Nonlinear climate dynamics: From deterministic behaviour to stochastic excitability and chaos

Dmitri V. Alexandrov, Irina A.Bashkirtsev,MichelCrucifix,Lev B.Ryashkoa

January 12, 2021

Contents

Abstract

Glacial-interglacial cycles are global climatic changes which have characterised the last 3 million years. The eight latest glacial-interglacial cycles represent changes in sea level over 100 m, and their average duration was around 100 000 years. There is a long tradition of modelling glacial-interglacial cycles with low-order dynamical systems. In one view, the cyclic phenomenon is caused by non-linear interactions between components of the climate system: The dynamical system model which represents Earth dynamics has a limit cycle. In another view, the variations in ice volume and ice sheet extent are caused by changes in Earth's orbit, possibly amplified by feedbacks. This response and internal feedbacks need to be non-linear to explain the asymmetric character of glacial-interglacial cycles and their duration. A third view sees glacial-interglacial cycles as a limit cycle synchronised on the orbital forcing.

The purpose of the present contribution is to pay specific attention to the effects of stochastic forcings. Indeed, the trajectories obtained in presence of noise are not necessarily noised-up versions of the deterministic trajectories. They may follow pathways which have no analogue in the deterministic version of the model. Our purpose is to demonstrate the mechanisms by which stochastic excitation may generate such large-scale oscillations and display intermittency. To this end, we consider a series of models previously introduced in the literature, starting by autonomous models with two variables, and then three variables. The properties of stochastic trajectories are understood by reference to the bifurcation diagram, the vector field, and a method called stochastic sensitivity analysis. We then introduce models accounting for the orbital forcing, and distinguish forced and synchronised ice-age scenarios, and show again how noise may generate trajectories which have no immediate analogue in the deterministic model.

We conclude on a general reflexion on the interest of this research and its potential applications on a wide range of climatic phenomena.

Chapter 1

Introduction

1.1 The processes and natural phenomena influencing the Earth's climate

The changes in temperature and circulation of the oceans that occurred over Earth history left traces all over the globe. For example, foraminifera — millimetre-size marine organisms — produce a calcite shell, of which the isotopic composition is influenced by temperature and salinity of the water in which the foraminifera developed, and the amount of ice accumulated over the continents. Foraminiferas accumulate in sediments, which can be recovered in deep-sea cores, and then analysed with mass spectrometers. Gas bubbles trapped in ice sheets, stalagmites, peat bogs containing pollen, and moraines similarly provide palaeoclimate evidence at different time scales, which form the basis for palaeoclimate reconstructions [1].

These reconstructions have revealed that climate varies on all time scales. Among others, the slow cooling trend which characterises the latest 65 Ma [1]. — this era is called the "Cenozoic" — was punctuated by temperature maxima (the Eocene thermal optimum, the Miocene optimum), somewhat rapid transitions (such as the Eocene - Cenozoic transition marking the first glaciation of Antarctica), and rapid excursions of surprisingly high amplitudes [2, 3]. During the Palaeocene-Eocene Thermal Maximum (PETM), about 56 Ma BP (BP = before present), thousands of gigatons of carbon were released in the atmosphere, causing a temperature surge of 5 to 8 ° [4, 5]. The carbon release and the concomitant temperature increases happened over a duration of the order of 10 to 20,000 years, and the whole event lasted about 200,000 years.

The amount and variety of data increase as we approach the present, making it possible to identify and characterise events with increasing temporal

[1]throughout this manuscript we use the following convention: 1 ka = 1000 years; 1 Ma = 1000 ka

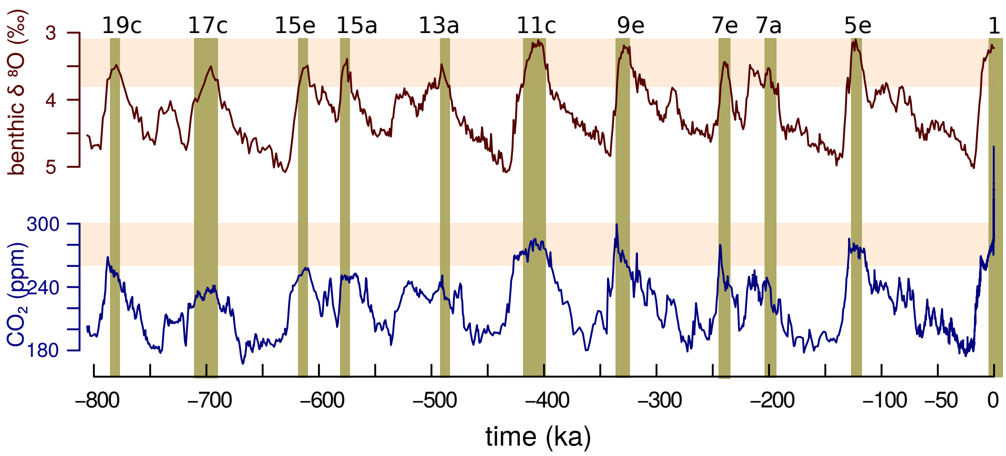

Figure 1.1: Reconstruction of the averaged isotopic ratio of oxygen sampled in benthic foraminifera calcite, expressed as a measure called the δ^{18}O [10], and CO_2 concentration sampled from Antarctic ice core records, expressed in part per million in volume [11, 12]. These two records provide the classical illustration of Late Pleistocene glacial-interglacial cycles. Bands and numbers refer to interglacial periods, with number denoting so-called isotopic stages following a scheme introduced by [13].

resolution. Throughout this review we will focus on the Pleistocene. This period starts around 3 Ma ago. At this time, the Antarctic ice sheet already covered the Antarctic continent, and ice sheets had started to episodically appear and disappear in the northern hemisphere. Such cycles of ice accumulation and melt are termed *glacial-interglacial cycles*. Their amplitude and periodicity increased throughout the Pleistocene, with a step-change located around an event called the Mid-Pleistocene Transition (MPT). This event occurred between 800 ka and 1.2 Ma ago, depending on how exactly it is defined [6–8]. Glacial-interglacial cycles, which until the MPT followed a cycle of 40 ka, morphed into a saw-tooth pattern of an average period of 100,000 years. The amplitude of theses cycles has remained pretty stable since the MPT, but their period and shape varied quite significantly from one cycle to the next (Figure 1.1). Most cycles are terminated by a rapid transition towards the interglacial regime, during which northern hemisphere ice sheets melt and release the equivalent of 100 m of sea level in the oceans in about 10,000 years. This last phase is often called the "termination" [9]

Further zooming within a glacial-interglacial cycle, one discovers rapid climate variations. Their signature is found all over the globe, but their origin is located in the North Atlantic realm. The most spectacular ones, called the Dansgaard-Oeschger events [14], occur when ice sheets have reached a mid-size, before the mature stage that gives way to the deglaciation. Dansgaard-Oeschger events were originally defined as isotopic excursions in the composition of Greenland ice. It is known today that these events were produced by jumps in temperature of the order of 10 ° or more [15]. They are associated with atmospheric circulation which occurred over a few years, and temperature changes are completed within a few decades [16]. Although Greenland ice older than the penultimate interglacial period is not available, indirect evidence attest the existence of similar temperature jumps over the last 800,000 years at least [17,18]. Smaller events punctuated the early stages of the glaciation [19–21].

The purpose of palaeoclimate dynamics theory is to explain these variations. The relevant mechanisms depend on the time scale under focus. At the time scale of several million years, climate changes are associated with tectonic drift and biological evolution. Tectonic drift affects the shape and orientation of continents, and it also affects the rates of rock weathering, which determine the fluxes of chemical compounds between the continents and the oceans. Biological evolution affects the rate and variety of biochemical reactions available on Earth — photosynthesis, reduction and oxydation of nitrogen compounds — as well as, among others, the texture and colour of soils.

The dynamics of glacial-interglacial cycles involve the hydrodynamics of ice, atmosphere, and ocean circulation. Winter snow precipitations are needed to grow ice sheets in the Northern Hemisphere, but, on the other hand, these newborn ice sheets will persist only if polar climates are cold enough, especially in summer [22]. We know today that the configuration of Earth's orbit and the value of its obliquity are quite critical for meeting these conditions, and this explains why the timing of glacial-interglacial cycles appear to be controlled by variations in Earth eccentricity, obliquity, and the position of perihelion. This is the basis of the Milankovitch theory [23]. As ice sheets grow, they create conditions propitious to cool their own surface by reflecting sunlight (albedo feedback) and reaching higher elevations. Their size may then increase until they become limited by the geometry on the continent and, since Milankovitch, we have learned that this can be a factor of instability that explains the abruptness of deglaciation [24, 25]. However, theories of ice age cycles also involve other important factors explaining the amplitude and size of ice sheet cycles. The growth of ice causes changes the structure and depth of ocean circulation, the extent and density of forests cover, and marine biological activity, which all affect the concentration of CO_2 in the atmosphere. Because of the greenhouse effect, CO_2 changes impact climate, and thus ice sheet growth. The dynamics of ice sheet and CO_2 form a coupled system with, as we will further develop below, may have non-trivial implications.

Ocean waves and instabilities also explain climatic variations over time scales from a few years to several thousands of years [26]. The Dansgaard-Oeschger events, in particular, are now believed to be associated with a form of instability in the North Atlantic circulation involving convection in the Nordic Seas, and advection of salt and heat by western boundary currents. These instabilities are also likely to interplay with the dynamics of ice sheets and their marine platforms which, when melting, release icebergs and melt water in the ocean [27].

Topping this scenery, volcanic eruptions and bolide events may have affected the climate system with consequences ranging from benign to disruptive. The bolide impact that caused or triggered the CretaceousPalaeogene extinction [28] is a major and rare event, but every century is punctuated by a number volcanic eruptions causing a short-lived negative temperature excursion of the order of a few tenths of degree. The Tombora 1815 eruption is a well-studied example which has allowed climate scientists to conclude that such an eruption can cause local temperature variations of the order of several degrees, and a global temperature anomaly of the order of one degree, with a life span of the order of 5 to 10 years [29].

1.2 The quest of dynamical behavior

The number of processes involved in the dynamics of Earth's climate changes is overwhelming. Hydrodynamic flows including ocean and atmospheric circulation are the domain of geophysical fluid dynamics, in which equations of motions involve partial derivatives in space and time. The combination of rotation and Sun heating generate waves and instabilities of time scales ranging from the second to several millennia. They explain, for example, the inconstancy of extratropical weather. The underlying equations of fluid motion have no closed-form solution, because the convection term is non-linear. Modelling heating terms is also a difficult problem, among others because water exists under its three phases. Hence, for understanding atmospheric and oceanic motion on Earth it is common to use numerical simulation methods, which require truncating equations at a certain resolution. It is not practical to truncate equations down to the viscosity scale because the required storage and computing capacity would exceed by many orders of magnitude what computing technology may offer in any foreseeable future. Consequently, adequate theories and idealizations are needed to account for the effects of turbulence and sub-grid-scale waves.

However, understanding climate dynamics involves much more than hydrodynamics. Modelling the flow of ice in ice sheets also requires dealing with partial differential equations, along with a good understanding of ice rheology, thermal diffusion, and ice dynamics near the bedrock. On the continents, the roughness, colour and albedo of the surface are affected by the spatio-temporal dynamics of vegetation, surface and subsurface water flows, which in turn depend on climatic conditions. Modelling sea-ice dynamics confronts one with the movement of dense sea ice, the formation of leads, and their interaction with the ocean water column. Last, but not least, biological activity controls a significant fraction of the exchanges of gas and other chemical compounds (including, among others, CO_2 and organic carbon), which affect the radiation balance of the Earth.

Climate scientists have attempted to combine their knowledge of all these different processes into giant computer programs called 'general circulation models' (GCM). The memory and computing capacity of the best commercial computers are used to their maximum possibilities to solve the hydrodynamics equations of motion with the maximum possible resolution. Processes considered to be important, but which are not explicitly simulated by these equations, are said to be "parameterized".

What is the "maximum possible resolution" depends on the computer time one is willing to spend, and the time scale of interest. State-of-the-art GCMs typically cited in scientific reports about climate change have a typical horizontal resolution of the order of 1 degree in latitude and longitude in the atmosphere, and the highest-resolution versions of these models go down to a few tens of degrees [30].

Such models have obvious scientific and political interests, but there are also many good reasons for willing models with a higher degree of idealization and abstraction. Simulating longer time scales requires reducing the model spatiotemporal resolution. The models which follow this strategy are sometimes called "models of intermediate complexity" because they have fewer lines of code than GCMs, but they remain much more complicated than dynamical systems mathematicians usually deal with. Addressing longer time scales generally requires increasing the range of relevant processes which enter in consideration. For example, the climatic consequences of deep-sea sediment dissolution are irrelevant at the decadal time scale, but they matter at the millennial time scale. However, one can never study a time scale without some regard for what happens at shorter and longer time scales. Non-linear dynamics effective bridge small and large spatiotemporal scales. For example, the stability of continental-size ice sheets may depend on local, small-scale phenomena such as ice buttressing near marine ice shelves [31]. The continental shelves, although they contribute to only 20% of the global ocean production, possess characteristic features which make them particularly sensitive to the global climate changes associated with glacial-interglacial cycles (sensitivity to aeolian and riverine nutrient input and to variations in sea levels [32]. As we see it, building a model that would adequately represent every process is an overwhelming task.

As others have argued [33], large-scale simulators will therefore not, alone, provide scientists with a satisfactory understanding of climate variability and predictability. We need concepts to identify fundamental limits of this predictability, and also provide foundations for the emerging domain of climate control theory, which deals with the detection of early warning signals before climatic transitions, and identify causes of uncertainty.

These objectives can be contributed to by using the language and tools of dynamical systems theory. We need to be able to identify and justify possible analogies between different climatic phenomenon, and perhaps also establish analogies between climatic oscillations and other natural phenomena. To this end, we need to adopt a different mindset than the one which underlies the development of large climate prediction simulators.

Consider, for example, the energy-balance model. This model was famously introduced the same year by Budyko [34] and Sellers [35]. These models are based on partial differential equations representing the dynamics of the distribution of surface temperature across latitudes, and account for incoming radiation and the effects of a change in surface albedo. The latter introduces a non-linear term, which generates the possible coexistence of two stable fixed points: a cold and a warm state [36, 37], arranged in such a way that number of fixed points depends on a control parameter (the solar input). In spite of its extreme idealization, this model turns out to have useful explanatory power. It shows the possibility and emergence mechanism of a hysteresis dynamics between ice-free and ice-full states. Highly idealized models generally describe mechanisms which, a priori, are relevant over a reasonably narrow range of time scales. Glacial-interglacial cycles, for example, are an oscillation involving time scales of 40 to 100 ka. The El Niño southern oscillation involves time scales over a few years. Quite obviously, these different phenomena are captured with different models. Yet, the mathematical structure of these models are sometimes strikingly similar, allowing for enlightening analogies (see [38] and references therein).

1.3 What the reader can find in this review

The literature on low-order models of glacial-interglacial cycles is vast, with different traditions: low-order deterministic dynamical systems featuring limit cycle behaviour [39], theories of stochastic resonance [40, 41], quasi-linear, highly idealized models of ice mass balance [42], and models address ice sheet flow dynamics from physical principles [43]. These different traditions interacted over forty years.

The present review is deliberately focused on the first tradition, already partly addressed in [44]. However, compared to that review and the references therein, we bring much more emphasis on the effects of stochastic parameterizations and bifurcation scenarios. As we have already seen, dynamical systems tend to focus on mechanisms relevant over a reasonably narrow range of time scales, but they may, however, be influenced and interact with phenomena associated with smaller, or greater time scales. Consider, again, the latest glacial-interglacial cycles depicted on Figure 1.1. Every cycle is distinct, some variations are pretty rapid, especially in the CO_2 concentration, and it is not obviously clear how much of this behaviour is influenced or even perhaps determined by climatic mechanisms operating at millennial or even sub-millennial time scale. A typical strategy in climate modelling is to represent these phenomena with stochastic parameterizations, thereby generating a random dynamical system [45, sect. 2.3]. The tradition was introduced with the linear model of [46], and the design and justification of adequate stochastic parameterizations is an active area of research, especially in the domain of decadal variability and predictability [47,48]. Some of the non-trivial effects of noise in deterministic models of ice ages were discussed early on, in particular with the proposal that ice ages could be the manifestation of a phenomenon of stochastic resonance in a Budyko-Sellers type model [40]. However, as we will see, stochastic effects may have many other effects, and produce dynamics which have no equivalent in the framework of deterministic dynamical systems theory. Therefore, even though we will focus on models which have been presented as models of glacial-interglacial cycles, the analyses presented here may have implication across a larger range of climatic phenomena.

Emphasis, in this review, is heavily put on dynamical system analysis. To this end, we will start with autonomous oscillators in state space of two (Chapter 2), and three dimensions (Chapter 3), and then introduce the astronomical forcing (Chapter 4). The review is based on dynamical systems which have been previously introduced and discussed in the literature, but we have deepened the dynamical system analysis and introduced stochastic parameterizations such as to produce analyses that have not been discussed before.

In most cases, the authors of the reference studies on which we have based ourselves have introduced and discussed their models as a plausible representation of a mechanism of glacial-interglacial cycles. For example, the Rombouts-Ghil model [49] is presented as a representation of ocean-atmosphere-vegetation dynamics, and introduce physical quantities such as albedo, heat flux and vegetation fraction. We should be clear upfront about the fact that many models can generate oscillations, and the different low-dimensional ice-age models have been proposed over the latest forty years have sometimes emphasized very different mechanisms. This may be admittedly troubling to the reader. Observations and theory have made it clear that the physics of ice sheets and of the carbon cycle constrain, at least in part, their amplitude and shape [50], but some of the models we discuss the carbon cycle and ice sheet physics altogether, and focus on other mechanisms which may be quite disputable. From a physical standpoint, these models are thus inadequate, but we nevertheless introduce them because their dynamic properties are enlightening and useful to construct of our understanding of stochastic effects in non-linear dynamics. This will be the purpose of chapter 5 to synthesize our current understanding of glacial-interglacial cycles and propose avenues of research.

Chapter 2

Ice-temperature-vegetation 2D models

The succession of glacial and interglacial periods evokes an oscillation. From basic Lyapunov theory of stability, we know that a dynamical system must have at least two ordinary differential equations to produce self-sustained oscillations [51]. We therefore start our review with models which display these characteristics.

2.1 A simple auto-oscillatory climatic feedback system

2.1.1 Definition

The first climatic oscillator suggested here was imagined by [52]. This model describes the effect of isolation of the ocean surface by sea ice, which prevents (reduces) the heat flux from the ocean to the Earth's atmosphere. The extent of sea ice depends on the average temperature of the ocean, and this generates a non-linear feedback on land-ice growth. This model will provide us with the basis to introduce and understand the effects of additive and multiplicative noise parameterizations. More precisely, we will see that *additive* noise produces fluctuations of large and small amplitudes (called mixed-mode oscillations), within the basin of attraction. This type of noise may also cause transitions between a stable equilibrium and a limit cycle. Parametric noise may either increase the dispersion of random trajectories, or concentrate them near the unstable equilibrium, and bring the system from order to chaos.

The [52] model is illustrated on Fig. 2.1. Here $\zeta = \sin\varphi$ is the sine of the marine-ice latitude φ (measured from the equator), $\eta = \zeta$ at the ice edge, D_o is the mean ocean depth, and θ is the mean ocean temperature.

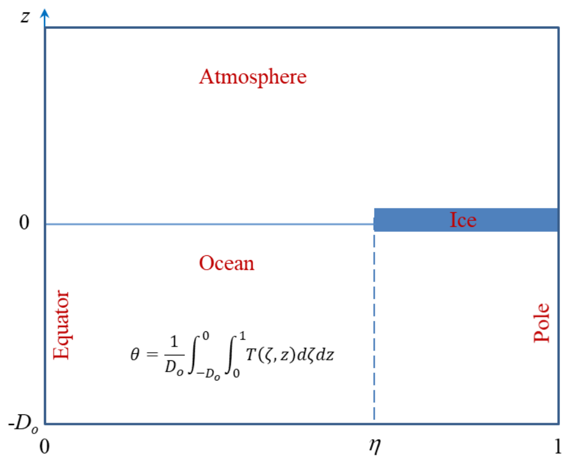

Figure 2.1: Idealized atmosphere–ocean–sea ice system (the mean ocean temperature θ is given by averaging of the local ocean temperature $T(\zeta, z)$ over coordinates ζ and z).

$$\begin{aligned} \dot{\eta} &= \phi_1\theta - \phi_2\eta + X_\eta, \\ \dot{\theta} &= -\psi_1\eta + \psi_2\theta - \psi_3\eta^2\theta + X_\theta, \end{aligned} \tag{2.1}$$

We use Newton's notation for differentiation: $\dot{\eta} = d\eta/d\tau$, $\dot{\theta} = d\theta/d\tau$, and τ is the time. The equation of η ($0 \le \eta \le 1$), and hence, φ ($0 \le \varphi \le \pi/2$) parameterize the process of ice melting when the mean ocean temperature increases. Parameters X_η and X_θ determine the growth rates of sea ice and temperature at points (η^*, θ^*) and (η_*, θ_*) where $\theta^* = \phi_2\eta^*/\phi_1$ and $\theta_* = \psi_1\eta_*/(\psi_2 - \psi_3\eta_*^2)$, respectively. The equilibrium points of the system (2.1) are described by means of zero parameters X_η and X_θ.

The positive parameters ϕ_1 and ϕ_2 describe the upward heat flux at the ice edge and the transmitted radiation absorbed at the surface [52]. Moreover, the denominators of ϕ_1 and ϕ_2 contain the contributions proportional to the latent heat of fusion and the ice mass inertia. Parameter ψ_1 defines the sensible, latent heat and longwave radiative fluxes. Parameter ψ_2 quantifies the effect of changes in the atmospheric carbon dioxide concentration. The nonlinear contribution containing ψ_3 describes the vertical heat flux at the surface (see, for details, [52, 53]).

This system was studied and discussed by [53–57]. We reproduce this analysis here. Let us introduce the departures η' and θ' of η and θ from their equilibrium (steady-state) values η_0 and θ_0 as

$$\eta' = \eta - \eta_0, \;\; \theta' = \theta - \theta_0, \;\; |\eta'| \ll \eta_0, \;\; |\theta'| \ll \theta_0, \tag{2.2}$$

where η_0 and θ_0 are chosen on the basis of recent observations ($\eta_0 \approx 0.941$, $\varphi \approx 70^o$N and $\theta_0 = 276.68$K [58, 59]).

Substituting variables (2.2) into equations (2.1) and keeping the small departures η' and θ', we obtain

$$\begin{aligned} \dot{\eta}' &= \phi_1 \theta' - \phi_2 \eta', \\ \dot{\theta}' &= -\psi_1 \eta' + \psi_2 \theta' - \psi_3 \eta'^2 \theta'. \end{aligned} \tag{2.3}$$

The coupled autonomous system (2.3) describes the following nonlinear mechanisms [53]: (i) the "ice-insulator" effect leading to a damped harmonic oscillation (contributions containing ϕ_1, ϕ_2 and ψ_1), (ii) a feedback between the atmospheric carbon dioxide concentration and the mean temperature in the ocean leading to a linear destabilizing tendency (contribution containing ψ_2), and (iii) when the dynamical system is far from its equilibrium the negative feedback operated by the nonlinear term (containing ψ_3) becomes dominant.

At this point, it is convenient to rescale variables and parameters as follows:

$$x = \frac{\eta'}{\gamma_1},\ y = \frac{\theta'}{\gamma_2},\ t = \phi_2 \tau,\ a = \frac{\phi_1 \psi_1}{\phi_2^2},\ b = \frac{\psi_2}{\phi_2},\ \frac{\gamma_1}{\gamma_2} = \frac{\phi_1}{\phi_2}, \tag{2.4}$$

where a and b are positive coefficients, and t is the dimensionless time.

Rewriting the dynamical system (2.3) in dimensionless variables (2.4), we have:

$$\begin{aligned} \dot{x} &= y - x, \\ \dot{y} &= -ax + by - x^2 y. \end{aligned} \tag{2.5}$$

We explore the different regimes exhibited by this deterministic dynamical system (2.5).

2.1.2 Identification of different dynamical regimes

First of all, observe that the system (2.5) has a trivial equilibrium point $M_0(0,0)$ for all values of coefficients a and b. This equilibrium is stable in the parametric region $b < a$ and $b < 1$ (region D in Fig. 2.2)). A phase trajectory going in region D is attracted to the equilibrium point M_0.

A stable limit cycle appears when the model parameters a and b cross the boundary between D and C. This boundary is defined by the line $b = 1$ at $a > 1$ and corresponds to the Andronov-Hopf bifurcation (the point M_0 loses its stability). Hence, in region C, the system displays stable auto-oscillations (2.5). Saltzman and co-authors analysed the global climate oscillations for fixed parameters $a = 6.4$ and $b = 4$ [53]. [54] studied the system dynamics in the vicinity of its Andronov-Hopf bifurcation boundary by means of the normal form technique. [55] further investigated the behaviour near the homoclinic

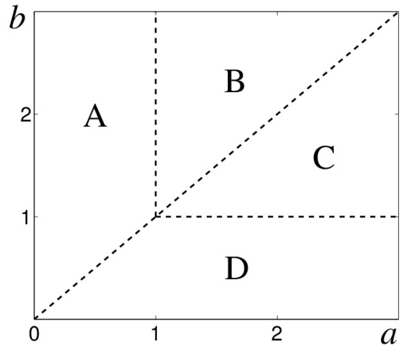

Figure 2.2: A scheme of parametric regions of the dynamical system (2.5).

bifurcation point. Finally, [57] carried a detailed parametric analysis of these equations.

Two nontrivial symmetric points of equilibrium $M_1(\bar{x}_1, \bar{y}_1)$ and $M_1(\bar{x}_2, \bar{y}_2)$ exist in the phase plane in the parametric region $b > a$ ($\bar{x}_1 = \bar{y}_1 = \sqrt{b-a}$ and $\bar{x}_2 = \bar{y}_2 = -\sqrt{b-a}$). These equilibrium points are stable in the region A ($a < 1$ at $b > a$). When $b < 1$, to two types of possible phase diagrams are possible (no cycles), (i) if $0 < a < b$, M_0 is unstable while M_1 and M_2 are stable, and (ii) if $a > b$, M_0 is the only stable point.

Let us now to describe the deterministic dynamics at $b > 1$ various values of the parameter a in the regions A, B, and C. To this end, we analyse the system behaviour for $b = 2$ by means of the bifurcation diagram shown in Fig. 2.3, where the y-coordinates of attractors and repellers are plotted against parameter a. Parameter a goes through four bifurcation points: $a_1 \approx 0.714$, $a_2 \approx 0.775$, $a_3 = 1$, and $a_4 = 2$. These points characterize the regions of different dynamic behaviour, namely A ($0 < a < a_1$), B ($a_1 < a < a_2$), C ($a_2 < a < a_3$), D ($a_3 < a < a_4$), and E ($a > a_4$). The corresponding phase portraits are shown in Fig. 2.4.

The equilibrium point M_0 is an unstable node at $a > a_4$, and a saddle point at $a < a_4$. In region A, the stable equilibrium points M_1 and M_2, and the unstable equilibrium M_0, completely determine the nonlinear behaviour. When a crosses a_1, a saddle-node bifurcation occurs and a new attractor appears. It is represented by a stable cycle surrounding all equilibrium points. An unstable cycle (red-dotted curve) isolates the equilibrium points from the attractors. There is a second bifurcation point at a_2, where the unstable cycle splits into two unstable cycles, and which defines region C. Each of these two unstable cycles surrounds the corresponding stable equilibrium. A subcritical point of Hopf bifurcation appears at $a = a_3$ where the unstable cycles collapse on their respective fixed points, M_1 and M_2, giving rise to unstable fixed

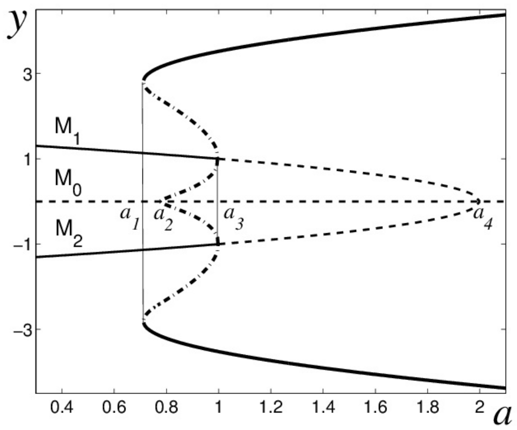

Figure 2.3: Bifurcation diagram at $b = 2$. The thin solid, dashed, thick solid, and dash-dotted lines show the y-coordinates of stable equilibria, unstable equilibria, extrema of stable cycles, and extrema of unstable cycles.

points. This defines a region D, characterized by three unstable equilibria, surrounded by a stable limit cycle. Finally, a pitchfork bifurcation arises at $a = a_4$, where the phase points M_1, M_2 and M_0 merge. This leads to a single unstable equilibrium point surrounded by the stable cycle in region E.

In summary, this simple climate model may have two stable, non-trivial equilibrium points (warm and cold attractors), as well as a stable limit cycle depending on the values of system parameters. Both attractors have their own "basins of attraction". Trajectories may therefore be attracted towards one or the other, depending on initial conditions.

2.1.3 Noise-induced phenomena and transition to chaos in the stochastic model

For convenience we assume that the ocean temperature is the variable which is most sensitive to random disturbances. We therefore inject uncorrelated white Gaussian noise $\xi(t)$ in the second equation (2.5) as follows:

$$\begin{aligned} \dot{x} &= y - x, \\ \dot{y} &= -ax + by - x^2 y + \varepsilon\xi(t), \end{aligned} \tag{2.6}$$

where ε stands for the intensity of fluctuations. The last contribution describes fluctuations of the ocean temperature. Numerical simulations of stochastic dynamics presented below are obtained with the Euler-Maruyama scheme [60]. We use the standard Box-Muller transform to model the stochastic components of the Gaussian fluctuations.

Fig. 2.5 illustrates different stochastic regimes in parametric domains A, B, C, and D, with phase trajectories (left), corresponding time series (middle),

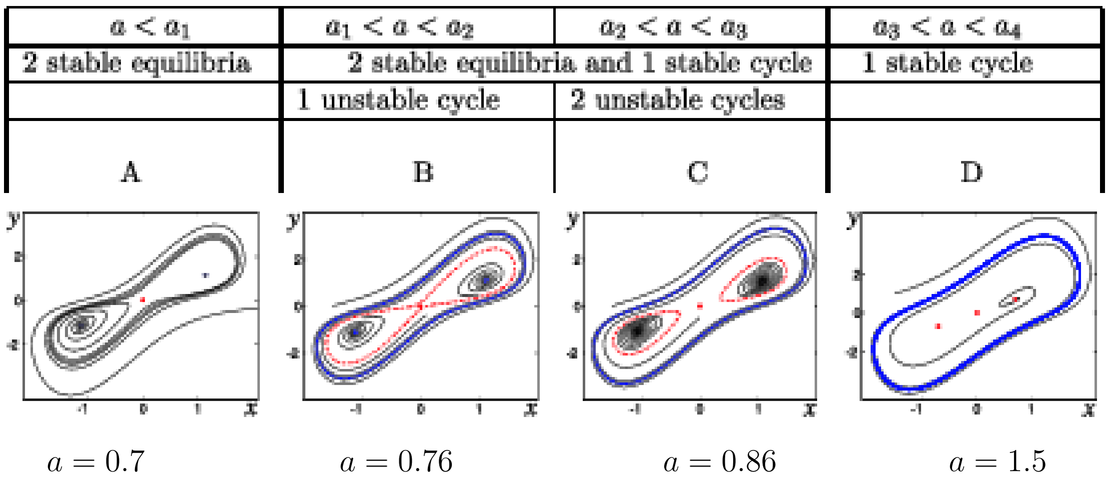

Figure 2.4: Different dynamical regimes for $b = 2$. The blue and red circles illustrate stable and unstable equilibria, while the blue solid, red dotted and black lines show the stable cycles, unstable cycles and phase trajectories.

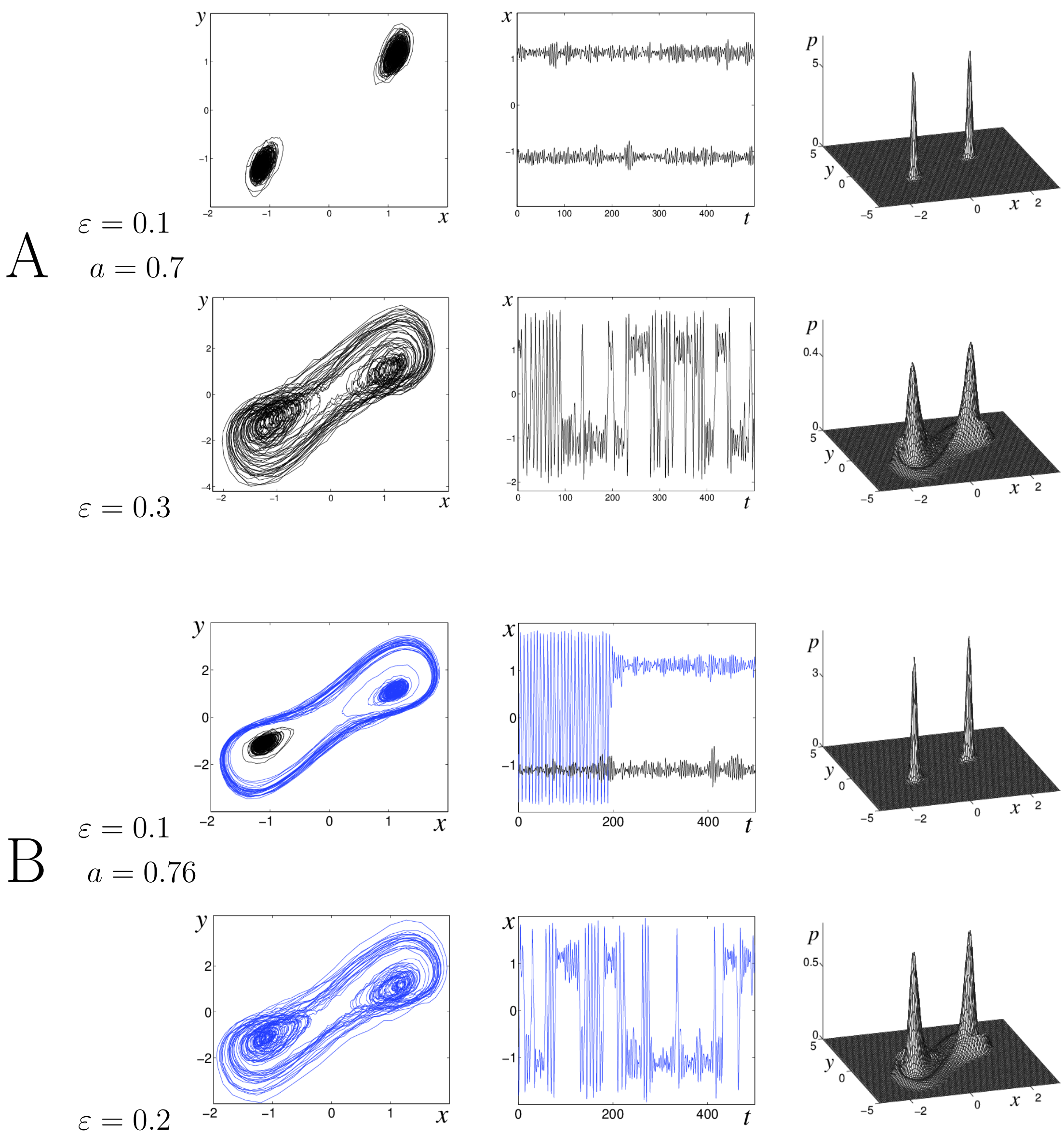

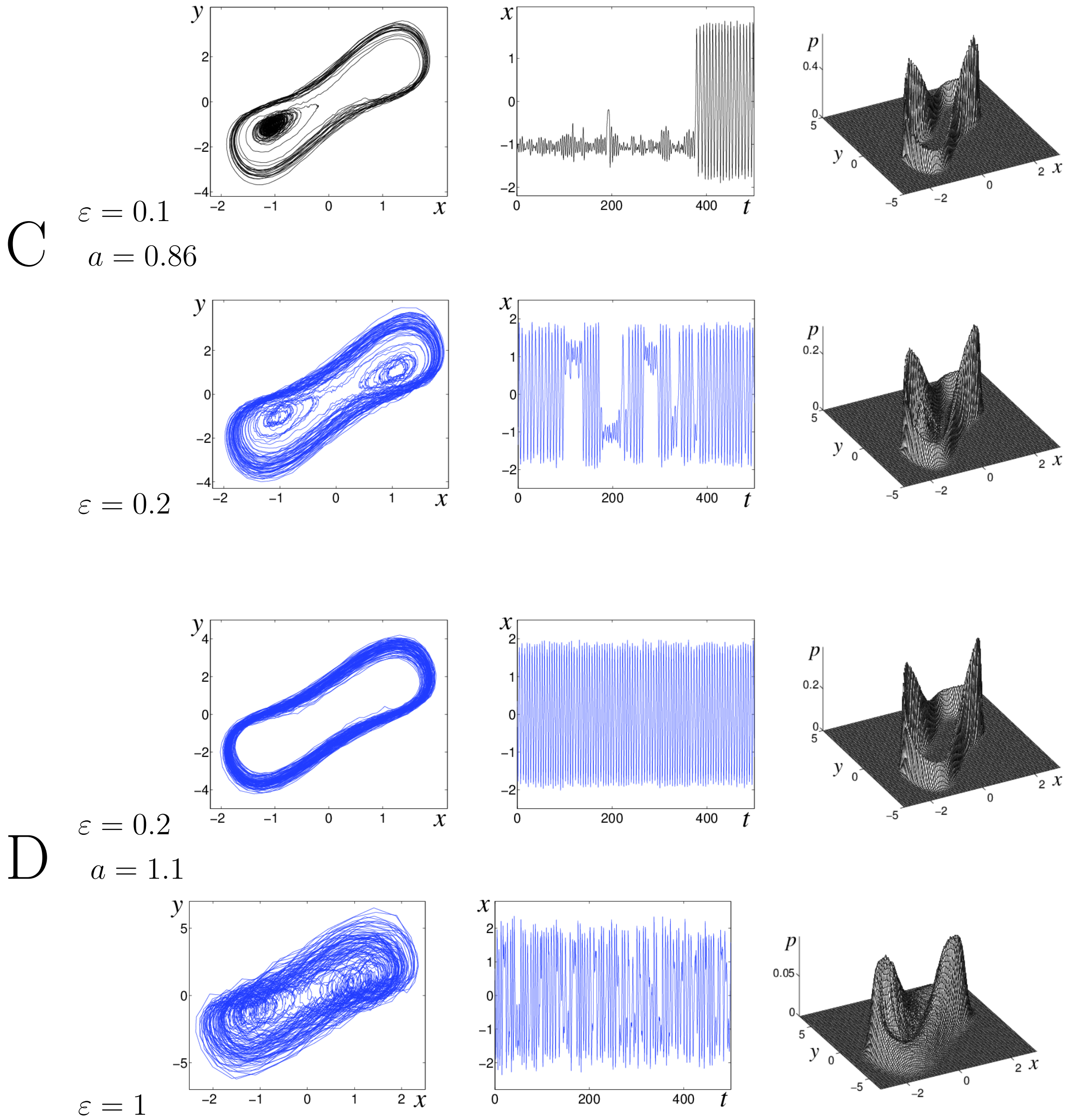

Figure 2.5: Random trajectories (left column), time series (middle column), and pdf (right column) in the presence of additive noise. The black and blue colours illustrate the phase trajectories starting from the stable equilibrium and stable cycle, respectively.

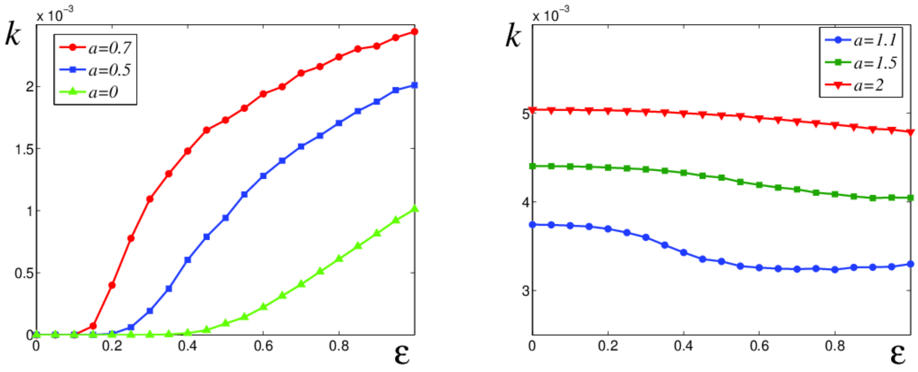

Figure 2.6: Dependencies k versus ε for the phase regions A (left) and D (right).

and stationary probability density functions (pdf, right). Random trajectories leave the deterministic attractors (stable equilibrium points or cycles) and determine a pdf under the influence of noise. Below we discuss some important features of the noise-induced dynamics in regions A, B, C and D which we defined above.

Region A. The phase trajectories in the presence of weak noise ($\varepsilon = 0.1$) remain in the vicinity of stable equilibrium points. They are termed some small amplitude stochastic oscillations (SASO) near equilibria, which are organized to form a pdf characterized by two sharp peaks, corresponding to the stable fixed points in the deterministic system. When the noise intensity increases ($\varepsilon = 0.3$ in panel A), trajectories occasionally escape their attractor and cross the separatrix. These trajectories form so-called large amplitude stochastic oscillations (LASO). In this case, LASO, and SASO coexist, and this coexistence generates a regime called mixed-mode amplitude fluctuations.

The pdf shown under higher noise intensity (panel A, right-hand side) shows an intriguing closed ridge, surrounding two peaks. This phenomenon is not associated with the corresponding deterministic dynamics (limit cycle), but we can understand its presence by considering the details of the transient trajectories. Deterministic trajectories (panel A in Fig. 2.4) running to the point of stable equilibrium go through a region, where the trajectories are temporally localized. The addition of noise generates a stochastic cycle, with the ratio of LASO trajectories over SASO ones increasing with noise intensity ε. The frequency of LASO can be quantified with the ratio $k = n(T)/T$, where $n(T)$ is the number of intersections of the mixed-mode oscillations $x(t)$ with the axis $x = 0$ on the interval $[0, T]$, and T represents the analysis time, which must be large enough for good statistics. Fig. 2.6 shows how $k(\varepsilon)$ varies with noise intensity ε, for different values of a.

Region B. We showed that in region B, M_1 and M_2 are isolated from the stable limit cycle by an unstable cycle (Fig. 2.4). This structure influences the dynamics of stochastic trajectories. Weak noise generates SASO near both equilibria. Larger noise intensity ($\varepsilon = 0.1$) authorizes transitions between the climate attractors. Specifically, trajectories around the cycle may leave their basin of attraction and become slowly attracted (after a few rotations) to one of the equilibrium points. This is a stochastically-induced transition "cycle-equilibrium". The inverse transition is possible as well. The transition "equilibrium-cycle" becomes more frequent under increasing the noise intensity ($\varepsilon = 0.2$). Transitions between attractors form LASO. Their coexistence with SASO produces a form of intermittency that characterizes individual trajectories (see the lower panel B in Fig. 2.5).

Region C. The deterministic phase portrait contains a stable cycle and a couple of stable equilibrium points divided by two unstable cycles. Here the stochastically-generated transition "equilibrium-cycle" happens at small noise and the intermittency of SASO and LASO regimes takes place with increasing ε (LASO predominates, the lower panel C in Fig. 2.5).

Region D. If the noise intensity ε is small enough, a random trajectory goes around the deterministic cycle in its basin of attraction (LASO, see the upper panel D in Fig. 2.5). An oscillating mode originates in the vicinities of stable equilibrium points ($\varepsilon = 1$, see the lower panel D in Fig. 2.5). The frequency of LASO in this mode of stochastic fluctuations is shown in the right panel in Fig. 2.6. The period $1/k(\varepsilon)$ slowly increases (decreasing k) and converges to half of the period of the limit cycle found in the deterministic model.

Is summary, additive noise changes the system dynamics but the structure of trajectories can be explained by reference to the underlying attractors. LASO, SASO, and mixed mode oscillations appear around the stable equilibrium points and stable cycles. In the second place, LASO are associated with two-way transitions between them. In other words, additive noise generates climatic transitions between regimes considered as stable in the deterministic system.

Perturbing parameters with a noisy process can be justified as a way to account for possible random disturbances in the physical mechanisms and processes parameterised by the model coefficients a and b. To this end, we rewrite the model equations (2.5) in the presence of simultaneous additive and parametric noises as

$$\begin{aligned} \dot{x} &= y - x, \\ \dot{y} &= -\left(a + \varepsilon_a \xi_a(t)\right) x + \left(b + \varepsilon_b \xi_b(t)\right) y - x^2 y + \varepsilon \xi(t), \end{aligned} \tag{2.7}$$

where $\xi_a(t)$, $\xi_b(t)$ and $\xi(t)$ represent the uncorrelated white Gaussian zero-mean noises, ε_a and ε_b stand for the intensities of a- and b- parametric noises (as before, ε designates the intensity of additive noise). In numerical simulations, we consider this stochastic system in Ito sense.

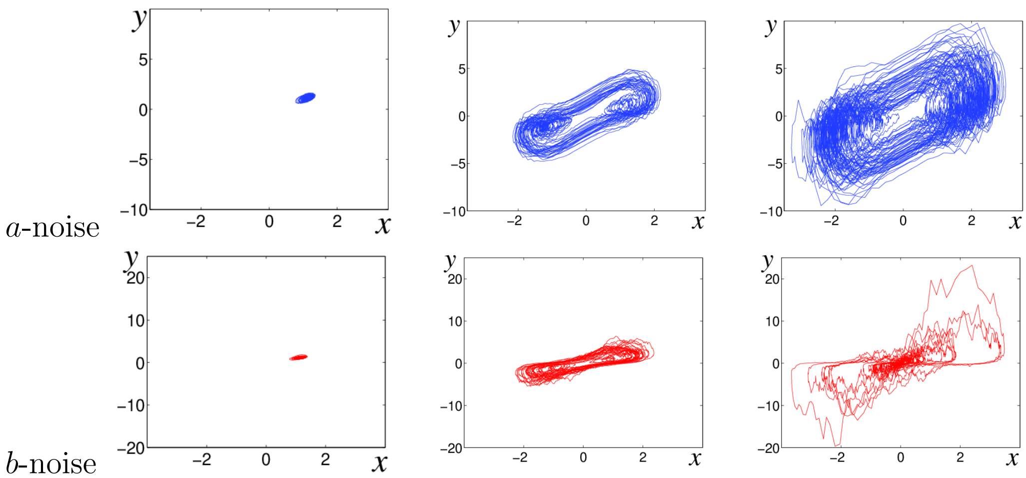

Figure 2.7: Stochastic dynamics in the presence of a parametric a-noise (top panel) and b-noise (bottom panel) for $a = 0.7$ and $\varepsilon = 0.01$. The upper panel is plotted for $\varepsilon_b = 0$ and $\varepsilon_a = 0.1$ (left), $\varepsilon_a = 0.5$ (middle), $\varepsilon_a = 2$ (right). The lower panel is shown for $\varepsilon_a = 0$ and $\varepsilon_b = 0.1$ (left), $\varepsilon_b = 0.5$ (middle), $\varepsilon_b = 2$ (right).

We adopt reference values for coefficients $a = 0.7$, and $b = 2$. The intensity of additive noise is fixed $\varepsilon = 0.01$. These parameters correspond to the following coordinates of the phase points: $M_1(1.14, 1.14)$, $M_2(-1.14, -1.14)$, and $M_0(0, 0)$ (region A). We consider the role of a-noise ($\varepsilon_a \neq 0$ and $\varepsilon_b = 0$) and b-noise ($\varepsilon_a = 0$ and $\varepsilon_b \neq 0$) in turn.

Fig. 2.7 illustrates the noise-induced dynamics of equations (2.7) at different values of noise intensities. Phase trajectories start from the equilibrium point M_1. With weak intensity, the trajectories remain near equilibrium M_1 (fluctuations in SASO regime, left column). This mode of oscillations changes with increasing noise intensity increases (fluctuations in LASO regime, middle column). So far, the dynamics are very similar to the aforesaid fluctuations in the case of additive noise.

However, this behaviour changes significantly when the noise intensity is increases further. The larger values of a-noise lead to larger amplitude and dispersion of fluctuations. The growth of b-noise localizes the phase trajectories in the vicinity of unstable equilibrium point M_0.

The left columns plotted in Fig. 2.8 show that the time dependencies of reduced marine-ice latitude x and the corresponding pdf look very similar for a- and b-noises. With increasing a-noise, the pdf takes the shape of a crater (compare the left and right column in the upper panel, Fig. 2.8), surrounded by two peaks corresponding to the stable equilibrium points M_1 and M_2. The effect b-noise is quite different: the pdf takes one a sharp peak with high noise

a-noise

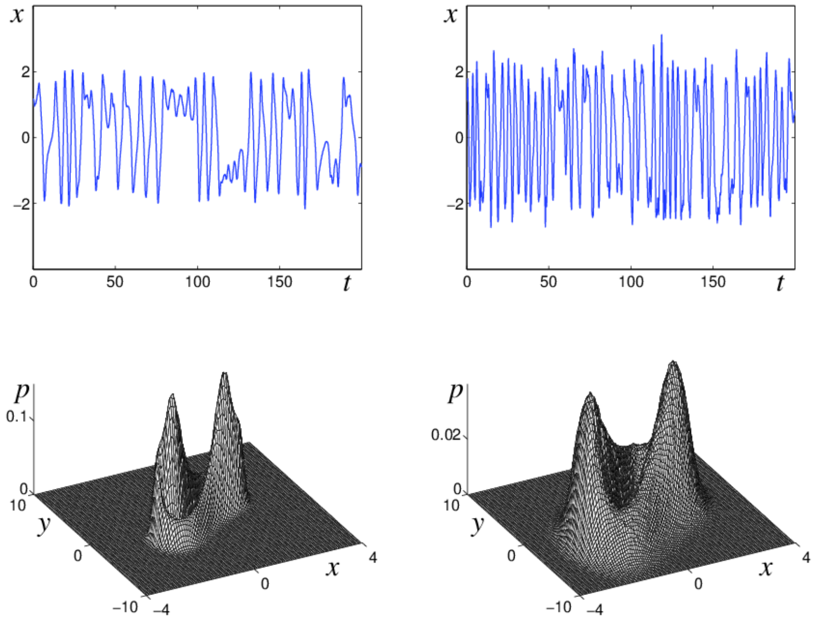

b-noise

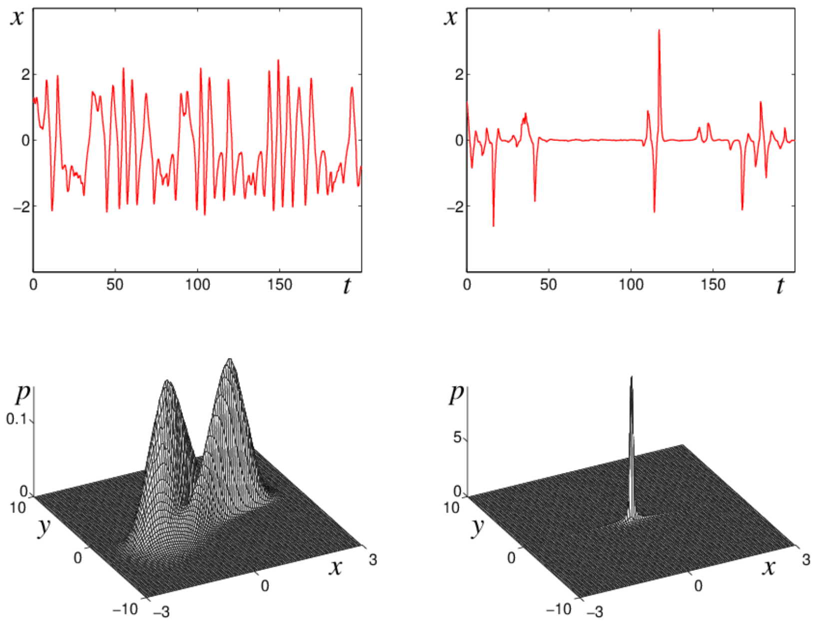

Figure 2.8: Time series and pdf in the presence of a parametric a-noise (upper panel) and b-noise (lower panel) for $a = 0.7$ and $\varepsilon = 0.01$. The upper panel is illustrated for $\varepsilon_b = 0$ and $\varepsilon_a = 0.5$ (left), $\varepsilon_a = 2$ (right). The lower panel is presented for $\varepsilon_a = 0$ and $\varepsilon_b = 0.5$ (left), $\varepsilon_b = 2$ (right).

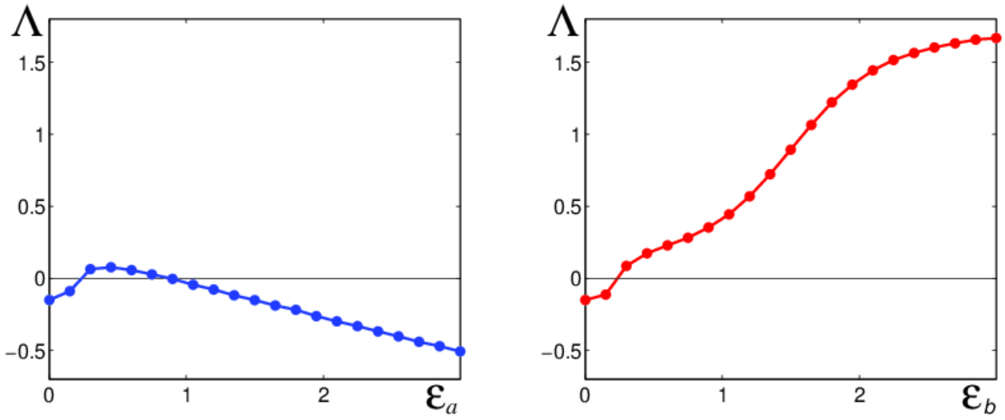

Figure 2.9: The largest Lyapunov exponents as functions of noise intensities calculated for the stochastic model (2.7) in the presence of a parametric noise for $a = 0.7$ and $\varepsilon = 0.01$ ($\varepsilon_b = 0$ (left) and $\varepsilon_a = 0$ (right)).

intensity: phase trajectories remain in the vicinity of the unstable equilibrium point. This is typical for parametric noise.

The effect of noise may be further characterized by considering the largest Lyapunov exponent Λ, shown in Fig. 2.9, for a- and b-noises. Note that these calculations are based on the standard Benettin method [61]. The Lyapunov exponent is negative for small amounts of a- and b-noises. The exponent Λ becomes positive for increasing noise levels, marking the transition to chaos. Λ keeps increasing monotonously with increasing b-noise intensity, while it becomes negative again with a-noise (compare the left and right panels in Fig. 2.9; a-noise and b-noise intensities are denoted with ε_a and ε_b, respectively). This can be explained as follows. Generally speaking, random phase trajectories go through the regions of local convergence and divergence; the sign of Λ is then determined by the balance of time spent between these regions. If the convergence regions dominate the total distribution, then $\Lambda < 0$; otherwise $\Lambda > 0$. With small noise, the phase trajectories run in the vicinity of stable equilibrium point M_1, which is a region of convergence. Consequently, $\Lambda < 0$. a-noise ejects phase trajectories towards the vicinity of unstable equilibrium M_0, which explains the transition towards positive Λ (chaos). However, even further a-noise levels eject trajectories well outside the limit cycle, which is a region of convergence, and explains why Λ becomes negative again. $b-$noise does not do this. It concentrates random states in M_0, and this is a divergence region. Hence, $\Lambda > 0$.

In summary, in the analysis of parametric noises (in the presence of additive noise) let us highlight that the dispersion of random trajectories and the amplitude of random oscillations may grow (a-noise), or shrink to the vicinity of the unstable equilibrium (b-noise). Parametric noise may also induce a transition to chaos. In absence of parametric noise, the stochastic system does

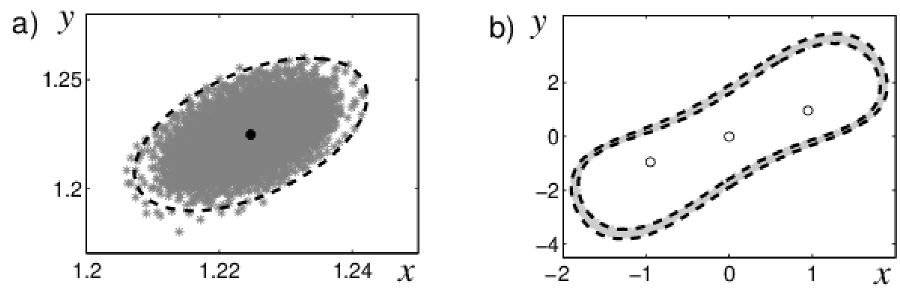

Figure 2.10: Random states (grey) of stochastic attractors and confidence domains (dashed lines): a) confidence ellipse around the equilibrium M_2 for $a = 0.5, \varepsilon = 0.01$, b) confidence band around the limit cycle for $a = 1.1, \varepsilon = 0.05$.

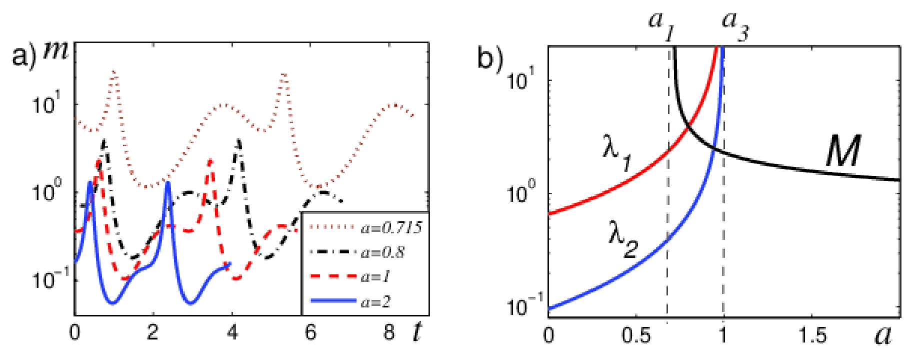

Figure 2.11: Stochastic sensitivity of attractors: a) plots $m(t)$ for cycles; b) plots $\lambda_1(a)$, $\lambda_2(a)$ for equilibria and $M(a)$ for cycles.

not exhibit the transition to chaos.

2.1.4 Stochastic sensitivity analysis of equilibrium and oscillatory regimes

The analysis above is based on numerical simulation of random trajectories. Another approach is possible, based on stochastic sensitivity functions and confidence domains techniques can be used. Mathematical details are given in Appendices A and B.

We however illustrate here the key ideas of this approach in the stochastic model with additive noise (2.6). The deterministic model (2.5) exhibits attractors in the form of equilibria or limit cycles. Under stochastic disturbances, a random solution of the stochastic system (2.6) leaves the deterministic attractor and produces a probability distribution (stochastic attractor) around it.

The dispersion of random states on such stochastic attractors can be estimated by the so-called stochastic sensitivity functions of initial deterministic attractors. They allow us to describe this dispersion geometrically, with the help of corresponding confidence domains. In the 2D-case, these domains are *confidence ellipses* around the equilibria, and *confidence bands* over limit cycles. These domains are assigned a fiducial probability, which quantifies the chances of finding the random states within the domain.

In Fig. 2.10, the confidence ellipse and confidence band with fiducial probability $P = 0.99$ are plotted by dashed lines and random states are shown in grey. As one can see, the confidence domains provide an adequate description of the spatial arrangement of random states in stochastic attractors.

The stochastic sensitivity of the equilibria $M_{1,2}$ is defined by the corresponding stochastic matrices $W_{1,2}$. In the considered system, $W_1 = W_2 = W$. The semi-axes of the confidence ellipse are determined by the eigenvalues λ_1, λ_2 of the matrix W, the noise intensity ε, and the fiducial probability (see Appendix B).

The stochastic sensitivity of the T-periodic limit cycle in two-dimensional case is defined by the scalar T-periodic function $m(t)$. The values of the function $m(t)$ determine the width of the stochastic bundle in the direction orthogonal to the deterministic limit cycle. To estimate the stochastic sensitivity of the limit cycle as a whole, it is convenient to use the stochastic sensitivity factor $M = \max m(t)$, $t \in [0, T]$.

In Fig. 2.11a), plots of the function $m(t)$ are shown for different values of a. As can be seen, the stochastic sensitivity along the limit cycles is non-uniform. Moreover, with the parameter a variation, one can observe changes not only in the height of the peaks for $m(t)$ but also in their quantity.

In Fig. 2.11b), the eigenvalues λ_1, λ_2, associated with the equilibria and stochastic sensitivity factor M of cycles, are plotted as functions of the parameter a. The stochastic sensitivity depends indeed mainly on the parameter a, and it increases unlimitedly to infinity near bifurcation points a_1 and a_3.

Near a_1, the cycle is more sensitive to noise than equilibria. Conversely, near a_3, the equilibria are more sensitive than the cycle. This difference in the sensitivity defines the direction of noise-induced transitions between the cycle and equilibria. Close to a_1, due to higher stochastic sensitivity of cycles, noise-induced transition occurs first from the cycles to equilibria; the other direction being possible at higher noise levels, only (see Fig. 2.5, panel B for $\varepsilon = 0.1, a = 0.76$). Even when both transitions occur, the low-amplitude oscillations near equilibria still dominate (see Fig. 2.5, panel B for $\varepsilon = 0.2$). Then, near a_3, the noise-induced transition occurs predominantly from equilibria to cycles (see Fig. 2.5, panel C for $\varepsilon = 0.1, a = 0.86$), and dominates mixed-mode oscillations at higher noise levels (see Fig. 2.5, panel C for $\varepsilon = 0.2$).

2.2 A mean temperature-vegetation model

Changes in albedo — the fraction of incident shortwave radiation reflected at the surface, or at the top of the atmosphere — play an important role in climate dynamics theory, because they constitute a potentially important feedback on climate change. Changes in *surface* albedo may be caused by changes in sea ice, snow and ice-sheet extent, and changes in area and structure of vegetation cover.

Changes in vegetation cover are interesting because they constitute one facet of the numerous mechanisms associated living organisms, and which, together, constitute an important internal force driving earth dynamics. There is, again, a fairly long history of works on vegetation-climate feedbacks, with some pioneering studies focusing on semi-arid areas [62], and others in the high-latitudes [63]. As in the preceding section, our choice is to focus on perhaps an outrageously simple model, with the purpose of outlining non-trivial effects of ramp effects, which characterise the dependency between climate and albedo.

The case study is here provided by Rombouts and Gill [49]. The underlying principle of this model is that lighter areas of the Earth's surface covered by snow or ice cool the planet whereas darker areas covered by the vegetated landscapes warm the Earth. The principle is encoded with two differential equations: one for the evolution of globally averaged temperature T, and one for the evolution of the fraction of land A covered by vegetation. The incoming and outgoing energy fluxes determine the temperature variations in time as

$$C_T \frac{dT}{dt} = (1 - \alpha(T, A))\, Q_0 - R_0(T), \tag{2.8}$$

where C_T and Q are the heat capacity and the incoming solar energy, and functions $\alpha(T, A)$ and $R_0(T)$ describe the Earth's albedo and the outgoing energy flux, respectively.

Fig. 2.12 illustrates the simple model under consideration: the Earth's surface is covered by the fraction p of land and $1 - p$ of ocean. In this case, one can use the following dependence

$$\alpha(T, A) = (1 - p)\alpha_o(T) + p\,(\alpha_v A + \alpha_g(1 - A))\,. \tag{2.9}$$

Here α_v and α_g stand for the albedo of vegetation and ground ($\alpha_v < \alpha_g$ due to the fact that forests are darker, absorbing more energy than bare ground).

Rombouts and Ghil further define temperatures $T_{\alpha,\ell}$ and $T_{\alpha,u}$ below and above which the ocean is ice-covered and ice-free, respectively. Ocean albedo

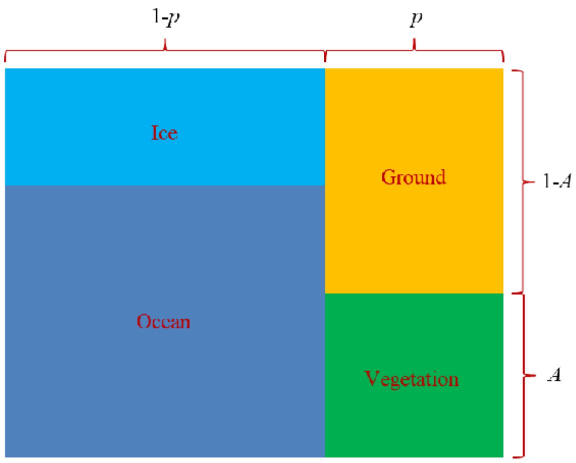

Figure 2.12: Partition of the Earth's surface used to derive equation (2.9). Ocean is divided into sea ice and ice-free fractions, and, land is separated into vegetation and bare soil.

α_o is then modelled with a ramp function [36, 64]

$$\alpha_o(T) = \begin{cases} \alpha_{\max}, \; T \leq T_{\alpha,\ell} \\ \\ \alpha_{\max} + f(T), \; T_{\alpha,\ell} < T < T_{\alpha,u} \\ \\ \alpha_{\min}, \; T > T_{\alpha,u}, \end{cases} \tag{2.10}$$

$$f(T) = \frac{\alpha_{\min} - \alpha_{\max}}{T_{\alpha,u} - T_{\alpha,\ell}} \left(T - T_{\alpha,\ell}\right),$$

and $\alpha_{\max}$ and $\alpha_{\min}$ represent the albedos of ice-covered and ice-free ocean.

The dependency of outgoing longwave radiation on temperature is linearized [49, 65]:

$$R_0(T) = B_0 + B_1 \left(T - T_{\text{opt}}\right), \tag{2.11}$$

where B_0 and B_1 represent the model parameters and T_{opt} is a reference temperature which, without loss of generality, is chosen to be the optimal temperature for vegetation growth. The parameterization is mainly justified as a linearization of the Stefan-Boltzmann law linking black-body temperature to longwave radiation emission, but it implicitly captures feedbacks associated with the dependency of water-vapour and CO_2 concentration, which both act as greenhouse gases, on temperature changes.

Vegetation cover dynamics are then be described by a logistic equation:

$$\frac{dA}{dt} = \beta(T)A(1 - A) - \gamma A, \tag{2.12}$$

where γ is the vegetation death rate and

$$\beta(T) = \max\left\{0, 1 - k\left(T - T_{\text{opt}}\right)^2\right\}$$

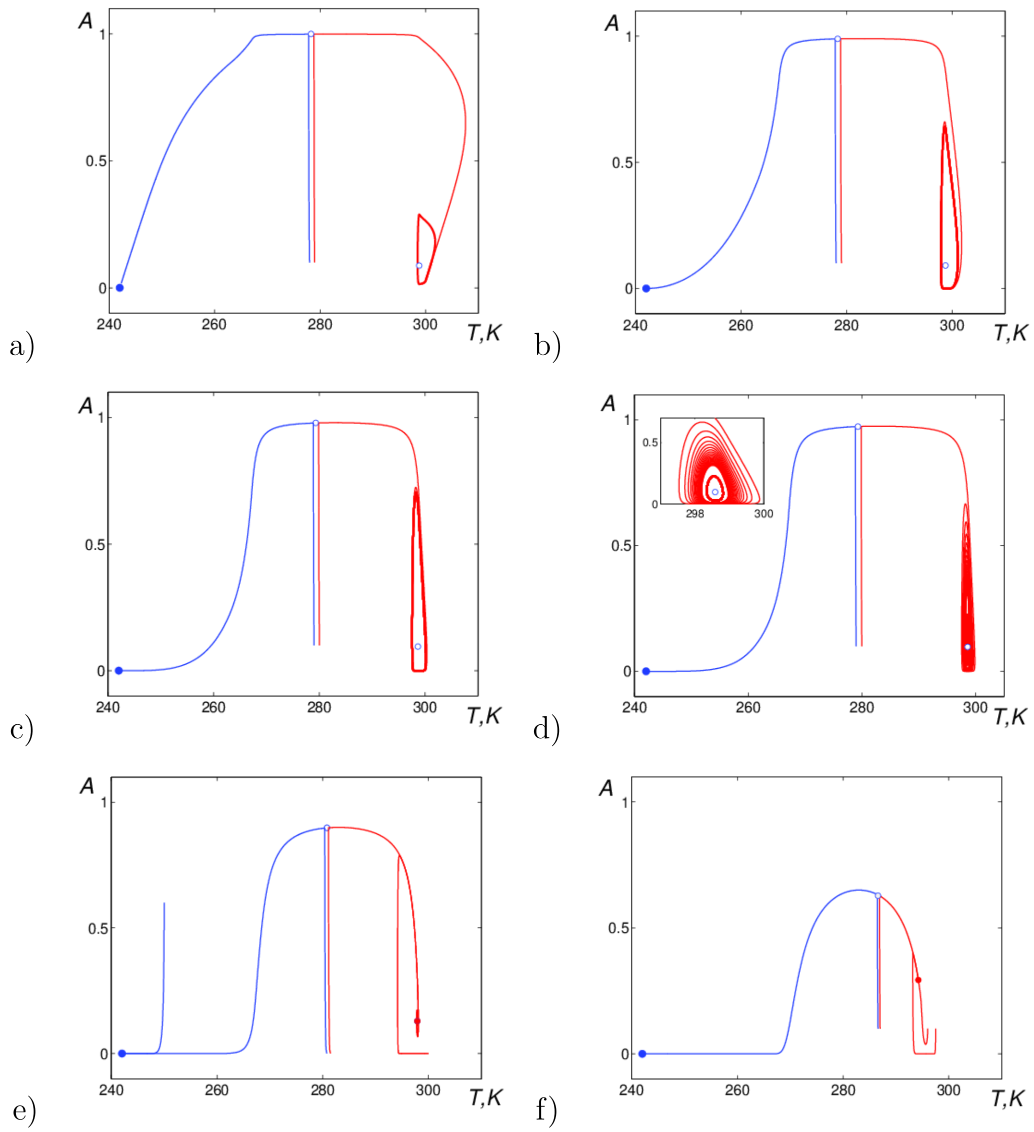

Figure 2.13: Deterministic phase trajectories of the climate-vegetation model: a) $\gamma = 0.001$, b) $\gamma = 0.01$, c) $\gamma = 0.02$, d) $\gamma = 0.025$, e) $\gamma = 0.1$, f) $\gamma = 0.35$ (model parameters are listed in Table 2.1).

represents the temperature-dependent growth rate: the dependency on temperature is parabolic with a maximum at $T = T_{\text{opt}}$ (k is the growth curve thickness).

The two-dimensional nonlinear model (2.8)-(2.12) describes the evolution of this climate-vegetation system in the temperature-vegetation cover phase plane, where the variables T and A evolve at a fixed set of system parameters (Table 2.1) under the influence of various external processes and phenomena (stochastic forcing).

Table 2.1: Model parameters of the climate-vegetation system [49].

Parameter	Value
Heat capacity, C_T	500 W yr K^{-1} m^{-2}
Incoming solar energy, Q_0	342.5 W m^{-2}
Fraction of land, p	0.3
Albedo of vegetation, α_v	0.1
Albedo of ground, α_g	0.4
Albedo of ice-covered ocean, $\alpha_{\max}$	0.85
Albedo of ice-free ocean, $\alpha_{\min}$	0.25
Temperature below which ocean is ice-covered, $T_{\alpha,\ell}$	263 K
Temperature above which ocean is ice-free, $T_{\alpha,u}$	300 K
Constant in outgoing radiation, B_0	200 W m^{-2}
Constant in outgoing radiation, B_1	2.5 W K^{-1} m^{-2}
Optimal growth temperature, T_{opt}	283 K
Growth curve thickness, k	0.004 yr^{-1} K^{-2}
Death rate of vegetation, γ	0.1 yr^{-1}

2.2.1 Vegetation or Snowball Earth: bistability in the deterministic model

Fig. 2.13 shows different deterministic phase trajectories, depending on the value chosen for vegetation death rate γ. This model has two equilibria corresponding to the cold (blue) and warm (red) state.

For low death rates (a), phase trajectories started from a middle-point temperature are attracted towards either a warm limit cycle (300 K, with high vegetation), or a cold fixed point (no vegetation, $A = 0$). The warm limit cycle surrounds an unstable fixed point represented by an open circle.

As the death rate is increased (see panels (b), (c), (d)), the warm limit cycle becomes narrower — temperature oscillations are smaller — until the system meets a supercritical Andronov-Hopf bifurcation (panel (f)). At this point the stable cycle and unstable equilibrium merge (red spot in panel (f)). This implies that any initial condition will end up with the system stabilising in one of both fixed points, which one is reached depending on which side of the separatrix the system started. There is no possibility of crossing the separatrix. The time series shown in Fig. 2.14 reveal also that the period of warm-climate oscillations decreases as one approaches the Andronov-Hopf bifurcation.

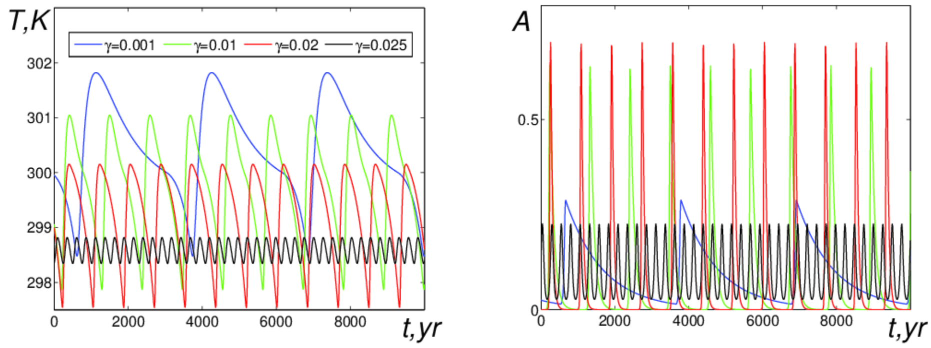

Figure 2.14: Average temperature (a) and fraction of land A covered by vegetation versus time in the case of deterministic dynamics.

2.2.2 Equilibrium and oscillatory vegetation: noise-induced dynamics

We now describe the effect of introducing noise perturbing the temperature forcing vegetation. The rationale being that T is a slowly-evolving (ocean) temperature subject to radiative balance, while vegetation experiences fluctuating "weather":

$$\begin{cases} C_T \dfrac{dT}{dt} = (1-\alpha(T,A))\, Q_0 - R_0(T), \\[2ex] \dfrac{dA}{dt} = (\beta(T) + \varepsilon\xi(t))\, A(1-A) - \gamma A. \end{cases} \tag{2.13}$$

Again $\xi(t)$ represents a standard Gaussian white noise, $\langle \xi(t) \rangle = 0$, $\langle \xi(t)\xi(\tau) \rangle = \delta(t-\tau)$, and ε stands for the noise intensity (note that we omit its dimension below). This model is considered in Ito sense.

As before, we use the Euler-Maruyama scheme to implement the stochastic integration (the time step is 0.01 yr). Simulated trajectories are shown on Fig. 2.15, in which panels (a), (b) and (c) corresponding to different regimes determined by γ. At low noise intensity (green), the fraction of land A covered by vegetation oscillates near the deterministic cycle (panel (a)) or the stable points of equilibria (panels (b) and (c)).

As the noise intensity is further increased, the global temperature leaves the warm attractor and freezes to a "Snowball Earth", with global temperature around 242 K. The critical intensity threshold depends on γ, and it increases with increasing γ.

The dependency on γ may be understood as follows. With low death rates, the warm stage undergoes, as we have seen, a limit cycle. Climate trajectories therefore approach, periodically, the separatrix isolating the warm region from the cold attractor. At this time, climate is at risk of being ejected to a Snowball Earth stage by a stochastic perturbation. As γ increases, the amplitude of the

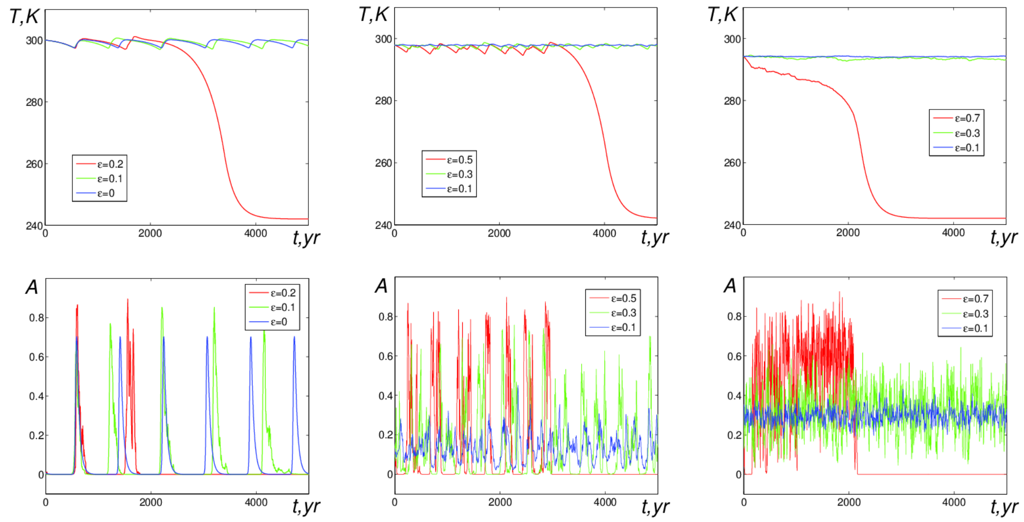

a) b) c)

Figure 2.15: Stochastically-induced evolution of the climate-vegetation system for $\gamma = 0.02$ (a), $\gamma = 0.1$ (b), and $\gamma = 0.35$ (c).

limit cycle decreases and the warm state is increasingly protected from fatal ejections to the cold attractor. A transition therefore requires a higher level of noise, and when this happens, the transition itself is steeper. The fraction of land A therewith drops to zero (red curves in the lower panel in Fig. 2.15). With further experimentation, we observe that the value at stepwise transition occurs for a limited interval of noise intensity, which depends on γ (see Fig. 2.16): it occurs for $0.15 \lesssim \varepsilon \lesssim 0.2$ for $\gamma = 0.01$ (panel (a)) and $0.35 \lesssim \varepsilon \lesssim 0.55$ for $\gamma = 0.1$ (panel (b)).

The dynamics of the transition is further illustrated on 2.17, this time with $\gamma = 0.35$. We take this higher value of γ, more robust to noise, to emphasise what happens *before* the transition. Expectedly, higher noise intensities cause more dispersion around the warm equilibrium (pdfs are wider with higher noise levels), until the trajectories have enough momentum to escape the warm attractor ($\varepsilon = 0.7$) and lock into the frozen stage.

2.2.3 Could noise freeze the Earth?

There is geological evidence of global glaciations called Snowball Earth episodes during the late Proterozoic (600 to 800 Ma ago). Ice sheets are thought to have reached the Equator [66–69]. Snowball Earth episodes ended thanks to volcanic outgassing, which may have pushed atmospheric CO_2 concentration levels to 350 times the modern level [70].

The simple dynamical model features such an transition to a Snowball Earth, triggered by a noise fluctuation, but made more likely by a limit cycle

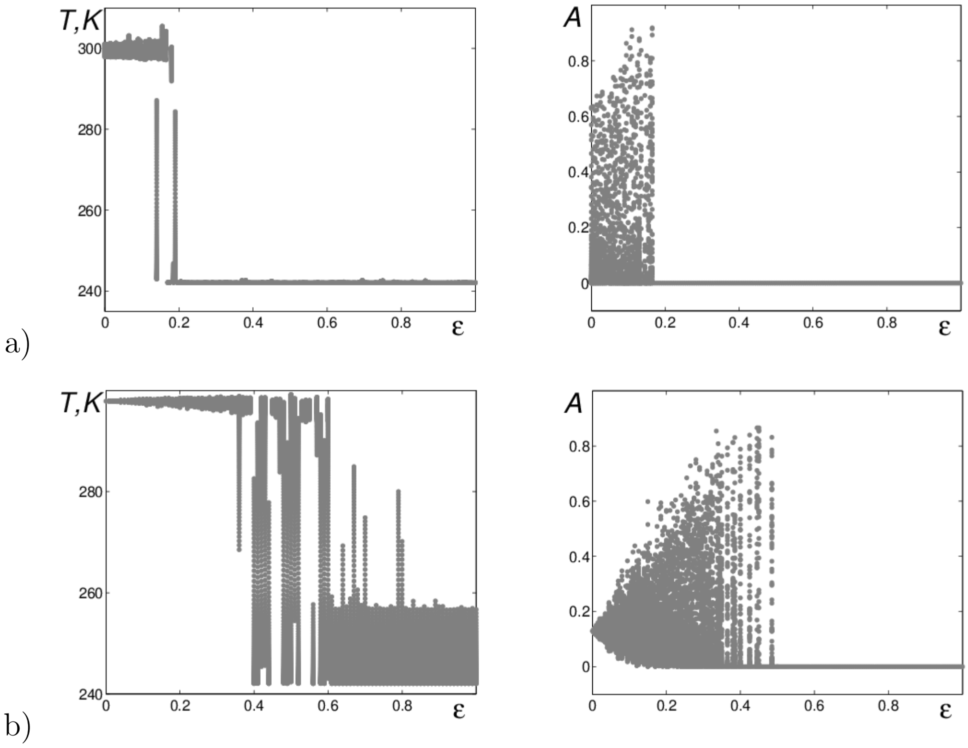

Figure 2.16: Random states of the climate-vegetation model for $\gamma = 0.01$ (a) and $\gamma = 0.1$ (b).

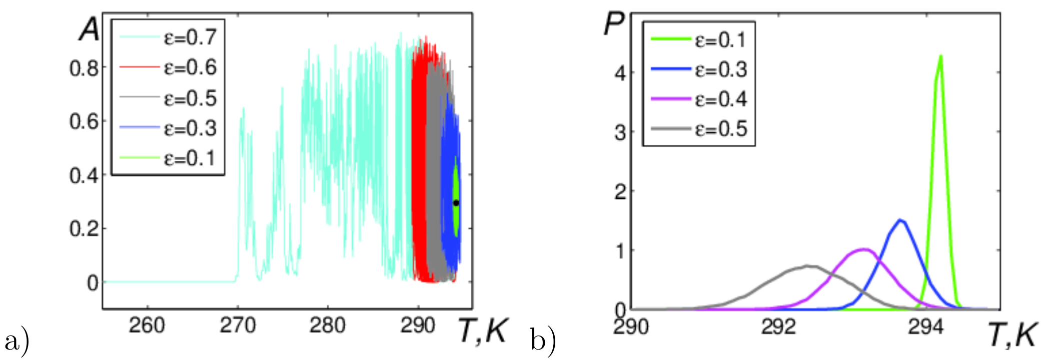

Figure 2.17: Stochastically-produced shift in the global temperature and pdf for $\gamma = 0.35$.

of the vegetation-climate system which periodically brings the climate dangerously close to the separatrix between cold and ward stages. Again, we have to bear in mind the caveats introduced earlier in this section. Variable “A” should not literally be interpreted as a vegetation state. Paleoclimate scientists are not aware of a 'global vegetation' oscillation. Yet, limit cycle dynamics, at the global scale, are plausible, even if they certainly involve much more complexity than a homogeneous vegetation cover. Mills et al. [71], for example, discovered in a dynamical system including a dozen of equation describing silicate weathering, respiration processes, and climate feedbacks, a slow limit cycle. They suggest to explain Snow-Ball earth glaciations as a phase of this cycle. Here, we show the possibility that a smaller cycle, around the warm state, would actually suffice to create the conditions propitious for precipitating a snow-ball Earth, if a deep-cold state exists and if enough stochastic forcing is present. This is speculative, but shows the heuristic value of associating stochastic forcing with deterministic forcing: this combination can offer new, previously overlooked explanations to known phenomena.

Chapter 3

Ice - temperature - carbon dioxide 3D feedback models

In this section, we continue to acquaint the reader with intriguing features emerging from the nonlinear dynamics observed in models of Earths climate changes at Quaternary time scales. Following the principle "from simple to complex processes", we explain the possible effects a third prognostic variable on the deterministic and stochastically-induced dynamic scenarios. The key phenomena considered below in more detail are the formation of irregular multimodal fluctuations consisting of the intermittency of large- and small-amplitude stochastic oscillations and possible chaotization of the Earth's climate following the introduction of stochastic forcing.

3.1 Continental ice - marine ice - mean temperature model

Following their earlier attempts with a 2-D model [53], Saltzman and Sutera included a third variable in their theory of glacial-interglacial cycles [39]. The state vector included a "mean temperature" (θ), continental (ζ), and marine (χ) ice masses (the marine mass is implicitly an aggregation of ice shelves and sea ice). A schematic diagram is presented in Fig. 3.1).

Let $\hat{\zeta}$, $\hat{\chi}$ and $\hat{\theta}$ describe the equilibrium values of dynamical variables ζ, χ and θ. Introducing the corresponding deviations from this equilibrium state as $(x, y, z) = (\zeta, \chi, \theta) - (\hat{\zeta}, \hat{\chi}, \hat{\theta})$, we come the following dynamical system after Saltzman and Sutera [39]

$$\begin{aligned} \dot{x} &= a_0 x + a_1(1 - a_2 y)y - a_3 z, \\ \dot{y} &= b_0 x + b_1(1 - b_2 y - b_3 y^2 - b_4 x^2)y - b_5 z, \\ \dot{z} &= c_0 x + c_1 y - \mu z, \end{aligned} \tag{3.1}$$

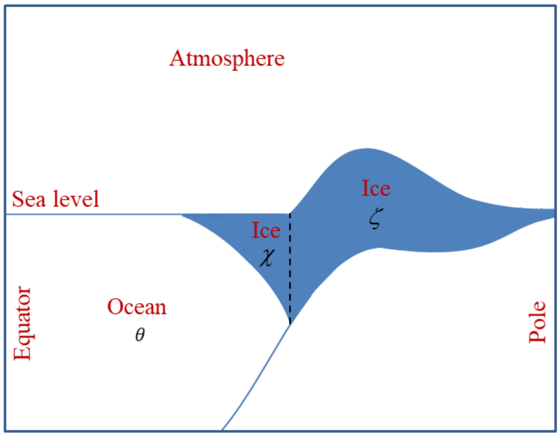

Figure 3.1: Idealized three-dimensional atmosphere–ocean–sea ice system: ζ - total continental ice mass (extended to the grounding line), χ - total marine ice mass (shelves, icebergs, and pack ice beyond the grounding line), and θ - mean ocean temperature.

where $\dot{x} = dx/dt$, t is time, and x, y, and z are the deviations of the continental and marine ice masses, and of the mean temperature from their equilibrium values. All the parameters are positive. The first contribution on the right-hand side (r.h.s.) of the first equation (3.1) describes the positive and negative feedbacks going to ζ, the second term containing the coefficient a_1 describes the effects of buttressing, ice albedo, and the feedback between continental ice mass and poleward heat transport. The last term on the r.h.s. involving the coefficient a_3 parameterises the positive influence of low latitude warming on the poleward atmospheric heat flux towards the sea-ice covered regions. The flux of continental ice directed to the ice shelves and the ice stream flow are defined by the term involving b_0. The positive feedbacks associated with the sea level changes, ice albedo and the feedback between marine ice and heat transport are parameterised by the term involving b_1. Melting and freezing of ice shelves and sea-ice are parameterised with the coefficient b_5. The first contributions on the r.h.s. of the third equation describe the "sea-ice insulator" effect (sea-ice reduces ocean cooling), and a quite speculative effect positing that continental ice, which releases meltwater, reduces ocean mixing and, thereby, effectively warms the ocean. The effect of thermal damping of deep ocean caused by the diffusive phenomenon is described by the term with the coefficient μ.

It turns out that in this nonlinear system, stable equilibria coexist with limit cycles. As we shall see, this configuration generates conditions of high noise sensitivity: noise-induced transitions between the basins of attraction of the different attractors are prone to induce chaos.

3.1.1 Attractors and bifurcations in the deterministic model

It is convenient to introduce the following dynamical variables:

$$u = k_x x, \;\; v = k_y y, \;\; w = k_z z, \tag{3.2}$$

where $k_x = 0.29 \cdot 10^{-19}$ kg^{-1}, $k_y = 0.75 \cdot 10^{-17}$ kg^{-1}, and $k_z = 0.32$ K^{-1} [39].

Setting $\dot{x} = \dot{z} = 0$ in equations (3.1), we find the system equilibria

$$x(y) = \frac{a_3 c_1 y - \mu a_1 (1 - a_2 y) y}{\mu a_0 - a_3 c_0}, \;\; z(y) = \frac{c_0 x(y) + c_1 y}{\mu}.$$

Substituting now these expressions into the third equilibrium condition $\dot{y} = 0$, we arrive at $g(y) = 0$, where

$$g(y) = b_0 x(y) + b_1 \left(1 - b_2 y - b_3 y^2 - b_4 x^2(y)\right) y - b_5 z(y).$$

This function $g(v)$ is shown in Fig. 3.2 for different parameters μ. Panel (a) focuses on $\mu \geq 10^{-4}$ y^{-1}, which may be judged as more physically realistic if we view the ocean as a heat reservoir, but in (b) we nevertheless examine $\mu > 10^{-4}$ y^{-1} because as we will soon discover, this yields interesting behaviours. Taking some freedom with respect to the physical interpretation of a dynamical system is not unusual in the climate literature as it may serve some heuristic purpose towards understanding climate phenomena (think of the celebrated Lorenz-Saltzman model [72]), but we will need to keep limitations in mind when drafting conclusions.

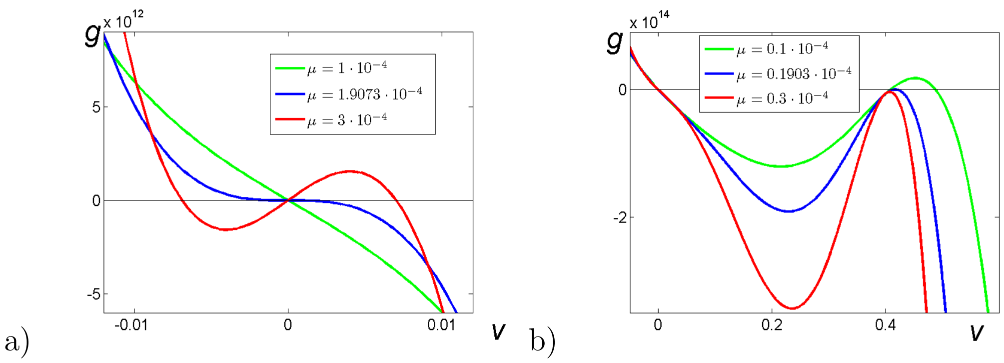

Figure 3.2: Plots of $g(v)$ for various values of the parameter μ: (a) $\mu = 1 \cdot 10^{-4}$ y^{-1} (green), $\mu = \mu_0 = 1.9073 \cdot 10^{-4}$ y^{-1} (blue), and $\mu = 3 \cdot 10^{-4}$ y^{-1} red); (b) $\mu = 0.1 \cdot 10^{-4}$ y^{-1} (green), $\mu = \mu_* = 0.1903 \cdot 10^{-4}$ y^{-1} (blue), and $\mu = 0.3 \cdot 10^{-4}$ y^{-1} (red). The other system parameters are [39, 73]: $a_0 = 0$, $a_1 = 0.145$ y^{-1}, $a_2 = 1.86 \cdot 10^{-17}$ kg^{-1}, $a_3 = 1.265 \cdot 10^{14}$ y^{-1}, $b_0 = 0.276 \cdot 10^{-6}$ y^{-1}, $b_1 = 3.77 \cdot 10^{-4}$ y^{-1}, $b_2 = 1.58 \cdot 10^{-18}$ kg^{-1}, $b_3 = 3.77 \cdot 10^{-34}$ kg^{-2}, $b_4 = 0.7152 \cdot 10^{-38}$ kg^{-2}, $b_5 = 0.697 \cdot 10^{13}$ y^{-1}, $c_0 = 0.792 \cdot 10^{-23}$ y^{-1}, $c_1 = 28.65 \cdot 10^{-23}$ y^{-1}.

The function $g(v)$ contains a single root for $\mu \leq \mu_0 = 1.9073 \cdot 10^{-4}$ y^{-1}, corresponding to the trivial equilibrium $M_0(0, 0, 0)$. For $\mu > \mu_0$ (thus, smaller ocean temperature relaxation time), the system has two roots corresponding to two equilibrium points $M_1(\bar{u}_1, \bar{v}_1, \bar{w}_1)$ and $M_2(\bar{u}_2, \bar{v}_2, \bar{w}_2)$, where $\bar{u}_2 < 0 < \bar{u}_1$. Another bifurcation appears for lower values of μ (Fig. 3.2b and c). There are two positive roots for $\mu < \mu_* = 0.1903 \cdot 10^{-4}$ y^{-1}, associated with two equilibrium points $M_1(\bar{u}_1, \bar{v}_1, \bar{w}_1)$ and $M_2(\bar{u}_2, \bar{v}_2, \bar{w}_2)$. M_1 is unstable and M_2 is stable. The two positive roots of the function $g(v)$ merge at the point $\mu = \mu_*$, above which only the trivial equilibrium M_0 persists. The boundary point μ_* is thus a bifurcation point, which we will characterise later.

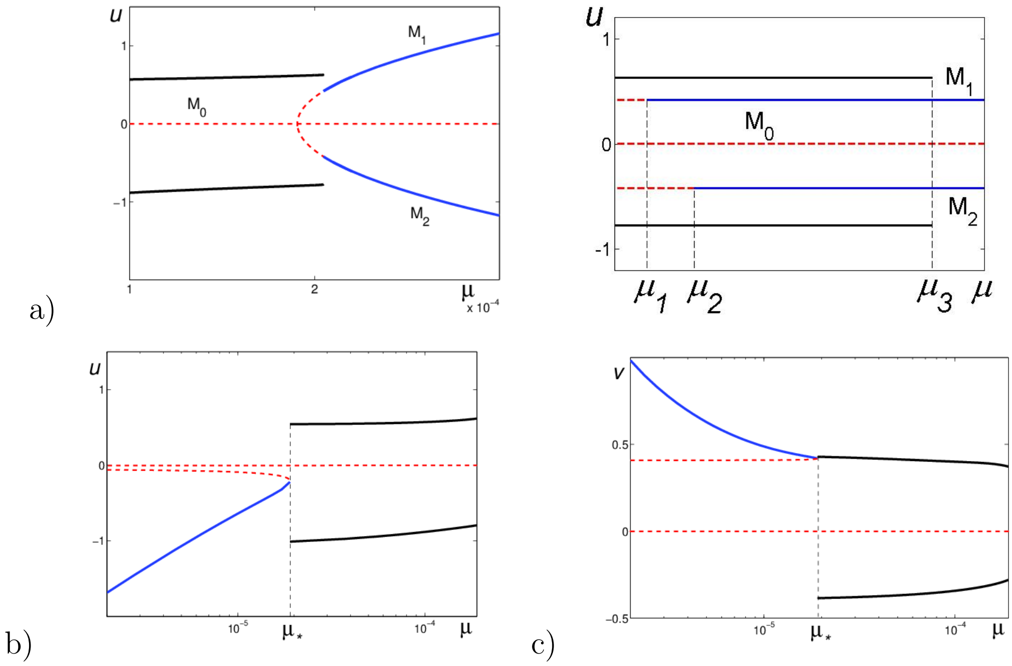

Figure 3.3: The points of extrema of u- and v-coordinates of attractors and repellers for the deterministic system (3.2) are shown as functions of the parameter μ. The stable equilibria (blue), stable limit cycles (black) and unstable equilibria are respectively illustrated by the blue, black and red lines.

Before doing so, consider again the range 10^{-4} y$^{-1} < \mu < 3 \cdot 10^{-4}$ y^{-1}. Fig. 3.3a shows how u depends on μ (an enlarged fragment is shown on the right). In this range, the trivial equilibrium point M_0 is always unstable (dashed line) while the equilibrium point M_1 is unstable for $\mu_0 < \mu < \mu_1 = 2.0436 \cdot 10^{-4}$ y^{-1}, and stable for $\mu > \mu_1$ (upper blue solid line in Fig. 3.3a). The second equilibrium point M_2 is unstable for $\mu_0 < \mu < \mu_2 = 2.0445 \cdot 10^{-4}$ y^{-1}, and stable for $\mu > \mu_2$ (lower blue solid line). The boundary parameter value μ_0, which is defined by the intersection of the red dashed lines, corresponds to a pitchfork bifurcation. In addition, a stable limit cycle exists for $1 \cdot 10^{-4}$ y^{-1} $\leq \mu < \mu_3 = 2.049 \cdot 10^{-4}$ y^{-1}; the limits of this cycle in the $u-$space are shown by the two black solid lines. The cycle disappears at a saddle-node bifurcation $\mu = \mu_3$. In summary, the system is monostable for $1 \cdot 10^{-4}$ y$^{-1} \leq \mu < \mu_1$ (the single attractor is a limit cycle), has two stable equilibria for $\mu_3 < \mu \leq 3 \cdot 10^{-4}$ y^{-1}, and for $\mu_1 < \mu < \mu_3$, the stable limit cycle coexists with two stable equilibrium points. Above μ_3, the two stable points $M_{1,2}$ constitute the only attractors.

Fig. 3.3b and c allow us to explore the range $\mu < 1 \cdot 10^{-4}$. We already identified the bifurcation point μ_* at which the two non-trivial fixed points disappear. They give way to the limit cycle already described and for $\mu < 1 \cdot 10^{-4}$. This type of bifurcation is called a saddle-node bifurcation on an invariant cycle (SNIC).

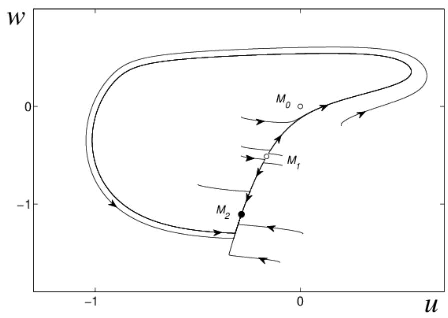

Figure 3.4: The phase trajectories of the deterministic system (3.1) shown in the $u - w$ plane for $\mu = 0.18 \cdot 10^{-4}$ y^{-1}. The point M_2 of stable equilibrium is illustrated with the black circle while the points M_0 and M_1 of unstable equilibria shown by the open circles.

Fig. 3.4 gives the phase diagram for $\mu = 0.18 \cdot 10^{-4}$ y^{-1}. The unstable equilibrium M_1 lies on a surface separating long and short migrations of phase trajectories towards the stable equilibrium M_2. Trajectories starting above M_1 follows a long path to M_2 via the upper route. Trajectories starting below M_1 reach M_2 via the short, lower route.

Fig. 3.5 then shows the oscillations associated with the limit cycle for different values of μ, just above the bifurcation point. As μ increases, the u- and v-oscillations change little, but those of w decrease, which is intuitively reasonable given that the relaxation time of ocean temperature decreases.

Figure 3.6 shows time series for different values of μ, below and above $\mu = 1 \cdot 10^{-4}$ y. Remember that in this model, marine and continental ice masses cause ocean warming. This is certainly speculative but consider this mechanism as instant. The parameter μ defines the response time of the ocean, which may either be very low (cases (a) or (b)) or more faster (cases (c) and (d)). The phases lag is the one which creates the possibility of a catastrophic and, admittedly, unrealistically abrupt deglaciations separated by long phases

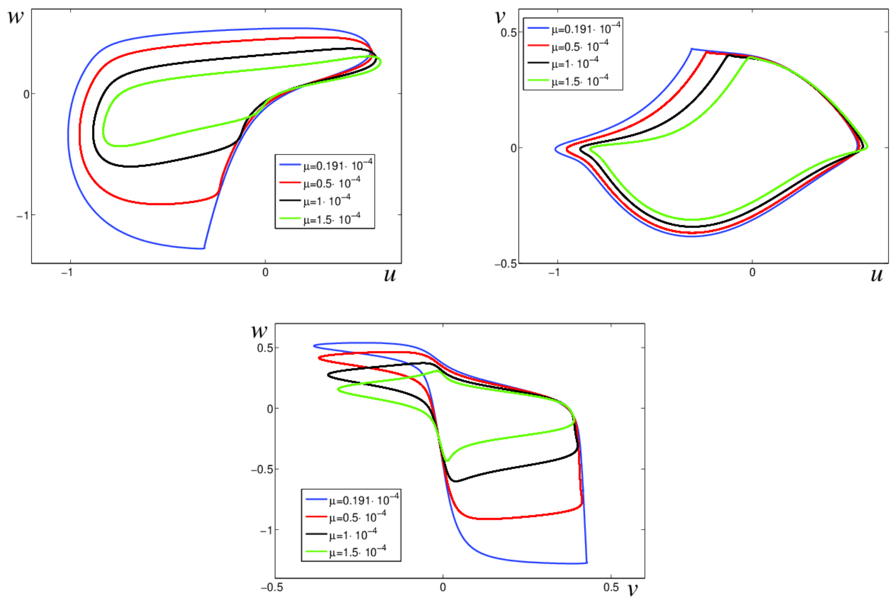

Figure 3.5: The phase portraits of the deterministic model.

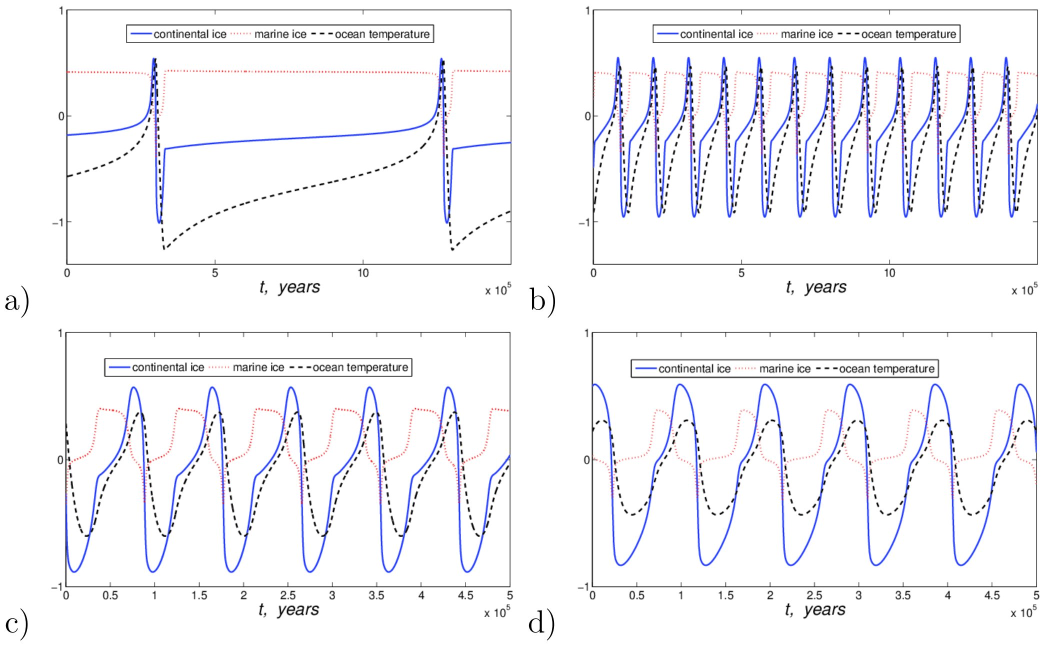

Figure 3.6: The time series illustrated for various μ: a) $\mu = 0.2 \cdot 10^{-4}$ y^{-1}, b) $\mu = 0.5 \cdot 10^{-4}$ y^{-1}, c) $\mu = 1 \cdot 10^{-4}$ y^{-1}, and d) $\mu = 1.5 \cdot 10^{-4}$ y^{-1}.

of latency (in (a)) and, for higher values of μ, back-and-through in the vicinity of what will become fixed points M_1 and M_2.

The period of the oscillation is reasonably constant for a wide range of μ, but increases near μ_*, which is characteristic for a saddle-node bifurcation of invariant cycle.

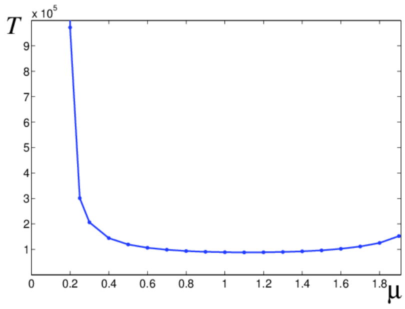

Figure 3.7: The period T of self-oscillations (in y) as a function of μ (in y^{-1}).

3.1.2 Mixed-mode oscillations and noise-induced chaos

Similar to the method followed in section 2, we consider the effects of stochastic forcing. Additive noise is introduced this time in the equation for ocean temperature, which, we considered, is physically the most reasonable option. Following [46], this may be seen as a way to represent the internal forcing due to atmospheric fluctuations. Consider a system

$$\begin{aligned} \dot{x} &= a_0 x + a_1(1 - a_2 y)y - a_3 z, \\ \dot{y} &= b_0 x + b_1(1 - b_2 y - b_3 y^2 - b_4 x^2)y - b_5 z, \\ \dot{z} &= c_0 x + c_1 y - \mu z + \varepsilon\xi(t), \end{aligned} \tag{3.3}$$

where ε parameterises the noise intensity and $\xi(t)$ stands for an uncorrelated white Gaussian noise.

Consider, first, the regime $\mu > \mu_3$ (short ocean relaxation time, two fixed points Figs. 3.8 and 3.9). Phase trajectories of the deterministic system reaching M_1 and M_2 are in blue and red, respectively. A saddle surface, also called separatrix, divides the corresponding basins of attraction. It contains the unstable equilibrium point M_0. Consider, first, the noisy trajectories reaching M_1. At small noise intensity, they remain within the vicinity of the attractor (Fig. 3.8b,c $\varepsilon = 0.0002$, green colour), thereby describing small-amplitude stochastic oscillations, which we already introduced with the acronym SASO. The dispersion radius increases with noise intensity. At some point, trajectories cross the separatrix, thus moving into the basin of attraction of M_2, from where they may return to the basin of M_1, again provided enough stochastic forcing. Such back-and-through between the two basins of attraction are large-amplitude stochastic oscillations (LASO), akin of stochastic jumps between two potential wells (Fig. 3.8). How much stochastic forcing in needed to excite LASO depends on μ. Less noise is needed when μ is near the bifurcation μ_3. At this point, the two fixed points merge, and the potential barrier vanishes.

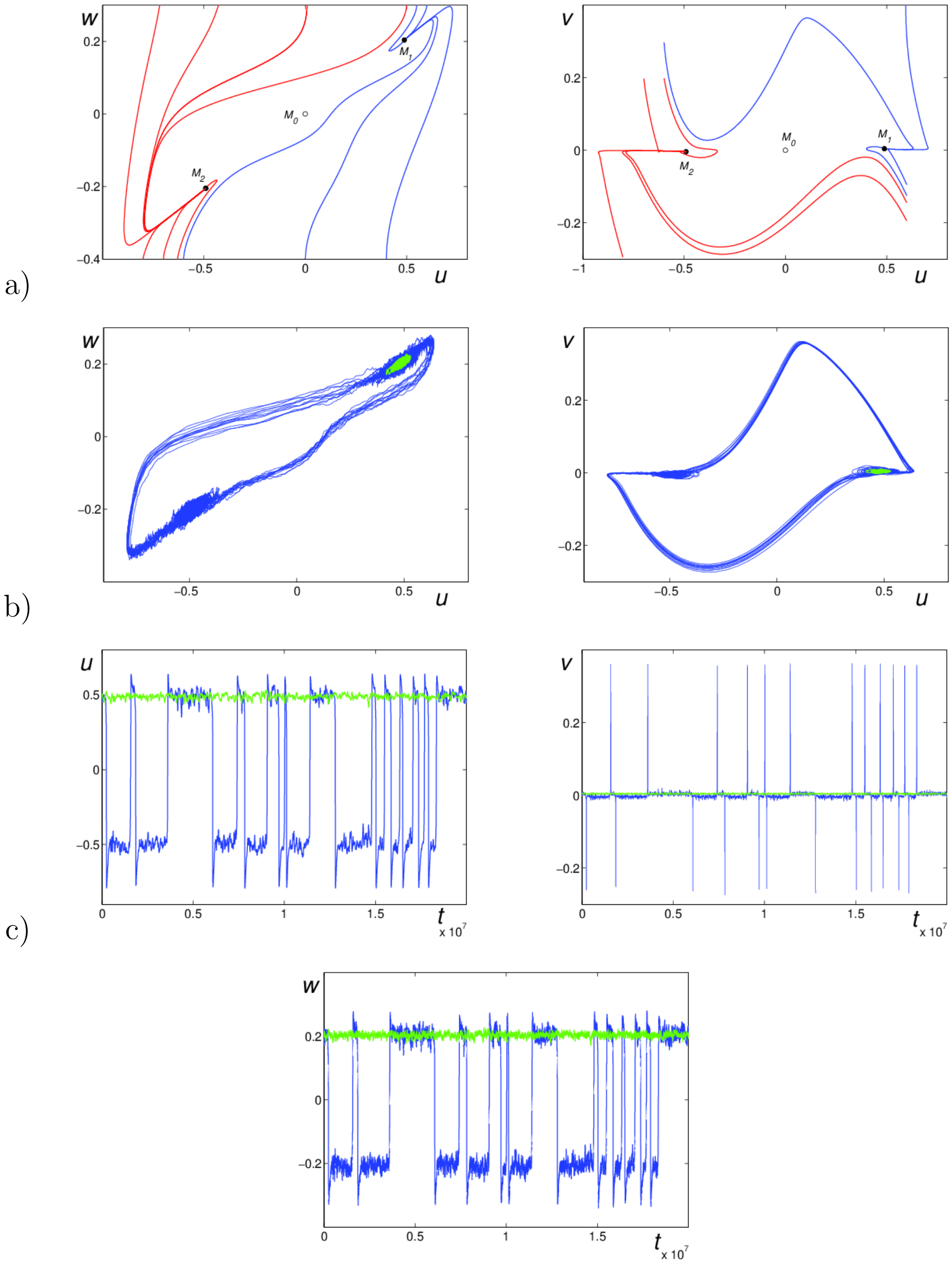

Figure 3.8: The phase portraits and time series with $\mu = 2.1 \cdot 10^{-4}$ y^{-1}: a) projections for the deterministic model; b) stochastic trajectories for $\varepsilon = 0.0002$ (green), $\varepsilon = 0.0005$ (blue), and c) time evolution (t measured in years).

Away from this bifurcation point, however, we do not necessarily expect transition probabilities to be symmetric. They will be determined by the structure of the deterministic vector field. This is what we address now, with a method called "stochastic sensitivity analysis".

The theoretical background of the technique applied here is available in Appendices A and B.

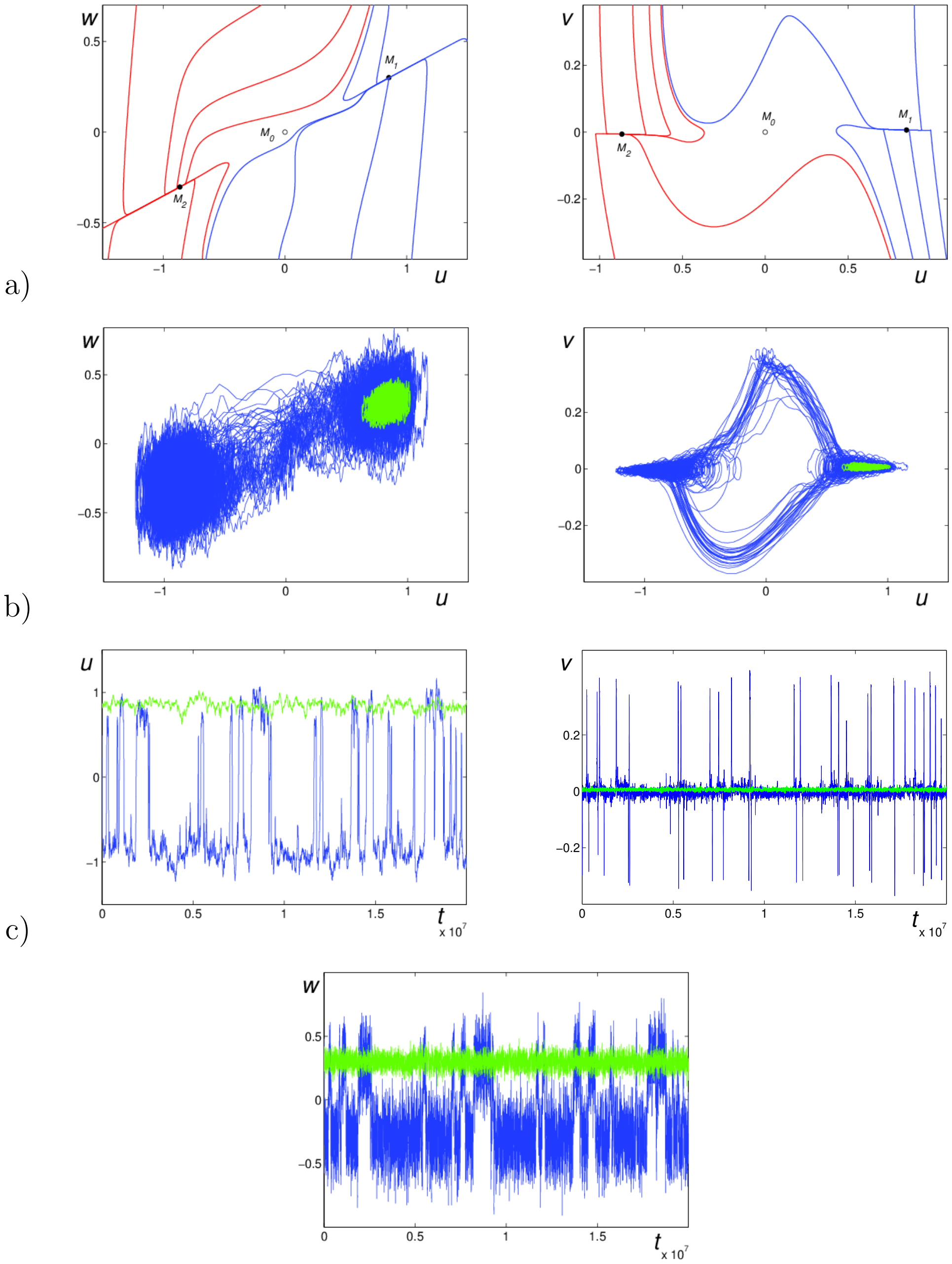

Figure 3.9: The phase portraits and time series with $\mu = 2.5 \cdot 10^{-4}$ y^{-1}: a) projections for the deterministic model; b) stochastic trajectories for $\varepsilon = 0.003$ (green), $\varepsilon = 0.01$ (blue), and c) time evolution (t measured in years).

Consider the 3×3-matrix W, defined as the solution

$$FW + W\,F^{\top} + S = 0,$$

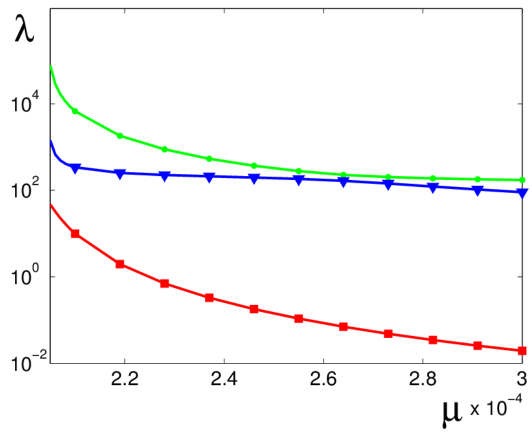

Figure 3.10: Stochastic sensitivity of the equilibrium point M_1.

where for system (3.3)

$$F = \begin{pmatrix} f_{11} & f_{12} & f_{13} \\ f_{21} & f_{22} & f_{23} \\ f_{31} & f_{32} & f_{33} \end{pmatrix}, \quad S = \begin{pmatrix} 0 & 0 & 0 \\ 0 & 0 & 0 \\ 0 & 0 & 1 \end{pmatrix},$$

$$f_{11} = a_0, \quad f_{12} = a_1 - 2a_1a_2y, \quad f_{13} = -a_3,$$

$$f_{21} = b_0 - 2b_1b_4xy, \quad f_{22} = b_1(1 - 2b_2y - 3b_3y^2 - b_4x^2), \quad f_{23} = -b_5,$$

$$f_{31} = c_0, \quad f_{32} = c_1, \quad f_{33} = -c_2.$$

The object W is called the stochastic sensitivity matrix. Let its eigenvalues (ranked in decreasing amplitudes) be $\lambda_1,\ \lambda_2,\ \lambda_3$, associated with the orthonormal eigenvectors $h_1,\ h_2,$ and h_3. The eigenvalue λ_i quantifies the dispersion of random states $\mathbf{x} = (v, u, w)^\top$ near the equilibrium point $\bar{\mathbf{x}} = (\bar{v}, \bar{u}, \bar{w})^\top$, in the the directions $h_i :\ \mathrm{E}(\mathbf{x} - \bar{\mathbf{x}}, h_i)^2 \approx \varepsilon^2\lambda_i$. Eigenvalues for M_1 are shown on Fig. 3.10, for different values of μ. One can see that the stochastic sensitivity of equilibrium M_1 decreases in all directions as μ increases. The dispersion is heavily directional, with $\lambda_3 \ll \lambda_1$ and $\lambda_3 \ll \lambda_2$.

The probabilistic distribution of random states near M_1 can be estimated with unit spheres in Mahalanobis metrics (see Appendix B for details), defined by the

$$(\mathbf{x} - \bar{\mathbf{x}}, W^{-1}(\mathbf{x} - \bar{\mathbf{x}})) = 1.$$

The sphere corresponds to ellipsoids in the Euclid metrics, defined with:

$$\frac{\beta_1^2}{\lambda_1} + \frac{\beta_2^2}{\lambda_2} + \frac{\beta_3^2}{\lambda_3} = 1, \tag{3.4}$$

where $\beta_i = (\mathbf{x} - \bar{\mathbf{x}}, h_i)$. The coordinates β_i of the ellipsoid are determined with the following two-parametric expressions

$$\beta_1 = \sqrt{\lambda_1}\sin\varphi\sin\psi, \quad \beta_2 = \sqrt{\lambda_2}\cos\varphi\sin\psi,$$

$$\beta_3 = \sqrt{\lambda_3}\cos\psi,\quad 0 \le \varphi \le 2\pi,\quad 0 \le \psi \le 2\pi.$$

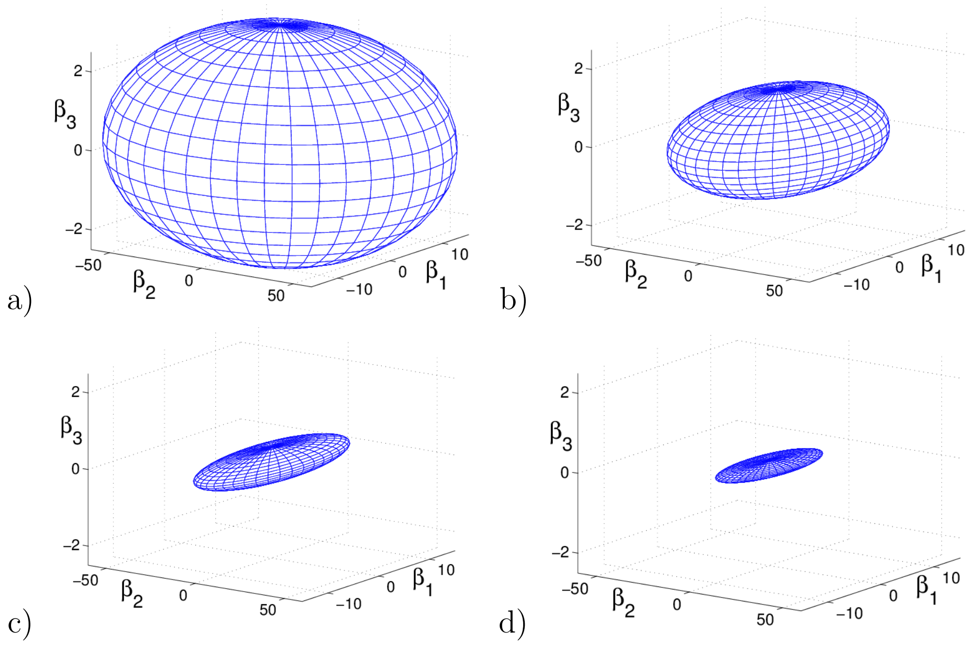

Figure 3.11: The ellipsoids associated with the unit spheres in Mahalanobis metrics for a) $\mu = 2.1 \cdot 10^{-4}$ y^{-1}, b) $\mu = 2.2 \cdot 10^{-4}$ y^{-1}, c) $\mu = 2.3 \cdot 10^{-4}$ y^{-1}, and d) $\mu = 3 \cdot 10^{-4}$ y^{-1}.

Fig. 3.11 shows the ellipsoids for different parameters μ ($\sqrt{\lambda_i}$ are the semi-axes), and, again, their size decreases with increasing the parameter μ.

The dispersion of random states in the 3D-space may now be visualised with 2-D sections. Let Π_{ij} be a plane defined by the equilibrium M_1 and eigenvectors h_i, h_j. The confidence ellipse in the plane Π_{ij} is defined as:

$$\frac{\beta_i^2}{\lambda_i} + \frac{\beta_j^2}{\lambda_j} = 2\varepsilon^2 \ln \frac{1}{1-P}, \tag{3.5}$$

where P stands for a fiducial probability. The plane Π_{ij} may be thought of as a Poincaré section, with sections Π_{12} and Π_{13} shown on 3.12. The ellipses capture nicely the random trajectories simulated by integrating the stochastic dynamical system, giving us confidence in the approach. Again, the dispersions in the direction h_1 are greatest, thus *a priori* most likely to trigger LASO. For this reason we concentrate in the following in the Π_{12} and Π_{13} sections.

The effects of noise now be understood by considering how the confidence ellipses fit in the vector field (Fig. 3.13). Consider the fixed point M_1. At low noise, the confidence ellipse lies in the basin of attraction of the equilibrium point. Only SASO are produced. With increasing noise intensity, it outgrows the basin of attraction and allows the excitation of LASO: trajectories leave the basin of attraction of M_1 and reach the domain of M_2. Again, more noise is needed to produce LASO away from the bifurcation point.

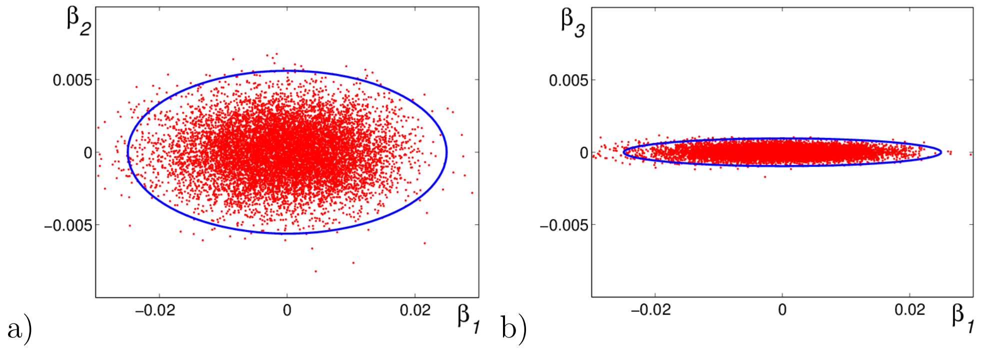

Figure 3.12: The random states (red) and confidence ellipses (blue) in the sections Π_{12} (left) and Π_{13} (right) for $\mu = 2.1 \cdot 10^{-4}$ y^{-1}, $P = 0.99$, $\varepsilon = 0.0001$.

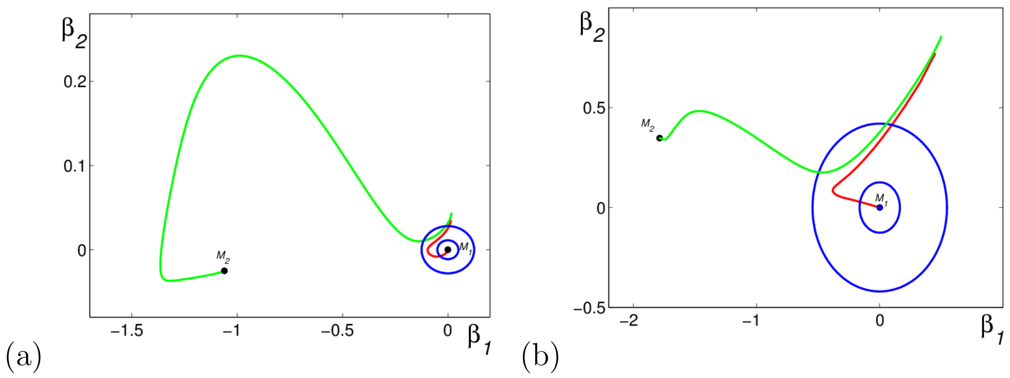

Figure 3.13: The phase trajectories and confidence ellipses for $P = 0.99$ and a) $\mu = 2.1 \cdot 10^{-4}$ y^{-1}, $\varepsilon = 0.0002$ (small ellipse), $\varepsilon = 0.0005$ (large ellipse); b) $\mu = 2.5 \cdot 10^{-4}$ y^{-1}, $\varepsilon = 0.003$ (small ellipse), $\varepsilon = 0.01$ (large ellipse). The confidence ellipses for fiducial probabilities $P = 0.99$ are shown by the blue lines and the trajectories going to M_1 and M_2 are shown by the red and green lines, respectively.

In the parametric region $10^{-4} \leq \mu < \mu_1$, the deterministic model has one limit cycle attractor. With low noise intensity, the phase trajectories remain around the deterministic cycle (Fig. 3.14 and Fig. 3.15). The stochastically-forced climate model has thus noisy, but nearly periodic oscillations which can be qualified as LASO. The thickness of stochastic bundle around the deterministic cycle grows with increasing noise intensity. The stochastic forcing therefore causes small oscillations within one cycle, so that one can say that SASO appear along the LASO. The response at higher noise levels slightly differs whether $\mu < \mu_0$ (one unstable equilibrium M_0, Fig. 3.14) or $\mu_0 < \mu < \mu_1$ (three unstable equilibria, Fig. 3.15).

For the higher value of μ, trajectories tend to spend more time around the unstable equilibria, creating more opportunities for SASO. Furthermore, these small oscillations tend to hasten the transition between the regions around

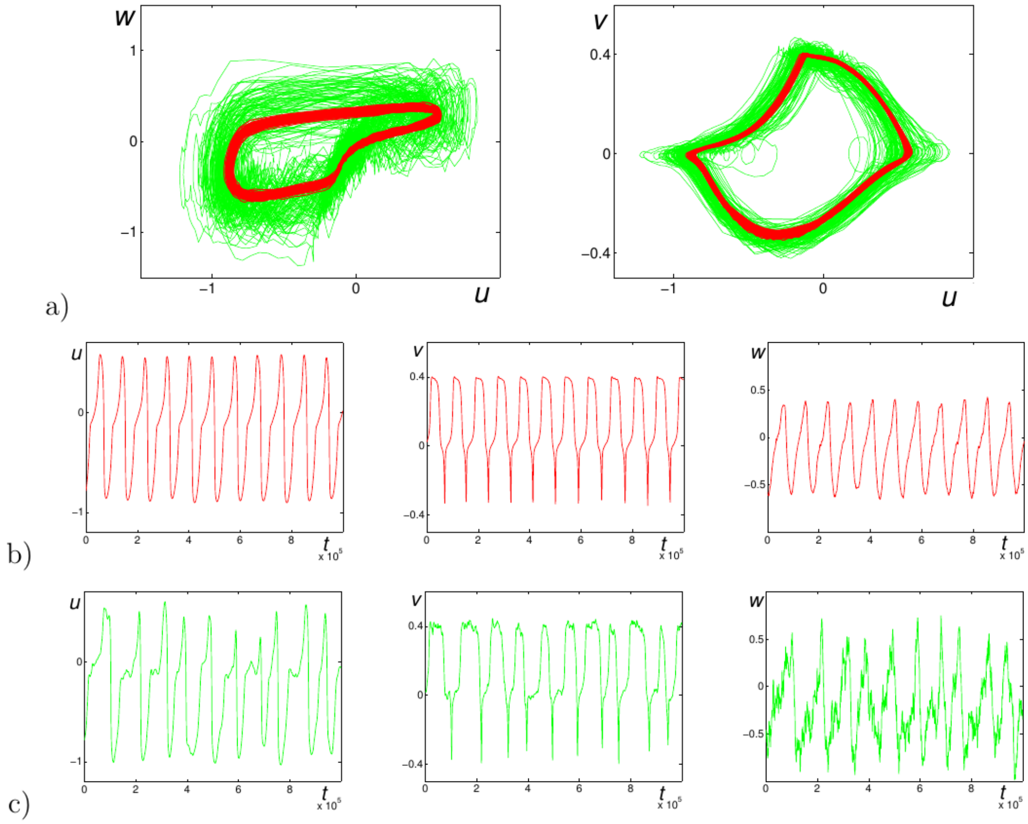

Figure 3.14: The stochastic trajectories for $\mu = 1.0 \cdot 10^{-4}$ y^{-1}, $\varepsilon = 0.001$ (red), $\varepsilon = 0.01$ (green) and corresponding time series (t measured in years).

the two unstable points M_1 and M_2 and reduce the duration of the LASO, compared to the duration of limit cycle of the corresponding deterministic system. This is well seen by considering the mean value T of time intervals between successive intersections of a phase trajectory with the Poincare plane $u = 0$ (from minus to plus, Fig. 3.16). With no noise, T is the period of the deterministic limit cycle, which increases to infinity as μ approaches μ_3, the point at which the deterministic limit cycle vanishes. Around this critical value, the stochastic forcing effectively decreases the period of the cycle, the more strongly that noise intensity is high, and it also allows the persistence of LASO beyond the bifurcation point.

Let us now focus on the region $\mu < \mu_*$, where the deterministic equations have one point of stable equilibrium. We have acknowledged that this regime no longer realistically describes glacial-interglacial cycles, but it may still be insightful for thinking about climate phenomena involving rapid dynamics separated by latency periods.

With small enough noise, SASO appear in the vicinity the stable equilibrium M_2 (green lines in Fig. 3.17 for $\mu = 0.18 \cdot 10^{-4}$ and $\mu = 0.19 \cdot 10^{-4}$ y^{-1}). LASO appear at larger intensities (blue and red lines), which originate in the

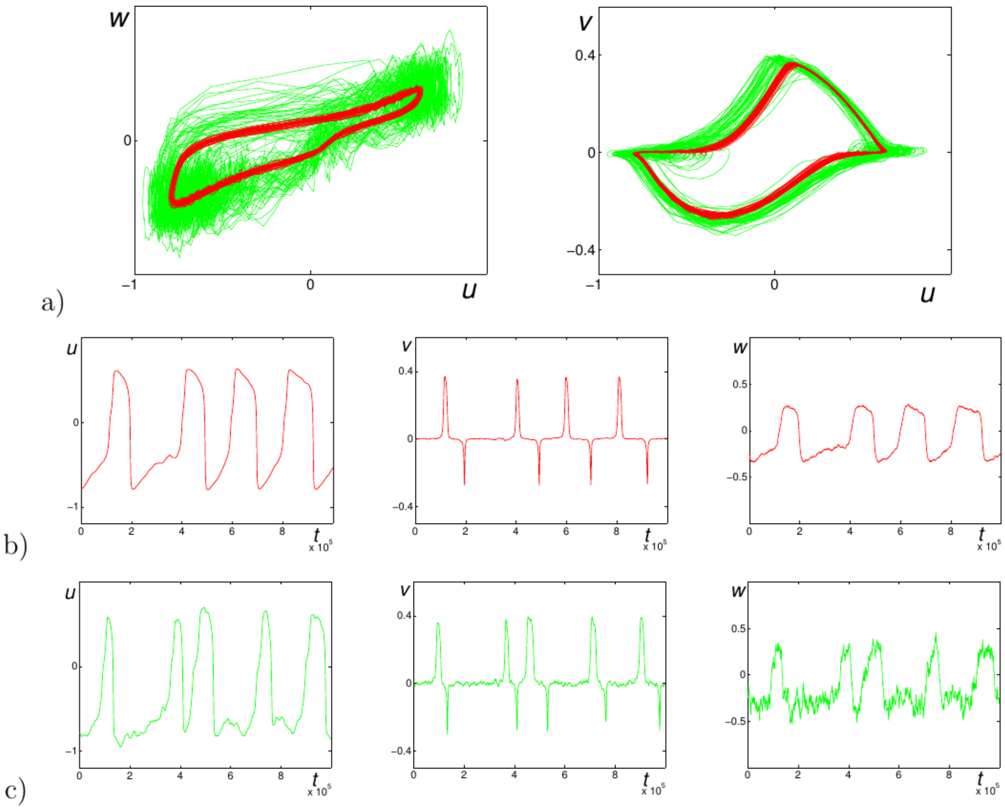

Figure 3.15: The stochastic trajectories for $\mu = 2.0 \cdot 10^{-4}$ y^{-1}, $\varepsilon = 0.0005$ (red), $\varepsilon = 0.005$ (green) and corresponding time series (t measured in years).

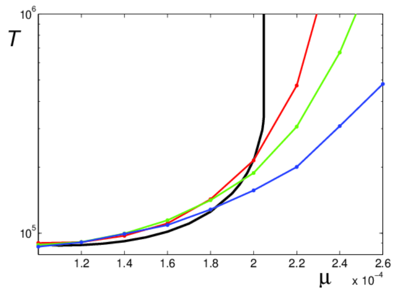

Figure 3.16: The mean value of time intervals between intersections of a phase trajectory with the Poincare plane $u = 0$ (from minus to plus) for $\varepsilon = 0$ (black), $\varepsilon = 0.01$ (red), $\varepsilon = 0.02$ (green), $\varepsilon = 0.03$ (blue).

region of stable equilibrium.

Small deviations from the stable equilibrium relax monotonically to this point (SASO). Large deviations bring the system state beyond M_1, from which it is forced to take the long route towards M_2. This long route (Fig. 3.18) is in fact similar to the limit cycle, which exists on the other side of the bifurcation point μ_*. Hence, the form of the LASO excitation is related to the limit cycle, which appears at bifurcation, and the threshold for the excitation of LASO is

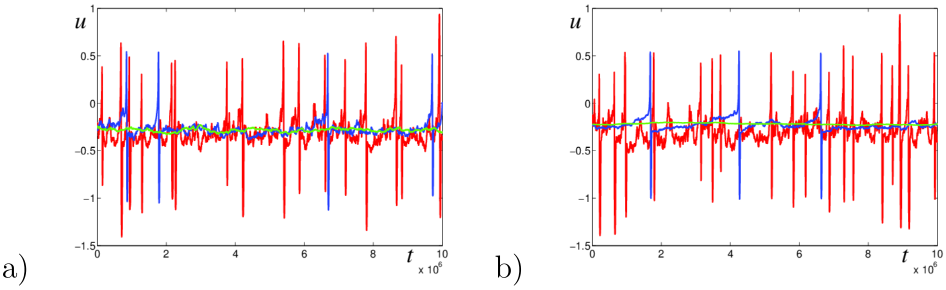

Figure 3.17: u-time series for a) $\mu = 0.18 \cdot 10^{-4}$ y^{-1} and $\varepsilon = 0.001$ (green), $\varepsilon = 0.003$ (blue), $\varepsilon = 0.01$ (red); b) $\mu = 0.19 \cdot 10^{-4}$ y^{-1} and $\varepsilon = 0.0001$ (green), $\varepsilon = 0.001$ (blue), $\varepsilon = 0.01$ (red).

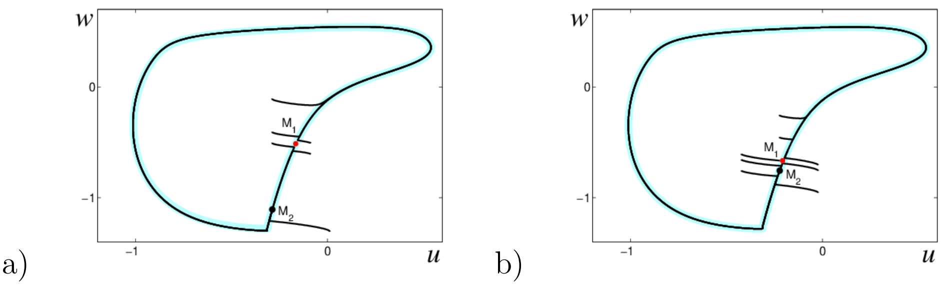

Figure 3.18: The phase trajectories (black thin lines) for the deterministic system with a) $\mu = 0.18 \cdot 10^{-4}$ y^{-1} and b) $\mu = 0.19 \cdot 10^{-4}$ y^{-1}. The stable equilibrium point M_2 is illustrated by the black circle and unstable equilibrium point M_1 is shown by the red circle. The blue thick closed lines represent the $u - w$-projections of the limit cycle for $\mu = 0.191 \cdot 10^{-4}$ y^{-1}.

determined by the distance between M_1 and M_2. This distance vanishes at the bifurcation point μ_*, where the deterministic limit cycle appears.

The SASO regime, at low noise, is thus the one obtained where the "long route" is never excited. The LASO regime, at high noise, consists in a perpetual excitation of the limit cycle, and is therefore qualitatively similar to the deterministic regime found beyond the bifurcation point. The mixed-mode regime occurs in between. The limit cycle is not-so-frequently excited, thereby yielding intermittency (Fig. 3.17). The LASO are rare spikes interrupting SASO phases. The length of the SASO phases decreases with increasing noise intensity (Fig. 3.20).

For characterising this intermittency further, we define the time points t_k of the intersection of the surface $u = 0$ as random spike intervals, and define the sequence $\tau_k = t_k - t_{k-1}$ as the interspike intervals (ISI). The mixed-mode scenario containing the intermittency of SASO and LASO can now be described by the mean value $m = \mathrm{E}\tau$ and dispersion $D = \mathrm{E}(\tau - m)^2$ of interspike intervals (Fig. 3.20). The mean value of ISI reduces and approaches

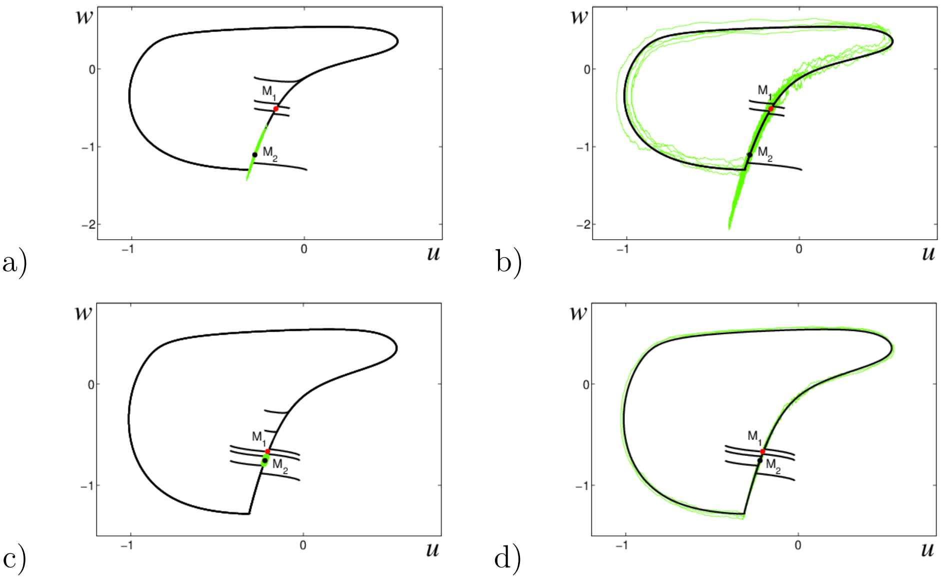

Figure 3.19: Transition mechanism between SASO and LASO at small μ: the green and black lines illustrate the stochastic and deterministic phase trajectories, the stable and unstable equilibria, M_2 and M_1 are shown by the black and red circles, respectively, $\mu = 0.18 \cdot 10^{-4}$ y^{-1} (upper panel) and $\mu = 0.19 \cdot 10^{-4}$ y^{-1} (lower panel). The noise intensities are a) $\varepsilon = 0.001$, b) $\varepsilon = 0.003$, c) $\varepsilon = 0.0001$, and d) $\varepsilon = 0.001$.

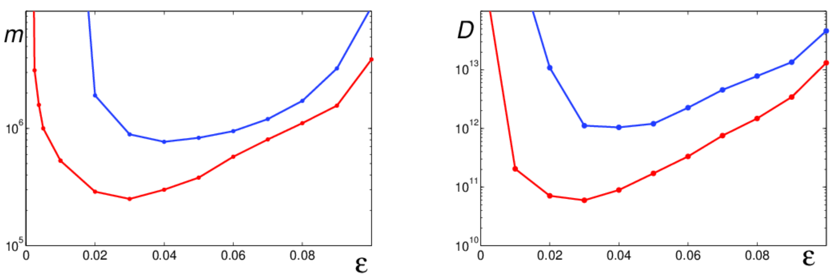

Figure 3.20: The mean value m and dispersion D of interspike intervals for $\mu = 0.1 \cdot 10^{-4}$ y^{-1} (blue) and $\mu = 0.18 \cdot 10^{-4}$ y^{-1} (red) as functions of noise intensity.

$2 \cdot 10^5$ y (close to the period of deterministic fluctuations for $\mu > \mu_*$) as a result of noise-induced forcing at $\mu = 0.18 \cdot 10^{-4}$ y^{-1}. ISI increases at lower noise levels, because the limit cycle is less and less frequently excited, leading to more rare LASO excursions. The minimum in dispersion D (Fig. 3.20) corresponds to the phenomenon of coherence resonance [74], which happens as a result of LASO-mode formation.

Let us now pay our attention to the parametric region $\mu > \mu_*$ where the deterministic model contains the limit cycle, but still for high relaxation time.

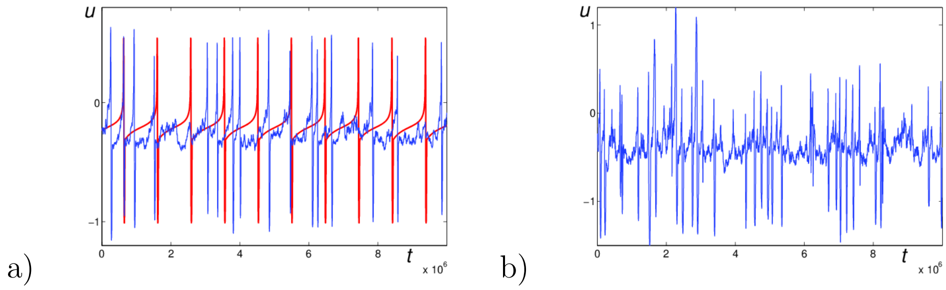

Figure 3.21: Stochastically-induced fluctuations (blue) for $\mu = 0.2 \cdot 10^{-4}$ y^{-1} with a) $\varepsilon = 0.005$, and b) $\varepsilon = 0.02$ (deterministic fluctuations are shown by the red colour).

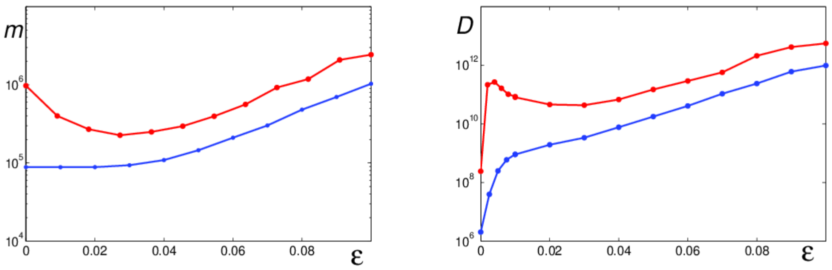

Figure 3.22: The mean value m and dispersion D of interspike intervals for $\mu = 0.2 \cdot 10^{-4}$ y^{-1} (red) and $\mu = 1 \cdot 10^{-4}$ y^{-1} (blue) as functions of noise intensity.

Thus, we are in this regime where catastrophic outbreaks are separated by latency episodes. Fig. 3.21 illustrates the evolutionary behavior of deviations in the continental ice mass (function $u(t)$) for various noise intensities. As we have already observed, the spike episodes which exist in the deterministic model are randomly shifted by noise, and the latency intervals are replaced by the noise-induced fluctuations. Some inter-spike intervals are surprisingly small. Near the bifurcation point (red on Fig. 3.22), even a small amount of noise decreases the mean value of ISI, and increases its variance, which indeed suggests extreme sensitivity. This is expected, if we consider the phase portrait which we examined on the other side of the bifurcation (Fig. 3.19a). In this regime, one stable and unstable fixed point were close to each other, permitting either slow and long excursions when the system was exited by noise. At μ slightly above μ_*, the two points have disappeared, but the system has remained highly sensitive to noise in this region of the phase space. As the noise intensity increases, the variance decreases and the mean value of ISI stabilises. Signs of this extreme sensitivity are also revealed by the analysis of the Lyapunov exponent (Fig. 3.23). A transition to chaos (negative to positive Lyapunov exponent) occurs as ε grows and, again, this transition occurs at smaller values when μ is close to the bifurcation point.

Further away from the bifurcation points (blue curve), the effect of noise consistently and monotonously increases the mean ISI and its variance, and transition to chaos (Fig. 3.23) no longer occurs.

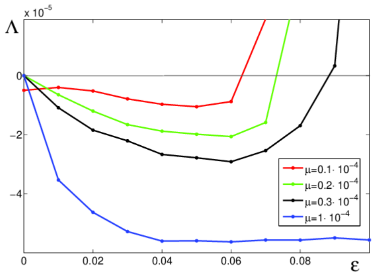

Figure 3.23: The largest Lyapunov exponent illustrating chaotization for $\mu = 0.1 \cdot 10^{-4}$ y^{-1} (red), $\mu = 0.2 \cdot 10^{-4}$ y^{-1} (green), $\mu = 0.3 \cdot 10^{-4}$ y^{-1} (black), and $\mu = 1 \cdot 10^{-4}$ y^{-1} (blue).

3.2 Ice mass – carbon dioxide – mean temperature model

3.2.1 Deterministic model containing a saddle-node bifurcation on an invariant cycle

As a follow-up to the above model, Saltzman and co-authors introduced another model [75] which takes into account explicitly the role of CO_2 as a greenhouse gas forcing — an increase in CO_2 causing a temperature increase, hence ice loss. The equations governing CO_2 is more speculative and Saltzman and co-authors have consistently consider that the dynamics governing CO_2 concentrations are highly linear (cf. [76]). This is controversial and other authors, which acknowledging the greenhouse gas forcing exerted by CO_2, consider that the crucial non-linearity is to be found in other components of the climate system, and specifically, in ice-sheet bedrock dynamics (e.g. [77]). Again, besides the precise attribution of physical phenomena and mechanisms, we are here interested in the possibilities which emerge out of exciting a ice age oscillator with noise. In this spirit, the main interest of the [75] which we study now is to contain a saddle-node bifurcation on an invariant cycle, as we will soon discover.

$$
\begin{aligned}
\dot{x} &= -\alpha_1 y - \alpha_2 z - \alpha_3 y^2, \\
\dot{y} &= -\beta_0 x + \beta_1 y + \beta_2 z - (x^2 + \kappa y^2) y, \\
\dot{z} &= x - \gamma z,
\end{aligned} \tag{3.6}
$$

where the dynamical variables x, y and z respectively describe the non-dimensional deviations of the ice mass, atmospheric carbon dioxide concentration, and deep ocean temperature from the equilibrium state.

The model parameters (coefficients entering in equations (3.6)) were empirically determined to reproduce the observed sequence of glacial-interglacial cycles over the last 400,000 years: $\alpha_1 = 0.4$, $\alpha_2 = 0.1$, $\alpha_3 = 0.012$, $\beta_0 = 10$, $\beta_1 = 3.77$, $\beta_2 = 20$, $\gamma = 1.45$ and $\kappa = 0.004$. In the present analysis we restrict the sensitivity analysis to the system to the parameter γ which, in this model, expresses the reverse relaxation time of the bulk ocean temperature to its mean value.

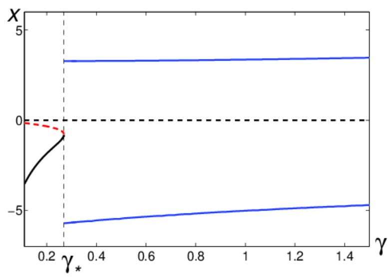

Figure 3.24: Bifurcation diagram of the nonlinear deterministic equations (3.6).

Let us consider the parametric interval $0.1 < \gamma < 1.5$ containing the value $\gamma = 1.45$ used by [75]. Fig. 3.24 illustrates the attractors and repellers of deterministic equations (3.6). An unstable equilibrium point $M_0(0, 0, 0)$ (black dashed line) exists for all values of γ. In addition, the system has a stable equilibrium M_1 (black solid line) and an unstable equilibrium M_2 (red dashed line) for $0.1 < \gamma < \gamma_* \approx 0.2691$. If γ goes to γ_* from the left side, two points, M_1 and M_2, approach and merge at γ_*. As a consequence of this a homoclinic trajectory arises. If $\gamma > \gamma_*$, the equilibrium point $M_1 = M_2$ vanishes and a stable limit cycle originates. The extremal values of x-coordinates corresponding to this cycle are illustrated in Fig. 3.24 by the blue colour. The shape of the cycle under consideration is almost invariant for $\gamma_* < \gamma < 1.5$. If we now focus our attention on the parametric region $0.1 < \gamma < 1.5$, we see that the deterministic model (3.6) has two dynamical regimes. Namely the deviations x, y, and z stabilize to their equilibrium values for $0.1 < \gamma < \gamma_*$ (left subinterval), while they undergo several periodic fluctuations with large amplitudes in the right subinterval. The point γ_* is a bifurcation on an invariante cycle [78], which

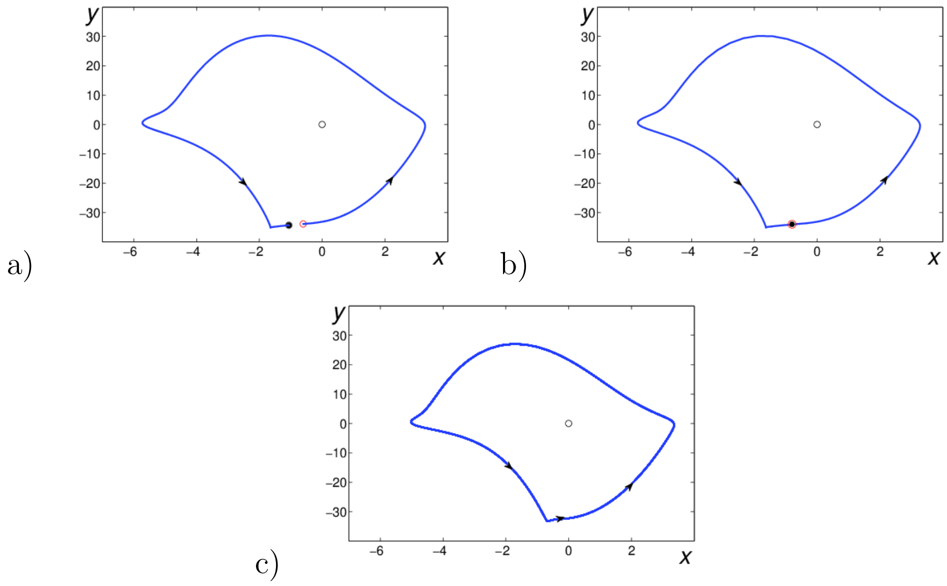

Figure 3.25: A saddle-node bifurcation on an invariant cycle: the phase trajectories are illustrated for a) $\gamma = 0.26$, b) $\gamma = 0.2691$, and c) $\gamma = 1$.

is to be different from the better-known Andronov-Hopf bifurcation. This is a saddle-node bifurcation on an invariant cycle [78]. Some of the peculiarities of this bifurcation are demonstrated in Fig. 3.25: just before the bifurcation, one can find a heteroclinic phase trajectory going from M_2 to M_1 (3.25a), at the bifurcation point, there is a homoclinic phase trajectory (Fig. 3.25b), and beyond it, one finds a limit cycle (Fig. 3.25c). The point M_2 of saddle equilibrium contains a stable manifold connected with a separatrix dividing two zones of the phase space with various dynamical behavior. So, for instance, if an initial point slightly deviates from the point M_1 of stable equilibrium, the corresponding phase trajectory relaxes readily to the point M_1. From the other hand, if the initial point is beyond the system separatrix, the phase trajectory it makes its way to M_1 via a large-amplitude excursion. As the deterministic solution goes to the stable equilibrium in the course of time, the system (3.6) is not oscillatory but it is excitable in the parametric region $\gamma < \gamma_*$.

3.2.2 Stochastic excitability: from equilibria to oscillations

We introduce additive noise in the third equation, as a representation of

$$\begin{aligned}
\dot{x} &= -\alpha_1 y - \alpha_2 z - \alpha_3 y^2, \\
\dot{y} &= -\beta_0 x + \beta_1 y + \beta_2 z - (x^2 + \kappa y^2) y, \qquad (3.7) \\
\dot{z} &= x - \gamma z - \varepsilon z \xi,
\end{aligned}$$

where again ξ represents a standard Gaussian white noise with parameters $\mathrm{E}\xi(t) = 0$, $\mathrm{E}\xi(t)\xi(\tau) = \delta(t-\tau)$ and ε stands for the noise intensity. The system (3.7) can be derived from the deterministic system (3.6) by substituting γ by $\gamma + \varepsilon\xi$: it therefore describes the effects of a stochastic perturbation of γ. We analyse the system for $\gamma < \gamma_*$, where the deterministic equations contain the point M_1 of stable equilibrium (single attractor).

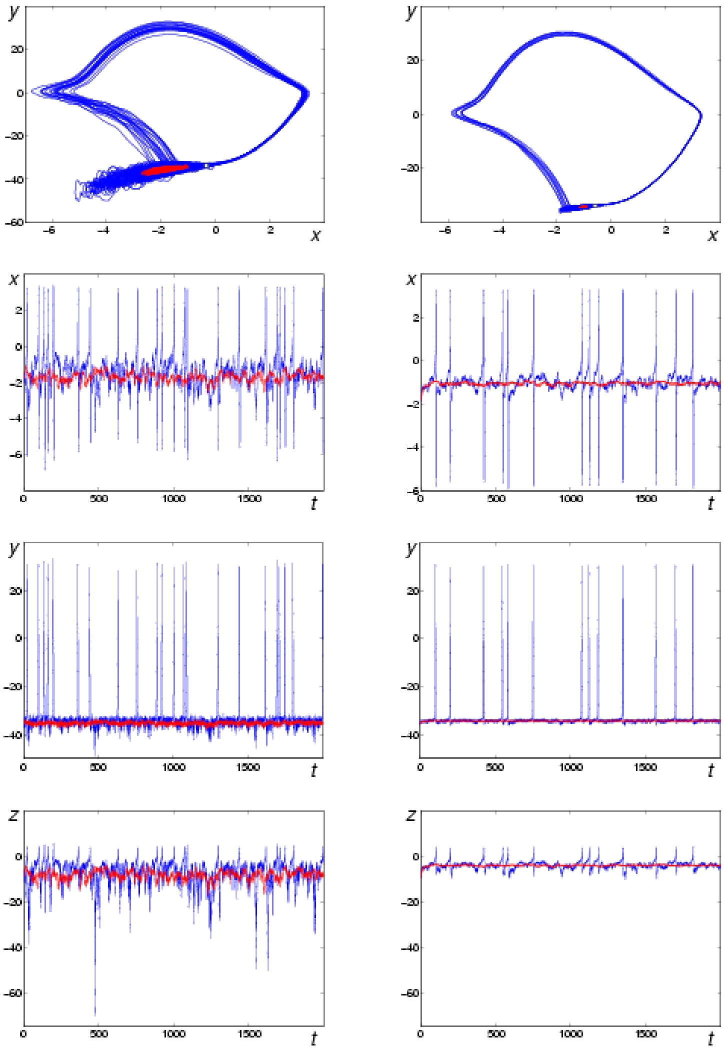

Figure 3.26: Noise-induced evolution of system (3.7) for $\gamma = 0.2$ (left panel) and $\gamma = 0.26$ (right panel). The left panel is plotted for $\varepsilon = 0.1$ (red), $\varepsilon = 0.3$ (blue), and the right panel is drawn for $\varepsilon = 0.02$ (red), $\varepsilon = 0.1$ (blue).

The characteristics of the noise-induced equations (3.7) depend on ε. If ε is small enough, the random trajectories remain localised in the the vicinity of M_1. The reader is now able to anticipate what goes on for higher noise levels: the random trajectories cross the system separatrix going through the saddle M_2, and reach the vicinity of point M_1 only after a long excursion. Phase portraits and time series or shown in Fig. 3.26 for $\gamma = 0.2$ and $\gamma = 0.26$. How

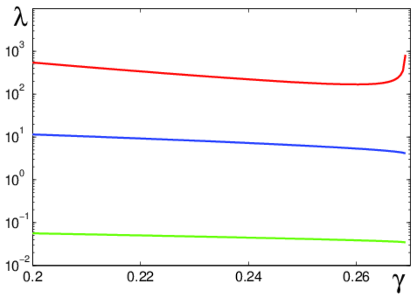

Figure 3.27: A stochastic sensitivity of equilibria.

much noise is needed to excite the long excursion (blue in Fig. 3.26) depends on γ: it is $\varepsilon = 0.3$ for $\gamma = 0.2$ and $\varepsilon = 0.1$ for $\gamma = 0.26$. SASO dominate below this threshold ("sub-threshold regime"); LASO dominate above this threshold ("super-threshold regime"). Near the threshold, LASO appear intermittently. The threshold is smaller near the bifurcation point for at least two reasons. First, the gap between M_1 and M_2 is reduced when $\gamma \to \gamma_*$, and is therefore easier to cross. The second reason is that the stochastic sensitivity of the equilibrium M_1, which determines the dispersion of random states in the vicinity of M_1 for a fixed value of ε, is largest near the bifurcation. We examine this point now.

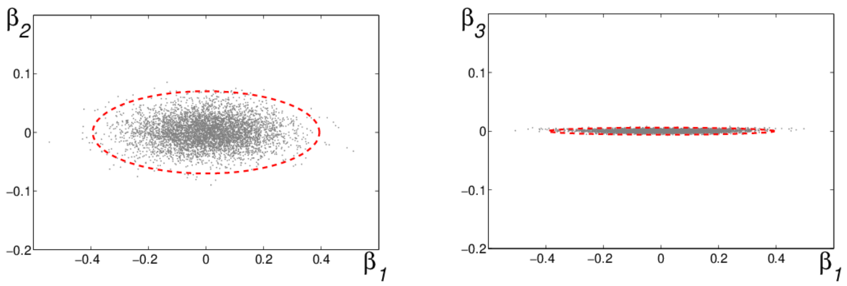

Figure 3.28: Random states and confidence ellipses for $\gamma = 0.26$, $P = 0.99$, and $\varepsilon = 0.01$.

3.2.3 Prediction of the excitement via stochastic sensitivity analysis

Let us consider the eigenvalues $\lambda_1(\gamma) > \lambda_2(\gamma) > \lambda_3(\gamma)$ of the stochastic sensitivity matrix W for the equilibrium point M_1 of equations (3.7) in Fig. 3.27 (λ_1 grows to infinity as γ approaches the bifurcation parameter γ_*). The spatial distribution of random states can be analyzed by means of the confidence domains technique (see for details Appendix B) based on the eigenvalues λ_i, and the corresponding eigenvectors h_i of the matrix W. Fig. 3.28 shows the

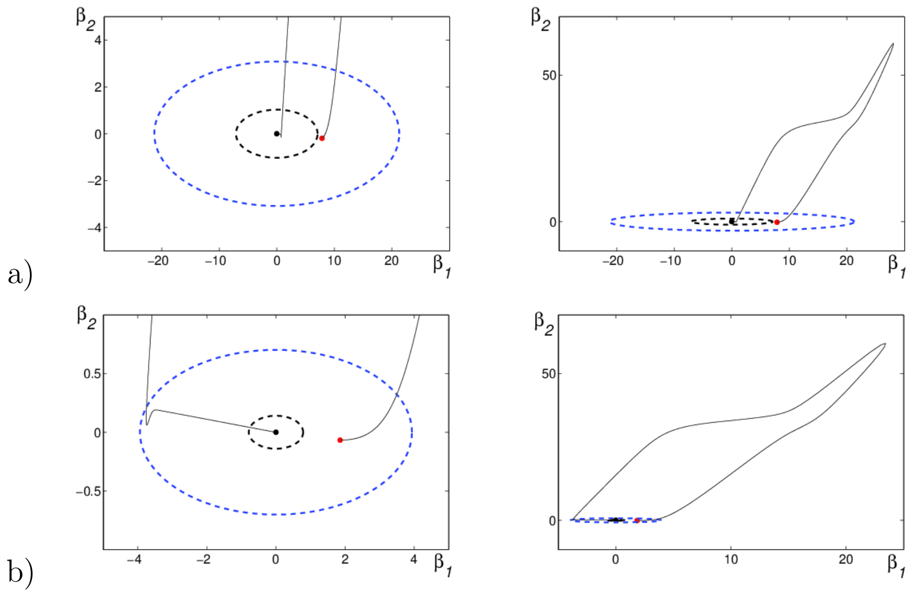

Figure 3.29: Confidence ellipses in the system (3.7) for a) $\gamma = 0.2$, $\varepsilon = 0.1$ (black), $\varepsilon = 0.3$(blue); b) $\gamma = 0.26$, $\varepsilon = 0.02$ (black), $\varepsilon = 0.1$ (blue).

random states and confidence ellipses in the plain sections Π_{12} and Π_{13} (Π_{ij} is a plane determined by M_1 and the coordinate eigenvectors h_i, h_j, and β_i are the corresponding coordinates in these planes). The λ_i differ by several orders of magnitude. Specifically, the dispersion of random states along h_1 and h_2 exceeds the dispersion in the direction h_3 because $\lambda_1 \gg \lambda_3$ and $\lambda_1 \gg \lambda_2$. We may therefore safely concentrate on the Poincare section Π_{12}. For analysing the noise-induced transitions between SASO and LASO, we focus on the position of the unstable equilibrium point M_2 with respect to the confidence ellipses near the stable equilibrium point M_1 (see Fig. 3.29a, obtained for $\gamma = 0.2$). The confidence ellipse is concentrated in the subthreshold region if ε is small enough ($\varepsilon = 0.1$). It then grows, crosses the unstable equilibrium point M_2 and reaches the superthreshold region around $\varepsilon = 0.3$: phase trajectories under the influence of noise are thus highly likely to leave M_1 and follow a large-amplitude return path towards M_1 by means of a large-amplitude return path to M_1. A similar case is illustrated in Fig. 3.29b for $\gamma = 0.26$. As can be seen, the closer γ to the bifurcation point the smaller noise causes the transition to LASO. These theoretical considerations agree nicely with the numerical simulations presented in Fig. 3.26, making us confident that the stochastic sensitivity approach and confidence ellipses are adequate to predict the stochastically-induced excitability in this model.

In summary, the model (3.7) under the influence of random disturbances produces the large-amplitude spikes with sufficient noise excitation, and intermittency is most likely to occur near the saddle-node bifurcation of an invariante cycle. Fig. 3.30 shows the probability density function $p(x, y)$ of

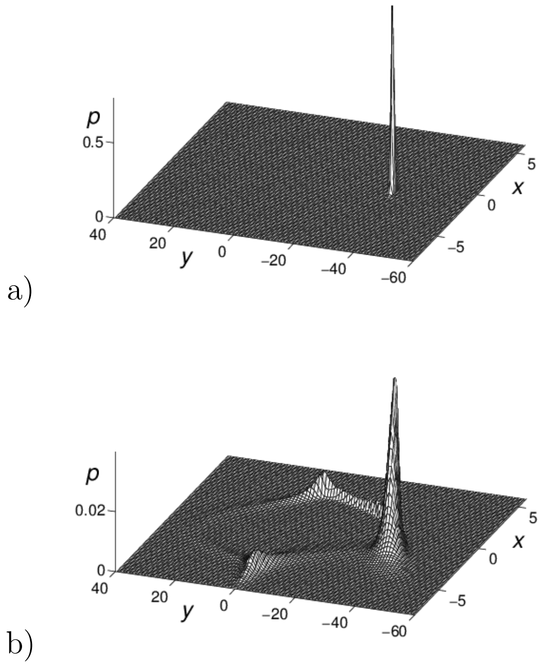

Figure 3.30: The probability density functions for $\gamma = 0.26$ and a) $\varepsilon = 0.05$, b) $\varepsilon = 0.6$.

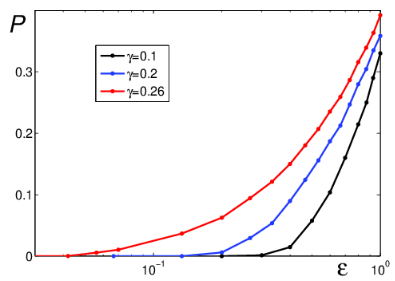

Figure 3.31: Probability of the residence for y-coordinates of random states for the system (3.7) as a function of noise intensity ε.

(x, y)-coordinates for different noise intensities. In the subthreshold regime, one can see a sharp peak above the stable equilibrium M_1. This case describes the SASO mode in the vicinity of M_1. The peak decreases and a ridge arises when the noise intensity ε increases. The ridge expresses the large-amplitude trajectories produced by the influence of stochastic forcing. This ridge increases with noise intensity, and the peak eventually vanishes (Fig. 3.30b). At this point, LASO dominate in the in the regime of mixed-mode fluctuations. This situation may further be described by the probability $P(\varepsilon)$ of residence of y-coordinates in the region $y > -20$ (region of spikes). Fig. 3.31 illustrates the monotonically increasing function $P(\varepsilon)$ for various γ. A sharp ascent of $P(\varepsilon)$ occurs when ε becomes greater than the threshold. Finally, the frequency of random spikes grows with increasing the noise intensity ε, a phenomenon which we now explain.

To this end, let us define the series t_k as the successive times of of random spike times t_k in the model (3.7). A random spike is said to occur when x crosses the threshold $x = 0$. In this case, the random sequence of interspike intervals (ISI) can be defined as $\tau_k = t_k - t_{k-1}$. The intermittency of SASO and LASO modes can be described with the help of mean value of ISI, i.e. $m = \mathrm{E}\tau$. Fig. 3.32 shows $m(\varepsilon)$ for $\gamma = 0.2$, $\gamma = 0.26$ (to the left of the bifurcation point γ_*) and $\gamma = 0.3$, $\gamma = 1$ (to the right of γ_*). For $\gamma = 1$ (the deterministic model having a limit cycle attractor), $m(\varepsilon)$ is almost constant. With no noise ($\varepsilon = 0$), m is the period of the deterministic cycle, and this function grows slightly monotonously as ε increases. For smaller values of γ the function $m(\varepsilon)$ changes regime. Indeed, as we have seen, $m(0)$ (the period of deterministic cycle) increases to infinity as the bifurcation point is approached, and remains infinity for $\gamma < \gamma_*$ (stable attractor). The quantity $m(\varepsilon)$ rapidly decreases and stabilises with increasing ε for γ smaller or near γ_*. As the noise intensity increases, the mean value of ISI becomes almost independent on γ as long as $0.2 < \gamma < 1$. Hence, the presence of noise may be said to cause a structural stabilization of stochastic fluctuations.

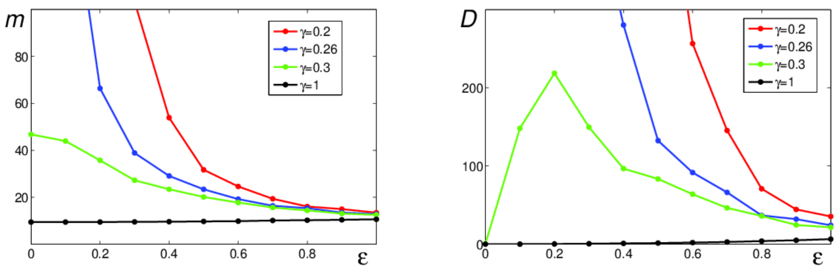

Figure 3.32: The mean value (left) and dispersion (right) of interspike intervals for the stochastic system (3.7) versus the noise intensity ε.

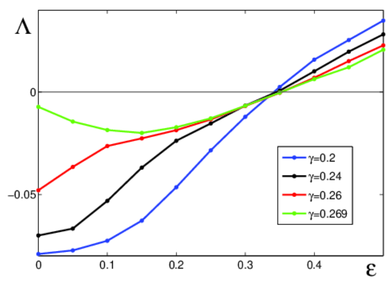

Figure 3.33: The largest Lyapunov exponents for the system (3.7) versus the noise intensity for different γ.

In Fig. 3.33 we show the largest Lyapunov exponent $\Lambda(\varepsilon)$ as a function of the noise intensity. It grows with ε and becomes positive (transition to chaos) for $\varepsilon \approx 0.3$ with increasing ε, and this threshold is almost independent of γ.

3.3 Ice volume – carbon dioxide – ice sheet area model

Paillard and Parrenin [79], hereafter PP, developed another climate model containing the ice volume, the area of the Antarctic continental ice sheet, and the atmospheric concentration of carbon dioxide as the prognostic variables. This section provides a detailed description of it, in absence and presence of stochastic forcing, but neglecting the astronomical forcing. To this end, we introduce three variables x, y, and z denoting the global ice volume (x), the extent of the Antarctic continental ice sheet (y), and the atmospheric concentration in CO_2 (z). The deterministic model takes the form [79]

$$\begin{aligned} \dot{x} &= \tau_V^{-1}\left(-a_1 z - a_2 I_{65} + a_3 - x\right), \\ \dot{y} &= \tau_A^{-1}\left(x - y\right), \\ \dot{z} &= \tau_C^{-1}\left(b_1 I_{65} - b_2 x + b_3 \mathrm{Hev}\left(-F\right) + \delta - z\right), \end{aligned} \tag{3.8}$$

where $\dot{x} = dx/dt$, t is time, $F = ax - by - cI_{60} + d$ expresses the effect of the oceanic switch forced by the salty bottom waters (a, b, c, and d are constant coefficients). Here F increases with the cooling of the Earth's climate (variable x) and decreases with decreasing the continental shelf areas (variable y). What is more, if $F < 0$ the ocean undergoes the interglacial period and vice versa. Parameters I_{60} and I_{65} stand for the daily insolations: I_{60} (60°S, 21st February) and I_{65} (65°N, 21st June). Coefficients τ_V, τ_A, and τ_C represent the time constants, Hev is the Heaviside function, a_1, a_2, a_3, b_1, b_2, b_3, and δ are constants. A nonlinear behavior of system (3.8) arises through the contribution of $\mathrm{Hev}\left(-F\right)$ (the influence of carbon dioxide or interactions between the deep stratification, bottom water formation, and thermohaline circulation [79]).

The model parameters and their ranges suggested by [79] are listed in Table 3.1 (here we consider the case $I_{65} = I_{60} = 0$).

3.3.1 Equilibrium and oscillatory behavior in the deterministic model

Fig. 3.34 shows the bifurcation diagrams versus the parameter δ (it determines the precessional forcing) for the x, y, and z variables, on which one can see a large parametric region of limit cycles. Fig. 3.35 provides an enlargement around $\delta = 0.4$. A subcritical Andronov-Hopf bifurcation occurs

Table 3.1: Model parameters and their ranges [79].

Parameter	Value	Range
τ_V	15 kyr	13.11-18.1
τ_C	5 kyr	3.1-15
τ_A	12 kyr	9.5-26
a_1	1.3	1.23-1.44
a_2	0.5	0.4-0.64
a_3	0.8	0.77-0.82
b_1	0.15	0-0.35
b_2	0.5	0.46-0.54
b_3	0.5	0.37-0.6
δ	0.4	0.39-0.42
a	0.3	0.26-0.39
b	0.7	0.63-0.74
c	0.01	0-0.15
d	0.27	0.253-0.302

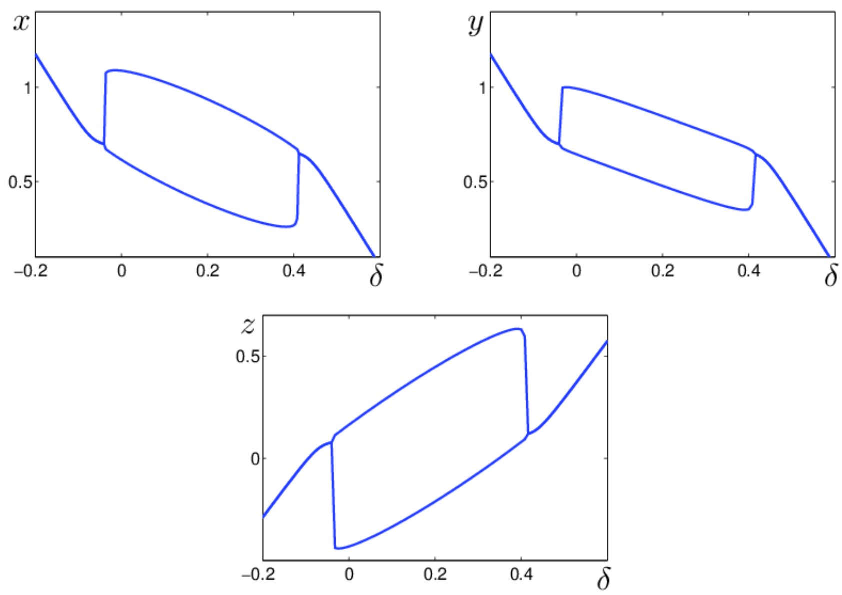

Figure 3.34: Bifurcation diagram: extremum values of x, y, and z coordinates for attractors of system (3.8).

at $\delta_1 = 0.4047$, where the equilibrium $(\bar{x}, \bar{y}, \bar{z})$ loses stability. The value $\delta_2 = 0.4088$ marks a saddle-node bifurcation of cycles. Between (δ_1, δ_2), the stable equilibrium co-exists with a limit cycle.

Fig. 3.36 depicts phase portraits for three values of parameter δ lying in the range of possible variations pointed out in Table 3.1. For $\delta = 0.4$ (Fig. 3.36a), the limit cycle (red curve) is the only attractor. The model therefore exhibits large-amplitude self-oscillations. At $\delta = 0.407$, the system is, as we have seen, bi-stable. Phase trajectories tend either to the stable equilibrium (black circle) or to the limit cycle (red curve) depending on the initial condition (see Fig. 3.36b). For $\delta = 0.41$, the system possesses has only one stable equilibrium point. In this regime, the path from the initial value to the attractor may either be direct if the initial point is close to the attractor, or follow a large-amplitude loop if it comes from further away. Here again we observe the phenomena associated with the existence of a sub-threshold and a superthreshold zone. These peculiarities of the deterministic phase portraits are important in understanding the stochastic phenomena taking into account the random disturbances.

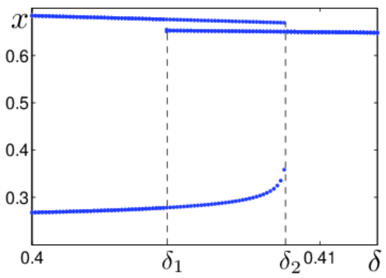

Figure 3.35: Bistability zone.

3.3.2 Analysis of the noise-induced mixed-mode oscillations

To study the stochastic phenomena in the Paillard-Parrenin model, we consider the following system with stochastic forcing

$$\begin{aligned} \dot{x} &= \frac{1}{\tau_V}(-a_1 z - a_2 I_{65} + a_3 - x), \\ \dot{y} &= \frac{1}{\tau_A}(x - y), \\ \dot{z} &= \frac{1}{\tau_C}(b_1 I_{65} - b_2 x + b_3 \text{Hev}(-ax + by + cI_{60} - d) + \delta - z + \varepsilon\xi(t)). \end{aligned} \tag{3.9}$$

Here, $\xi(t)$ is a standard Gaussian white noise with parameters $\langle \xi(t) \rangle = 0$ and $\langle \xi(t)\xi(\tau) \rangle = \delta(t - \tau)$, and ε stands for the noise intensity. Physically it means that we study the effect of additive stochastic forcing in the rate of carbon dioxide variations. In the present analysis, the numerical simulations of random solutions of the stochastic system (3.9) were carried out on the basis of the Euler-Maruyama scheme with the time step 10^{-4}.

We start from the case where the stable equilibrium $(\bar{x}, \bar{y}, \bar{z})$ is a single attractor, near the bifurcation value $\delta_2 = 0.4088$. With weak noise, the system

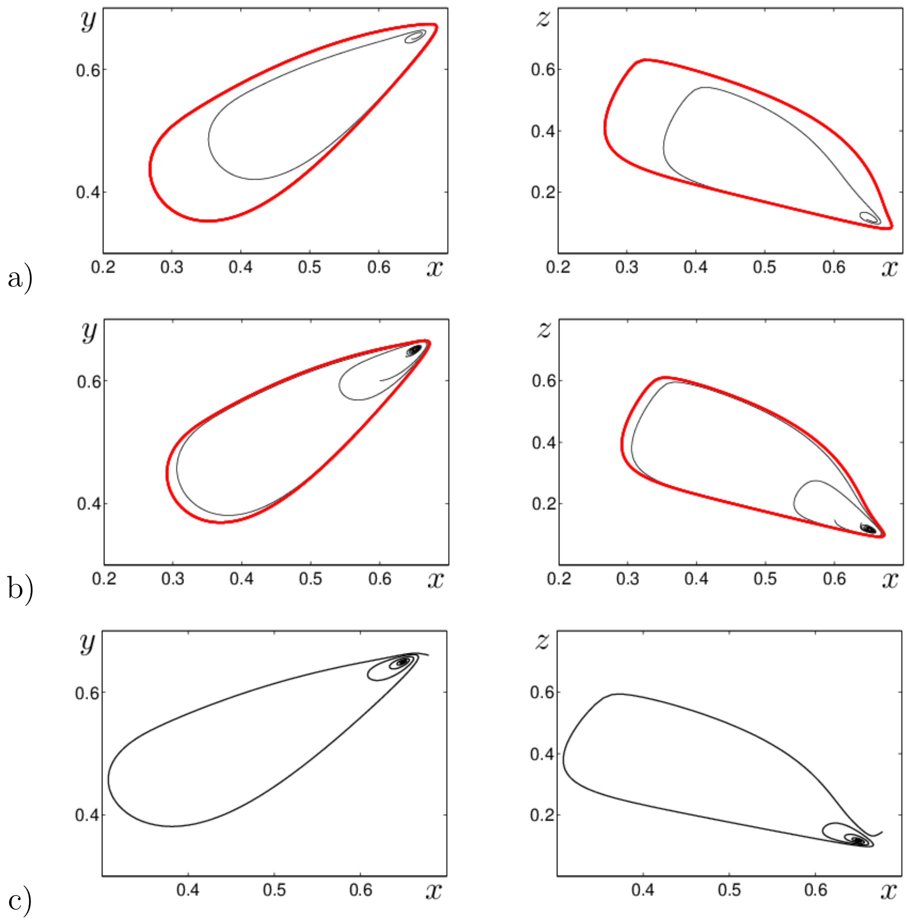

Figure 3.36: Phase portraits of the deterministic system (3.8) for a) $\delta = 0.4$, b) $\delta = 0.407$, and c) $\delta = 0.41$.

(3.9) exhibits the small-amplitude oscillations near its equilibrium. The dispersion of these oscillations increases as the noise intensity increases. A sharp change in the dispersion occurs when stochastic trajectories are strong enough to reach the superthreshold zone. This qualitative change of the dynamics is illustrated in Fig. 3.37 for $\delta = 0.41$ (compare blue trajectories, for $\varepsilon = 0.01$, and green trajectories, for $\varepsilon = 0.05$, of which the behaviour is typical of mixed-mode dynamics. As can be seen from the time series shown in Fig. 3.37, the presence of noise causes a sharp spike-type decrease in the global (x) and Antarctic (y) ice while the atmospheric carbon dioxide (z) sharply grows.

Some details of the transformation from small- to large-amplitude oscillations are shown in Fig. 3.38 for $\delta = 0.41$ and in Fig. 3.39 for $\delta = 0.43$. Here, x, y and z-coordinates of the random solutions versus noise intensity ε are plotted. As one can see, the intensity of noise corresponding to the onset of large-amplitude stochastic oscillations depends on the parameter δ: the more δ, the larger noise is necessary for the generation of large-amplitude oscillations. A quantitative description of the changes in probabilistic distributions is given

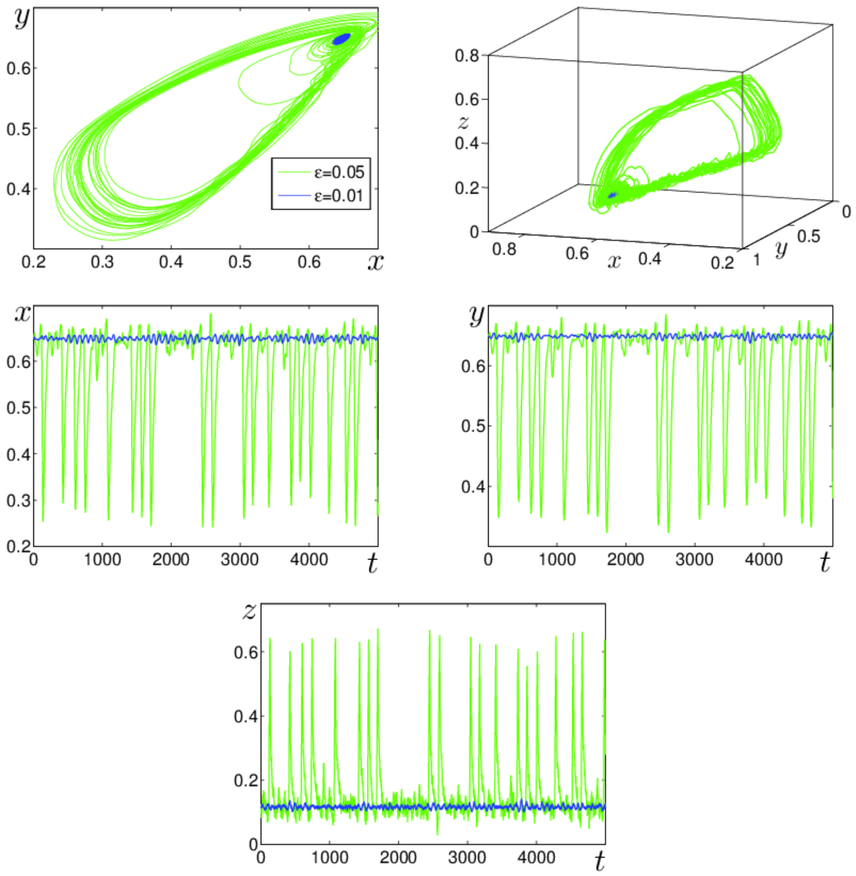

Figure 3.37: Stochastic excitability. WE NEED TIME UNITS TO SEE WHETHER THIS IS REALISTIC OR NOT. THIS LEGEND MUST BE EXPANDED. THESE MUST BE THOUSAND OF YERAS ?

in Fig. 3.40. Here, we show how the mean value $m = \langle x \rangle$ of random states and their mean square deviations $D = \langle (x - \bar{x})^2 \rangle$ from the equilibrium depend on parameters δ and ε. An important point is that there are the parametric zones where some abrupt changes in m and D occur. These zones mark the onset of stochastic generation of the mixed-mode oscillations in the Paillard-Parrenin model.

Results of the mathematical and numerical analyses presented above allow us to conclude that in some cases, the deterministic model does not give an adequate description of climate dynamics. Here, it is highly important to take into account the presence of the inevitable random noise. In the model under consideration, even a small background noise transforms the system dynamics from the equilibrium to the mixed-mode large-amplitude oscillations.

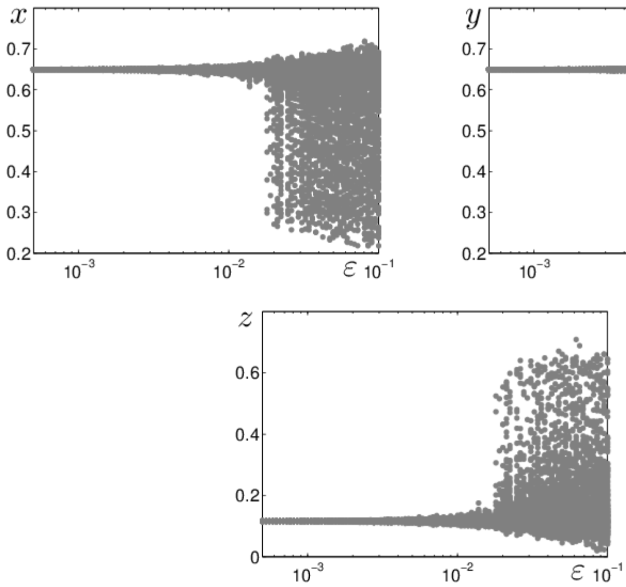

Figure 3.38: Random states of the stochastic system (3.9) for $\delta = 0.41$ versus noise intensity.

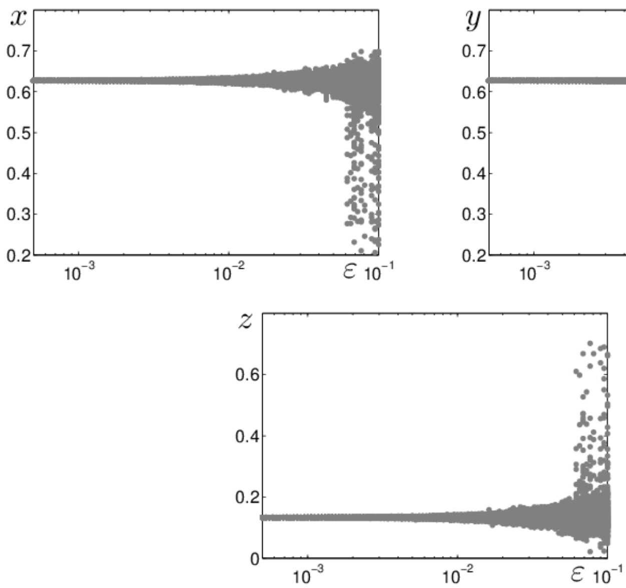

Figure 3.39: Random states of the stochastic system (3.9) for $\delta = 0.43$ versus noise intensity.

3.4 Some important peculiarities of 3D noise-induced dynamics

Our analysis of different stochastically-induced three-dimensional climate models that contain various prognostic variables and coefficients lead us to the following partial conclusions:

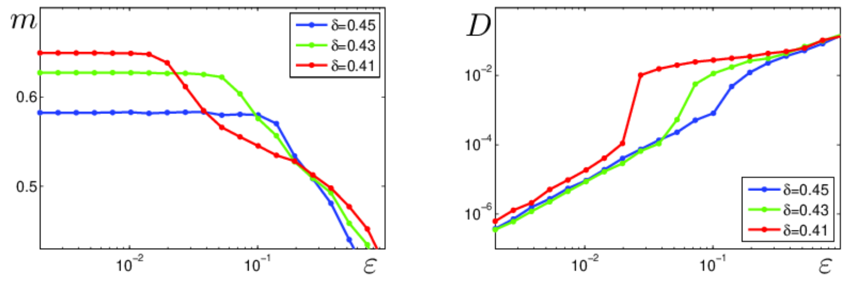

Figure 3.40: Mean values m and mean square deviations D for solutions of system (3.9).

i) The deterministic system may contain two stable equilibria and a limit cycle (their arrangement and bifurcation diagram essentially depends on variations of system parameters). In most paleoclimate models, these equilibrium phase points describe warm and cold phases of the Earth's climate. Large excursions from these extreme phases may be excited by noise.

ii) As the parameters approach a bifurcation point associated with the creation of a limit cycle, small amount of noises become more likely to trigger both small- and large-amplitude stochastic oscillations (SASO and LASO). In this scenario, the LASO corresponds to the excitation of the limit cycle. LASO may also be found in situations where a several fixed-points coexist, or where a fixed-point coexists with a limit cycle, or, yet, when there is a single fixed point attractor. In all theses scenarios, triggering a LASO depends both on the amplitude of stochastic oscillations, but also of the direction of this perturbation. Therefore, for certain amplitudes, the excitation of LASO may only be intermittent, and coexist with frequent SASO oscillations. This regime is characteristic of mixed-mode oscillations.

iii) The analysis of Lyapunov exponents carried out in this section statistically confirms that the system may undergo a transition from order to chaos due to the effect of noise-induced intermittency of LASO and SASO modes. In other words, large amplitude stochastic oscillations may sharply increase the dependence of system's trajectories to initial conditions.

iv) Physically, the glaciation/deglaciation periods (100 ky saw-tooth type climate fluctuations) become shorter, easier and faster with increasing the noise intensity. An important outcome is that a transition between the warm and cold climate states suddenly occurs when the climate system approaches the parametric vicinity of its bifurcation point. In this case a potential possibility to an abrupt glaciation/deglaciation transition becomes greater with the growth of stochastic forcing (this conclusion follows, for example, from the analysis of interspike intervals).

Chapter 4

Effects of the orbital forcing

4.1 Origin and computation of the astronomical (orbital) forcing

So far we have considered models which represent causal relationships between components of the climate system. We have been able to understand how non-linear interactions, along with stochastic effects, provide a formal basis to explain how climatic cycles, punctuated by intermittent behaviour, may emerge in a constant environment.

We have voluntarily discarded the effect of external causes to the succession of ice ages. Yet, such causes exist, and are even often considered as the most important driver of glacial-interglacial cycles. It is therefore time to address them.

Herschell [80] is quoted as having first formulated the hypothesis that "astronomical causes" may influence "geological phenomena". He pointed out that because of the precession of the equinoxes, the Earth, at one point of the year, may be either closer or further away to the Sun, which may "produce a transition for one to the other species of climate". Milankovitch [23] is best known today for having provided theoretical foundations of such "astronomical theory of palaeoclimates". He connected the then state-of-the-art knowledge of celestial mechanics, with a treatment of the energy budget of Earth radiation across latitudes, accounting for the modulation of Earth's albedo by snow cover. Further historical context on the development of astronomical theories is available in [81] and [82].

Before discussing the mechanisms of insolation forcing on climate, we review briefly the basic elements which determine insolation changes. The semi-major axis of Earth's orbit does not change appreciably over ice ages [83, 84]. Because of this, the distribution of insolation over latitudes and seasons is fully determined by three parameters [85]: Earth's eccentricity e, measuring the deviation of the eccentric orbit from circularity, obliquity ε, which is the angle between the equator and the ecliptic, and the longitude of the perihelion, ϖ that is, the angle measured between the perihelion and the vernal point. The literature is sometimes confusing about the choice of heliocentric or geocentric coordinates to measure ϖ, causing a shift of π in the definition of ϖ, but this is not a point we will further address here. The dynamics of e are immediately related to the dynamics of the planetary system were first solved by a perturbation method due to Lagrange. Nowadays, the combination of accurate observations, fast computing, and advanced symplectic integration schemes allow for accurate computation of orbital elements over several tens of millions of years in the past and in the future [86]. However, solutions obtained by perturbation method are still used in models of climate dynamics because they present a nice advantage. Even though these solutions are nowadays less accurate than state-of-the-art symplectic integration, the perturbation method presents an advantage. It works by identifying resonance terms, so that the angles which define the orbit are, in the end, expressed as a sum of harmonics. For computing ε and ϖ one needs, in addition, to take care of the lunisolar precession caused by Earth-Sun-Moon dynamics, which can also be solved by a method of perturbations. Together, these elements provide the basis to obtain, with a very good approximation, an expression of the astronomical forcing as a sum of sines and cosines [85]:

- obliquity (ω) dynamics is dominated by periods around 40 ka and 54 ka.
- climatic precession, defined as $e \sin \varpi$ has periods around 19 and 23 ka.
- eccentricity e has periods around 404, 95, 124, 99 and 131 ka.

The effect of the variations of the different orbital parameters on insolation at the top of the atmosphere are determined by geometry, and were largely established in [23]. *Obliquity* controls the distribution of annual mean insolation across latitudes: High latitudes get more radiation when obliquity is high, at the expense of the equator, the pivot being located at 43°. A higher obliquity also causes a stronger seasonal contrast. The *climatic precession* controls the amount of radiation received by the whole planet at a given month of the year.

Glaciologists interested in ice age dynamics have adopted since the 1980s a dynamical system framework to model the effect of insolation on ice ages [87,88].

At time of writing the most recent example of deterministic dynamical system model along this line is provided by [77], and which we comment later on in this chapter.

Insolation is distributed across latitudes and seasons, and a change in astronomical forcing generally affects the amount of insolation received at any time in the year and at any latitude, except, of course, during the polar night.

One problem is therefore to estimate the integrated effects of a change in distribution on the mass balance of ice sheets.

Milankovitch considered that the radiation received over summer in high northern latitudes determines the extent of glaciers. Hence, in Milankovitch's theory, ice sheets tend melt when obliquity is large, and when perihelion is reached when it is summer in the northern hemisphere.

This assumption is still considered to be valid nowadays. One the one hand, it is consistent with observations: it has now long been established that sea level tends to rise, i.e., ice sheets melt, when summer insolation increases [89]. On the other hand, it is consistent with computations with numerical simulators, which integrate equations of motion of the atmosphere, ocean and ice flows over a grid [25, 90].

Hence, in a low-order dynamical system model of ice ages — which is the approach we are interested in for the present review — the effect of astronomical forcing on ice sheet mass balance may be adequately parameterised using summer insolation, and not globally averaged insolation. This is important, because the summer insolation is largely dependent on precession and obliquity, while globally averaged insolation is only but slightly affected by eccentricity.

Yet, there are different approaches to parameterise summer insolation. It is common to use insolation received at 65°N on the day of summer solstice [42, 91], or in July [92]. These metrics differ from the original parameterization of [93], which integrated insolation over the half-year receiving the largest amount of insolation. Huybers and Tziperman [94] advocated using a metric more similar to the original Milankovitch one, which they argued is more consistent with our knowledge of ice sheet mass balance. Statistical inference gives them a further argument: a metric which gives more weight to obliquity, as does summer-integrated insolation compared to mid-June insolation, is more consistent with the benthic-foraminifera record [95, p.14].

4.2 The strong interpretation of the Milankovitch theory

Milankovitch's original view was that ice ages are caused by the astronomical forcing. They would not occur if orbital elements and obliquity were constant. We will refer to this view as the "strong interpretation" of Milankovitch's theory.

Letting aside, for a moment, what we can infer from our knowledge of ice sheet physics and other elements of the climate system, what is a priori the simplest dynamical system which would remain at rest in absence of forcing,

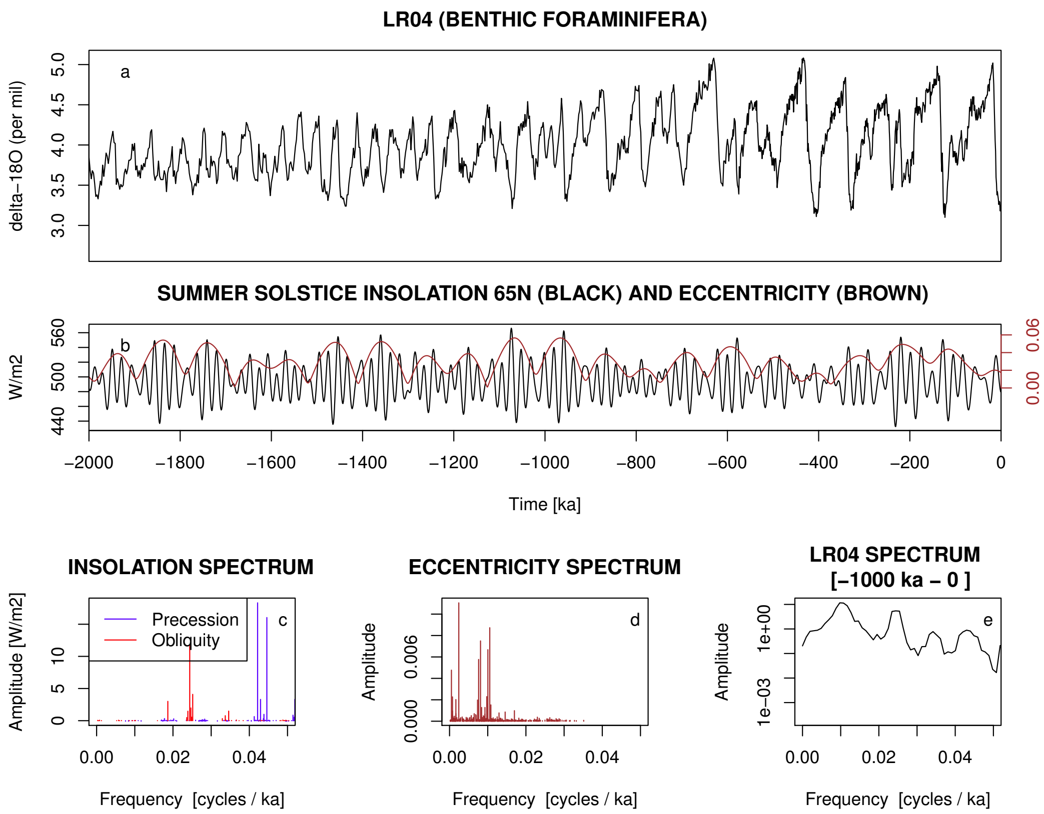

Figure 4.1: (a) Reconstructed climate variations over the last 2 million years (1˜ka stands for 1,000 years) inferred from deep-sea organisms, specifically benthic foraminifera [10], along with (b) the variations in incoming solar radiation at the summer solstice at 65° N (black), a classical measure of astronomical forcing computed here following the BER90 algorithm [96]. The spectrum of insolation is (c), with components arising from climatic precession and obliquity computed following [85, 97]. Eccentricity (figure (b), brown) is the modulating envelope of precession, and its spectrum is given in (e) [85, 97]. (f) multi-taper estimate of the LR04 spectrum (last million years only) estimated using multi-taper method [98] obtained using the SSA-MTM toolkit [99] with default parameters. Figure from [100].

and display oscillations with forcing, is a forced, linear relaxation:

$$\frac{\mathrm{d}x}{\mathrm{d}t} = -\frac{1}{\tau}(x - F(t)), \tag{4.1}$$

where τ is a relaxation time, and $F(t)$ is the insolation forcing. If $F(t)$ is a sum of harmonics, with frequencies ν_i, then the $x(t)$ obtained with a deterministic model 4.1 is a sum of harmonics with the same frequencies ν_i. However, palaeoclimate reconstructions of the latest four ice ages show that they followed a cycle of approximately of 100 ka, and their temporal structure presents a distinctive saw-tooth shape, with glacial build-up slower than deglaciation — a fact known since the pioneering Broecker and van Donck [9]. Neither the 100 ka period, nor the saw-tooth shape, appear in the forcing. This rules out the deterministic linear relaxation model.

Yet, it has generally been recognised that a linear relaxation model may still provide a good starting point because the variation rate of ice volume during the phase of ice accumulation clearly respond to insolation. More precisely, they appear to broadly follow changes in summer insolation [9, 89]. Consistent with this observation, the power spectrum of climate records contains the frequencies of obliquity and precession [101–103]. Hence, several authors suggested that the climate dynamics deviate substantially from a linear response regime only during the episodes of deglaciation, that is, when the ice volume decreases rapidly towards interglacial conditions. For example, MacAyael [104] expressed this suggestion to use a topological model inspired from imagery provided by the catastrophe theory of Ren Thom: the deglaciation would be the manifestation of a fold catastrophe (Fig. 4.2, left). Paillard [91] (hereafter P98) encoded a similar idea into a hybrid dynamical system (Fig. 4.2, right). A hybrid dynamical system model combines a continuous variable (in this case: a level of deglaciation, called v), with a discrete state that is, again in this particular case, one of i (interglacial), g (semi-glaciated), and G (heavy glaciation). The rules of transitions across discrete states are determined by rules of threshold crossing by v, and by the astronomical forcing function F. Within a same regime, that is, as long as the discrete state remains unchanged, the variable v follows linear relaxation dynamics. However, both the relaxation target and relaxation time depend on the discrete state. Therefore, when the discrete state changes, the variation rate of v changes discontinuously. The topology of system trajectories are constrained by rules establishing which transitions may take place. Only three transitions are allowed: $i \to g$, $g \to G$, and $G \to i$. The transition $g \to i$ is forbidden. Furthermore, the transition $G \to i$ is assumed to occur when the *forcing function* — insolation — exceeds a threshold. These rules impose asymmetric ice age cycles, with deglaciation occurring when insolation is high enough, consistently with the observation record.

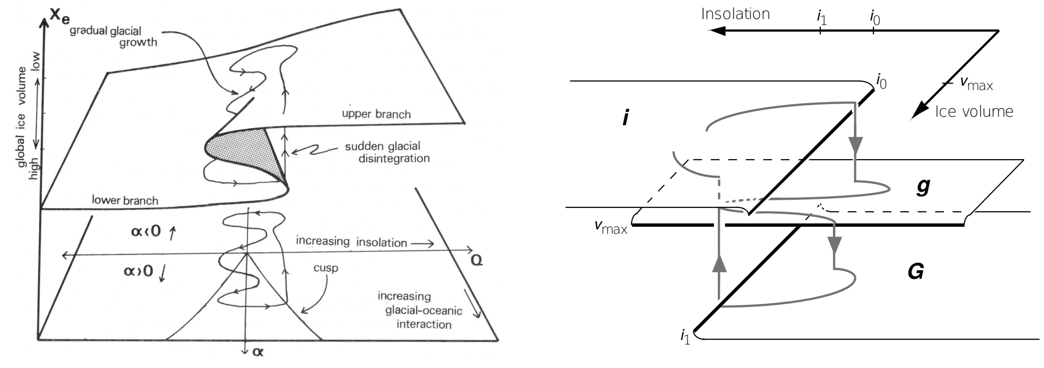

Figure 4.2: Two historical, conceptual models formulating the hypothesis that ice ages are the manifestation of astronomically-forced ice build-up, terminated by a catastrophic deglaciation. MacAyael 1979 (left-hand side) is directly inspired by catastrophe theory and glaciological theory. Q is insolation, and α a *potential action* increasing throughout the ice acclimation phase. In Paillard (1998) (right-hand-side), the role of α is played by a discrete state, with transitions from i, g and G determined by thresholds defined in the plane defined by ice volume and insolation. In both models, the fully glaciated state is intrinsically unstable, prone to collapsing

With these constraints, P98 provides a simple and easily understandable mechanism explaining how the period of ice age cycles may double the period of the forcing. Assume a harmonic forcing, of fixed amplitude. Starting from an interglacial state i, a first forcing minimum — assuming it is large enough — can force a transition from state i to g, where it is protected against the following maximum phase of the forcing (because $g \to i$ it is forbidden, see again Fig. 4.2). The second forcing minimum causes the system to switch from g to G. G is postulated to be more fragile. At this point, the next insolation maximum will generally suffice to precipitate the system into i, the interglacial state. Hence, even though the ice age sequence is determined by the forcing, the ice age duration may be a multiple of the forcing period. If, for example, we assume that the forcing is caused by obliquity (40 ka), then the ice-age cycle duration happens to be 80 ka. With the more complicated forcing function obtained from the addition of the numerous harmonics, the model generates non-periodic ice age cycles, which have roughly the allure of the Late Pleistocene ice age cycles. The model satisfies the strong interpretation of the Milankovitch theory, because in absence of forcing, the system lands on a fixed point, and also accounts for the asymmetric shape and duration of glacial-interglacial cycles.

Ditlevsen, 2009 [105] (hereafter, D09) re-expressed the ideas underlying P98 model in the form of a continuous dynamical system. The discrete regimes of the P98 model appear in the form of attracting stable states, which fold bifurcations arranged such that the trajectories generated by D09 reproduce qualitatively the regime changes encoded in P98. This reformulation has allowed this author to study the possibility of "noise assisted transitions" from one branch to the next, making the model more sensitive to stochastic forcing than P98. We will, however, not consider this model further here.

Both P08 and D09 provide an idealized realization of the strong interpretation of Milankovitch's theory (no ice ages without astronomical forcing), and both suggest that long glacial cycles can be interpreted as a form of period-doubling mechanism: the ice-age build-up phase survives one or two insolation maxima before entering a regime more unstable, and vulnerable to the subsequent insolation maximum. A qualitatively similar behaviour may be obtained with other standard dynamical systems, such as the Duffing oscillator [106]. The period-doubling concept provides a plausible explanation to the so-called Mid-Pleistocene transition, about 1 Ma ago, when the period of ice ages shifted from 40 ka, to about 100 ka. It suffices to assume that before the Mid-Pleistocene transition the ice sheets were vulnerable enough to be hit by the first insolation maximum, which occur approximately every 40 ka [107]. The transition is the manifestation of an increased resilience of this mid-glaciated state. It is often suggested that this increased resilience is related to a decrease in the background levels of CO_2 concentration, but this is not entirely sure. Interglacial temperatures in the southern ocean seemed to have remained stable since at least 1.5 Ma [8], which suggests that the interglacial-level of CO_2 concentration has remained reasonably constant as well.

This hypothesis encoded in P98 is very schematic but reasonably compatible with what glaciologists have known about ice sheet dynamics since the 1960s. Thick ice sheets cause significant strong lithospheric depletion (about a third of the ice-sheet thickness is below the unperturbed bedrock level). Warming may cause enhanced ablation on the southern edge of the ice sheet, which, given the lithospheric depression, may strongly enhance the southward flow of ice, causing the ice sheet to lose altitude. With this mechanism, an increasing fraction of its surface may end up below the equilibrium snow line, at which point its melting becomes ineluctable. These basic elements were captured in reasonably simple models about thirty years ago [22]. Other mechanisms may contribute to destabilising the ice sheet. Ocean warming and sea-level increase may conspire to break ice shelves, and as ice shelves somehow consolidate the ice sheets via an effect called ice buttressing, their loss may further therefore contribute to destabilising of the ice sheets and enhance the deglaciation [108].

Before the possibilities offered by supercomputers, the understanding of ice sheet dynamics was based on scaling relationships linking ice sheet thickness, extent, and ice flow, incorporated in conservation equations (e.g. [24,109,110])).

This modelling approach remains, we argue, insightful because it allows us to link basic properties associating with scaling and conservation laws, with what observations about palaeoclimates. The VCV18 model [77] is a contribution in that direction. This is a system of three ordinary differential equations expressing the dynamics of ice area S, temperature at the base of the ice sheet θ, and a global climate state ω. The climate feedbacks which are not immediately related to the large-scale ice flow (e.g., CO_2 response) are parameterised as a linear feedback. This model appears to support some of the intuitions explicitly encoded in P98. In absence of astronomical forcing, VCV18 presents one fixed point. Furthermore, with adequate, and physically reasonable parameter values, the model features a period-doubling mechanism similar to the one outlined about P98: Starting from an interglacial, ice build-up is accelerated by two positive feedbacks, one caused by the increase in areal extent of the ice sheets, the other one related to the global climate cooling. These positive feedbacks are, however, compensated for by basal-sliding, itself proportional to basal temperature. The resultant of these feedbacks concur to produce a stable, mid-glaciated state, which resists the following insolation maximum. The following insolation *minimum* generates another thrust towards a higher glaciation level. It this point, basal sliding grows non-linearly. A subsequent insolation maximum produces a catastrophic meltdown that brings the system back to its interglacial level.

The literature reporting simulations with models using finite difference schemes for resolving the equations of ice sheet flow dynamics is fairly abundant and cannot be fully reviewed here. Over the years, it has become common to couple these ice sheet models with atmosphere-ocean models of increasing level of detail and complexity, see, for example, the progression visible from [25, 90, 111, 112]. The course of CO_2 concentration is difficult to simulate and is often prescribed as a forcing. However, Ganopolski and Brovkin [113] provide an example linking reasonably detailed ice sheet dynamics with carbon cycle dynamics. The simulations made with these models are generally presented as a support compatible with the strong interpretation of Milankovitch's theory, and with the notion that CO_2 changes constitute a feedback to ice-sheet variations, essential to explain the amplitude of sea-level variations.

4.3 The weak interpretation of the Milankovitch theory

As we have just seen, more detailed models resolving the ice sheet dynamics tend to support the strong interpretation of the Milankovitch forcing. We will now consider the possibility that an autonomous oscillation between glacial and interglacial cycles remains a plausible possibility. To make this argument, we focus again our attention on CO_2.

One of the best known and quantified mechanisms by which glaciations affect CO_2 is the effect of a decrease in sea-surface temperature on the solubility of CO_2 in seawater. However, this mechanism would only explain 25 ppmv change between the last glacial maximum and the Holocene [114, 115], out of the 80 to 100 ppm which characterise glacial-interglacial cycles. Among other mechanisms, changes in ocean circulation — which may be rapid — may have contributed substantially to CO_2 concentration changes, but the amplitude and dynamics of this contribution is more uncertain. Ocean circulation changes may further impact the distribution of alkalinity in the deep ocean and affect CO_2 concentration via the growth or dissolution of biogenic calcite. Changes in sea levels also affect the riverine input of calcite and further affect the chemical balance and the pH of the ocean [114]. Photosynthesis, in the ocean, may respond to changes in micronutrient input by dust, especially iron. Finally, CO_2 outgassing, especially around oceanic ridges, may be affected by changes in hydrostatic pressures caused by the variations in sea level, and contribute to glacial-interglacial CO_2 variations [103].

The possibility that one or several of these mechanisms may contribute to generating limit cycle dynamics is in part suggested by inspection of the ice core records. For example, all interglacials of the last 800 ka — with the notable exception of the Holocene — have a concentration of CO_2 peaking just after the deglaciation, and decreasing afterwards [116]. This decrease may contribute to preparing the conditions for a subsequent glacial inception. Over the two latest deglaciations, CO_2 was observed to increase gently — though modestly — *before* any substantial increase in sea level [117].

Taken together, we see the possibility — but not the certitude — that ice sheet dynamics and carbon cycle dynamics interact in a way that gives rise to an autonomous limit cycle — an oscillation between glacial and interglacial cycles. Modelling the dynamics of the carbon cycle turns is arguably a more challenging and speculative exercise than modelling ice sheet dynamics, because the mechanisms which may substantially affect CO_2 concentration are diverse and difficult to quantify. The modeller cannot use scaling and conservation laws in the same way as with ice sheet dynamics. Hence, a variety of low-order models have been designed to present various mechanisms as a possible cause of autonomous limit-cycle dynamics. For example, Paillard and Parrenin [79] focus on southern ocean circulation and ventilation, Omta et al. [118] on the alkalinity balance [118], and Huybers and Langmuir [103], on mid-ocean ridge outgassing.

Milankovitch did not consider the possibility that glacial-interglacial cycles could be an autonomous oscillation, but one might still speak of a 'weak in-

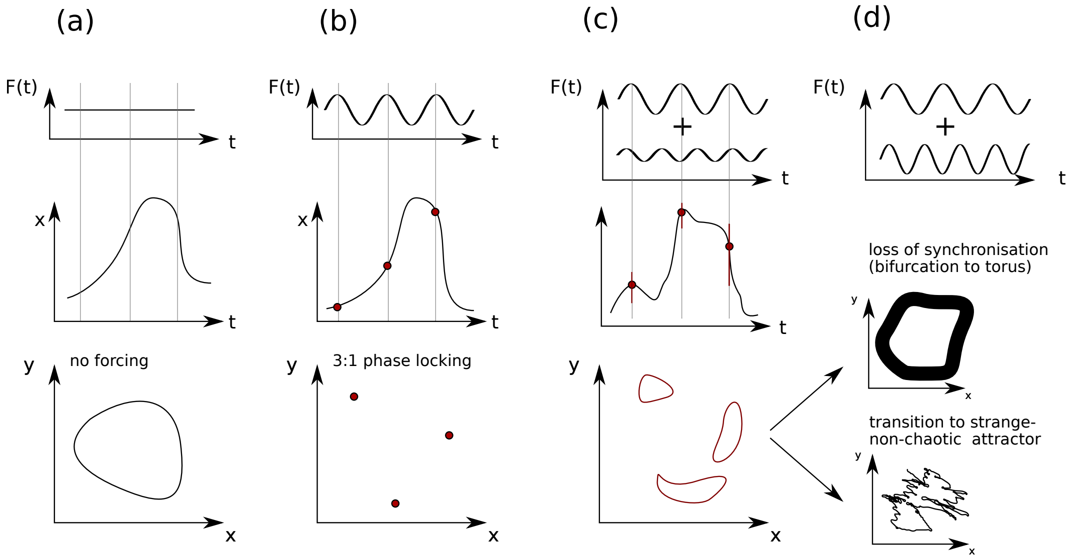

Figure 4.3: Schematic time series and phase diagrams of an oscillator forced by periodic and quasi-periodic forcings. (a) describes a periodic forcing (top) of a system with state space (x, y). It is assumed that the system response is here synchronised on the forcing with a $3:1$ ratio. The stroboscopic view, taken every forcing period, comprises three points. (b) represents the same system, but with an additional weak periodic forcing, with a period incommensurate to the main forcing component. Synchronization is maintained, so that the stroboscopic view present three closed loops homeomorphic to circles (the attractor is a torus in the forcing-state space). Further increasing the amplitude of the second harmonic forcing may either cause a synchronization loss, or a bifurcation towards a strange-non-chaotic attractor.

terpretation' of Milankovitch's theory if we consider the hypothesis that astronomical forcing sets the timing of the glacial-interglacial transition. In mathematical terms, this hypothesis can be expressed by the claim that glacial-interglacial cycles constitute a limit cycle *synchronised* on the astronomical forcing. However, to give substance to this claim we need to specify what is meant by synchronization. This is what we do now (the reader is referred to [119] for a reference text on synchronization).

Synchronization is easiest to describe and define when the forcing is period. Consider, specificity, a periodic forcing of amplitude A and period P.

The system is autonomous when $A = 0$. Suppose the system is observed every time $= n \times P$, to construct a stroboscopic view (Figure 4.3 (a), bottom). As there is no forcing, the phase of the limit cycle is unrelated to the phase of the forcing, and from repeated observations at different times $n \times P$ one will generally recover the topology of the autonomous attractor, in this case, a loop homeomorphic to the circle. Consider a weak positive A. In general, the stroboscopic view will be affected by the forcing, but remain homeomorphic to

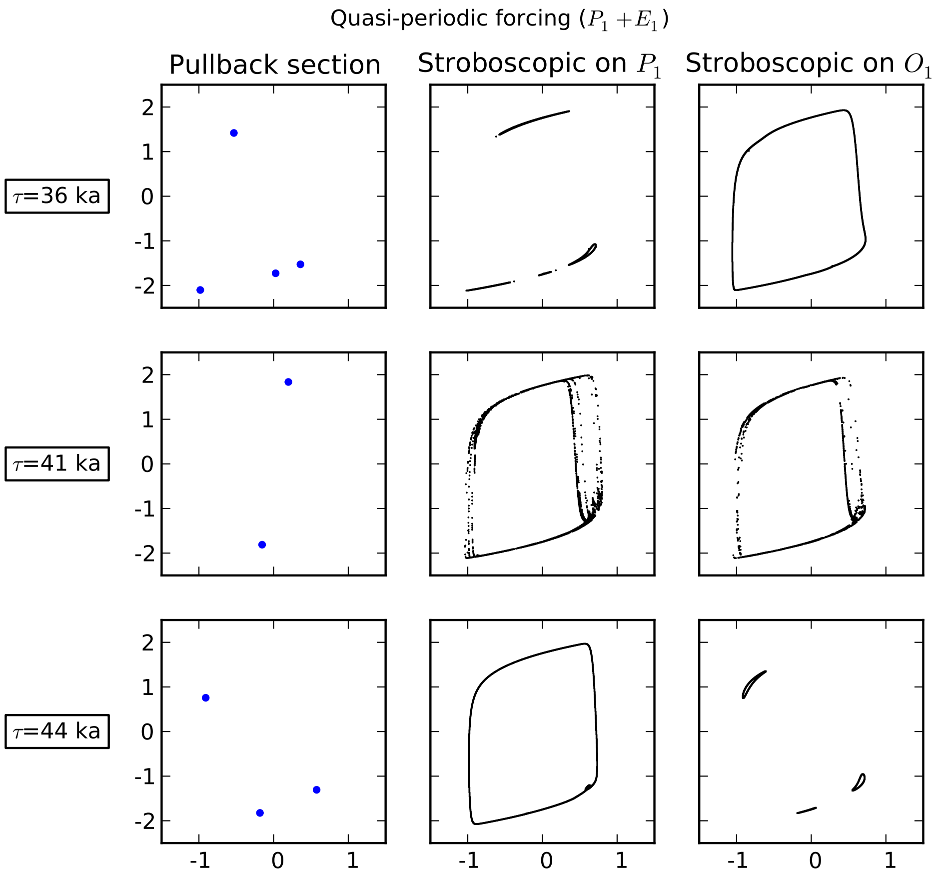

Figure 4.4: These figures were obtained with a conceptual oscillator model similar to a van der Pol model (see details in [120]), forced by a two periodic forcings: one with period 41 ka (this period is referred to as O1, for obliquity) and one of 23 ka (referred to as P1, for precession). The three rows, denoted $\tau = 36$ ka, 41 ka, and 44 ka, correspond to values in one of the model parameters, which controls the period of the autonomous oscillation. The left-hand-side column shows a "pullback section". The middle- and right-hand-side columns are stroboscopic views, that is, figures obtained by superimposition of states found at $t_0 + kP$, where P is either the period P_1 or O_1. See text for further explanation and interpretation . Figure redrawn from [120].

the circle. *Phase locking* is said to occur when this stroboscopic view changes from a loop to a set of points. This situation is depicted on Fig. 4.3(b). The underlying intuition is that the phase of the forcing controls the phase of the system cycle. Phase locking is a form of synchronization.

Consider now that a second forcing component is introduced, but with an amplitude significantly weaker than the main component. This case is illustrated on Fig. 4.3(c). The influence of this second harmonic will manifest itself by disturbing the state of the system. The time series $x(t)$ and $y(t)$ are no-longer periodic, but the system phase is still constrained by the dominant forcing. The stroboscopic view (bottom) then shows three closed curves, confirming that phase-locking is maintained. This is the signature of a quasi-periodic attractor, which combines the synchronised period (in this example, three times the period of the main forcing component), with the period of the secondary forcing component.

We can now foresee that as the amplitude of the second harmonic is further increased, the closed curves will connect, causing a bifurcation. At this point, two scenarios are generally observed. The first possibility is a torus bifurcation causing a loss of synchronization. The time series on both sides of the bifurcation are quasi-periodic (a sum of periodic signals), but in the synchronised regime, the time series are the sum of two periods, as we have just seen. When synchronization is lost, the time series are the sum of three periodic components (associated with the two forcings, plus the intrinsic period of the system). The second possibility is a bifurcation towards a strange non-chaotic attractor. In this case the time series become aperiodic, but, as we will see shortly, it is a synchronization regime.

To see this, we consider the following continuous oscillator, almost identical to the van der Pol oscillator. This was an attractive model to use because, on the one hand, literature is available about the quasi-periodic forced van der Pol oscillator, analysing the torus bifurcation [121] and the transition to strange-non-chaotic attractor [122]. With an additional drift term β which we introduced below, the forced van der Pol can be calibrated such as to reproduce glacial-interglacial cycles fairly convincingly [120], making it a credible model for our purpose. The model is defined as follows:

$$\begin{cases} \dfrac{\mathrm{d}x}{\mathrm{d}t} = (-y + \beta + F(t))/\tau \\ \dfrac{\mathrm{d}y}{\mathrm{d}t} = -\alpha(y^3/3 - y - x)/\tau \end{cases}$$

We adopt $F(t) = \gamma[\sin(2\pi/P_1 t + \phi_{P1})) + \cos(2\pi/O_1 t + \phi_{O1})]$, with $P_1 = 23.716$ ka, $O_1 = 41.000$ ka and $\phi_{P1} = 32.01^\circ$ and $\phi_{O1} = 251.09^\circ$. P_1 is the first period in the development of precession, O_1 is the first period in the development of obliquity and ϕ_{P1},ϕ_{O1} the corresponding phases given by [85], so that $F(t)$ may already be viewed as a very rough representation of the astronomical forcing. The forcing amplitude $\gamma = 0.6$, $\alpha = 30$, and $\beta = 0.7$.

Stroboscopic views for different values of τ are shown on Figure 4.4. On the middle column, the stroboscopic view is taken with respect to P_1; on the right-hand-side column, with respect to O_1. Contrary to Figure 4.3, the forcing amplitudes are constant, but the parameter τ varies. One therefore recognises three regimes: phase-locking on P_1 (obtained with $\tau = 36$ ka), phase-locking on O_1 (with $\tau = 44$ ka, third row), and strange-non-chaotic regime (with $\tau = 41$ ka, middle-row). The qualifier "strange" refers to the topology of the attractors and repellers. In the quasi-periodic regime, the attractor and repellers are well separated. In the strange regime, the repeller is embedded in the attractor in a way that both may be arbitrarily close to each other. This proximity of attractors and repellers implies that the strange regime is more sensitive to fluctuations in the forcing phase. It is therefore possible to recognise the strange regime by analysing the sensitivity of the state vector to the forcing phase, which is quantified by the "phase-sensitivity exponent" [123]. Mitsui and Aihara [100] confirmed, with this method, the existence of a strange-non-chaotic regime in several models of ice ages displaying an autonomous oscillation including, among others, the van der Pol-like model introduced in (4.3), and the Paillard-Parennin model introduced in Chapter 3, section 5.

So far, we defined the atractor as a transitive attracting invariant set, which is defined in the space spanned by the state space and the forcing. If, however, the forcing is aperiodic, we cannot rely on this definition. However, synchronization may still be defined and characterised. To this end we need to use the language of non-autonomous dynamical systems.

The intuition that a forced system may converge to a synchronised trajectory after the dissipation of transient effects is captured by the notion of pullback attractor [124]. Informally, the section of a pullback attractor at a time t is the set of points that can be reached by the system at this time t if it was started a long time ago (the definition involves the limit $t_0 \to -\infty$). In an system forced by a periodic forcing, the stroboscopic section and the pullback section at a time t are homeomorphic. This follows from the property of system invariance to a time shift by one forcing period. If further periodic forcings are added, then the homeomorphism between pullback attractor and stroboscobic view vanishes. As we have seen, the stroboscopic view may generate different structures, including a strange geometry. However, if there is synchronization, the pullback section still consists of a countable set of points. This is shown on Figure 4.4, left-hand-side column: Starting from arbitrary initial conditions and after dissipation of transient effects, the system reaches one of a countable set of trajectories. The phase of the system is thus constrained by the forcing, but there is no immediate relationship between a forcing phase and the system's phase. The phenomenon is called *generalised synchronization*.

Generalised synchronization may also be detected by considering the long-term, greatest Lyapunov exponent of the forced system, already introduced in chapter 2, section 5. It expresses the average rate of exponential growth of first-order perturbations. A non-synchronised oscillator has a greatest Lypaponov exponent equal to zero. A system whose greatest Lyapunov exponent is negative converges to an attracting trajectory, and therefore can be understood as being "synchronised".

Phase locking, discussed above, is a particular case of generalised synchronization. Consider once more the periodic-forcing case. The transition from non-synchronization to synchronization is a bifurcation. We can therefore define a bifurcation diagram in the space spanned by the forcing parameters, namely its amplitude A and period P. In oscillator models, the bifurcation diagram defines a specific pattern called Arnold tongues. These 'tongues' represent different synchronization regimes corresponding to different rational ratios between the output period and forcing period. The reader is again referred to [119] for an accessible textbook on this matter.

What happens to this diagram when several periodic forcing are combined in the van der Pol and other ice age oscillator models is studied in [120]. Arnold tongues corresponding to the different components of the forcing superimpose each other, such as to creating a wide area of synchronization. Hence, the quasi-periodic character of the astronomical forcing, which contains many harmonics, turns out to make it more likely to induce synchronization of an ice-age oscillator than if the forcing was periodic. However, as we will discuss in the next paragraph, this synchronization is often less reliable than with a periodic forcing.

4.4 Sensitivity to noise

In Chapters 2 and 3 we have seen that understanding the sensitivity of a dynamical system to noise requires an understanding of the attractor as well as a view of the configuration of the vector space around the attractor. For example, if the basin of attraction of the attractor is narrow, stochastic forcing is likely to propel the system state outside the basin of attraction and generate large-amplitude stochastic oscillations.

The existence of astronomical forcing makes the picture more complicated, but it is still possible to rely on the notions of attractor and repeller. The Figure 4.5 shows the projections of the attractors of four glacial-interglacial models, forced by a 3-component forcing. The state-forcing space is projected onto a 3-D hyperplane spanned by one of the state-vectors, together with two

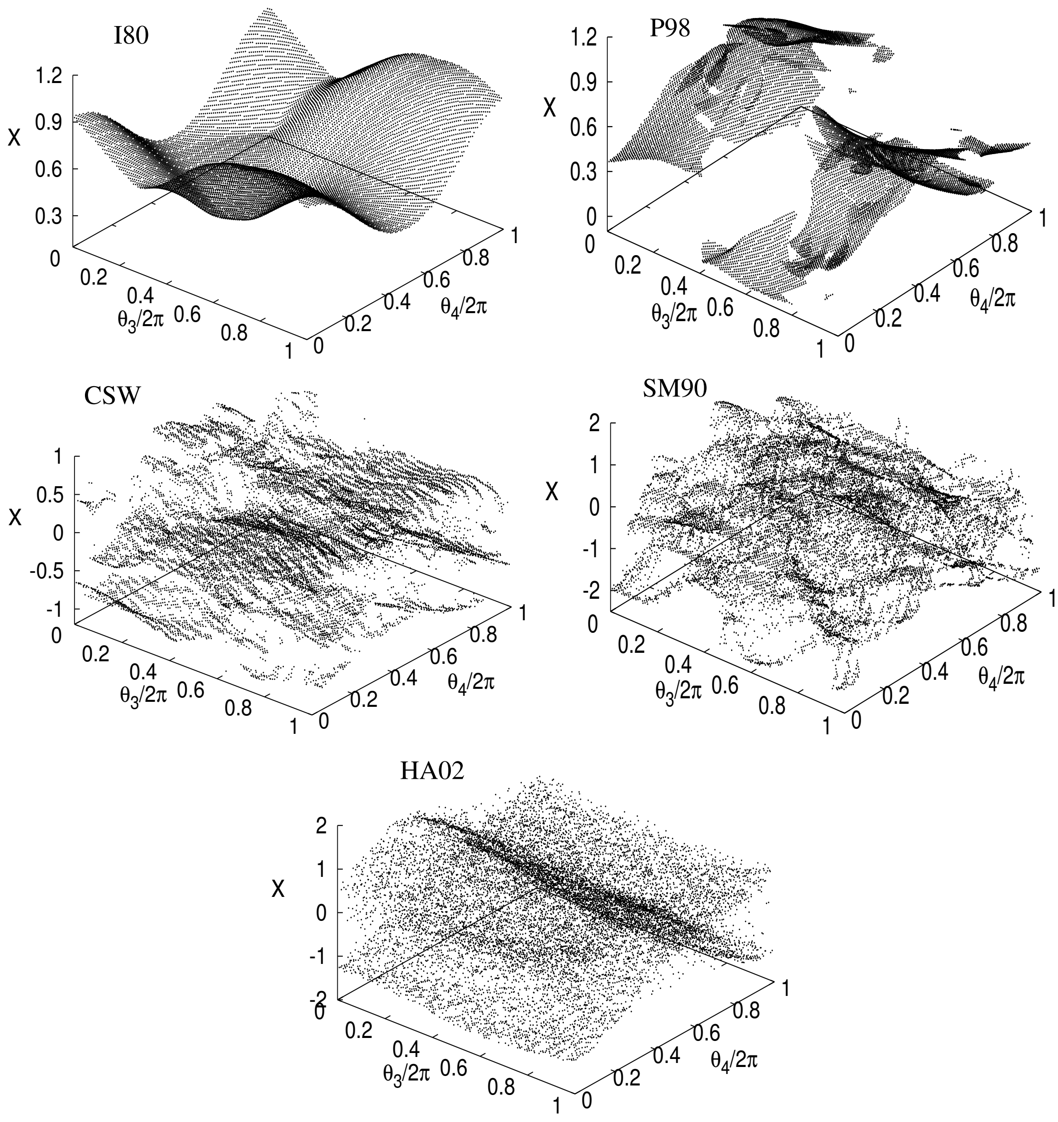

Figure 4.5: Projections of the attractor of four models: P98 [91], CSW (the name used in the original publication for the van der Pol-like oscillator defined in (4.3)), SM90 [92], and HA02 [125]. All models are forced by astronomical forcing, approximated as the as a sum of three periodic harmonics, at frequencies of precession (θ_1, θ_3) and obliquity (θ_4). Figure taken from [126]

forcing phases. We now discuss these projections one by one.

The P98 model was introduced in subsection 3.3. It is a hybrid dynamical system satisfying the strong interpretation of the Milankovitch theory. The projection of the attractor suggests a piecewise continuous geometry. These discontinuities in phase space are related to the regime changes $i \to g \to G$, which cause discontinuous changes in the variation rate of v.

The model labelled "CSW" on Figure 4.5 actually refers to the van der Pol-like oscillator defined in (4.3). The parameter configuration used here generates a strange-non-chaotic attractor, which, as one can see, is qualitatively distinct from the piecewise-continuous attractor of P98. The model SM90 model [92] is another autonomous oscillator, which was introduced to support the hypothesis that carbon cycle instabilities may generate a limit-cycle glacial-interglacial cycle. With the parameters of the original publication, it also produces a strange non-chaotic attractor.

The strange-non-chaotic regime can be a route towards chaos [127], and, indeed, when the SM90 was recalibrated against observations by Hargreaves and Annan, yielding the HA02 model [125], it developed chaos, with largest Lyapunov exponent greater than zero. The qualitative difference between the strange-non-chaotic and strange-chaotic attractors is visible on Figure 4.5, the latter appearing more mixed than the former.

The three kinds of attractors (piece-wise continuous, strange non-chaotic, strange chaotic) appear to represent an increased sensitivity to stochastic noise. In P98, the trajectories remain stable (linear relaxation) as long as the system is within a same regime, g, G, or i. It was found [126] that this configuration makes P98 little sensitive to stochastic forcing: A reasonable amount of noise (small enough to preserve the allure of glacial-interglacial cycles) does not qualitatively affect the sequence of ice ages, nor the structure of the ice-age cycle [126]. Hence, the model satisfies the intuition that the duration of individual ice age cycles is strongly determined by the astronomical forcing.

Systems associated with strange non-chaotic attractors are known to display long, locally stable, transient orbits [128]. To evidence them, Mitsui and Crucifix [100] integrated the model defined in (4.3) until a given time (here: $t = -400$ ka). Starting from this point, they perturbed the system state, and let the integration carry forward. The results of this experiment are shown on Fig. 4.6(a). Even though the perturbation is quite small, the perturbed trajectories (blue) take a long time, up to 1 Ma, to converge towards the pull-back attractor (red). The time at which the perturbation was applied was actually not taken at random: the authors experimented and found a time at which these long transients could effectively be excited with a small perturbation. Once they are produced, these long transients are locally stable most of the time, in the sense that small perturbations around the long-transient decay exponentially. These long transients satisfy the definition of finite-time attractiveness given by Rasmussen [129] (pp. 19–20). The locally-attracting character may also be seen by considering the evolution of the greatest Lyapunov exponent, averaged over a finite time (here, 200 ka, Fig. 4.6(a), bottom graph). Long transient can be excited when the finite-time Lyapunov is positive, and remain stable as long as it is negative.

Consider now the model (4.3), but with an additive stochastic forcing in the first equation:

$$\begin{cases} \dfrac{\mathrm{d}x}{\mathrm{d}t} = (-y + \beta + F(t) + \varepsilon\xi(t))/\tau \\ \dfrac{\mathrm{d}y}{\mathrm{d}t} = -\alpha(y^3/3 - y - x)/\tau \end{cases}$$

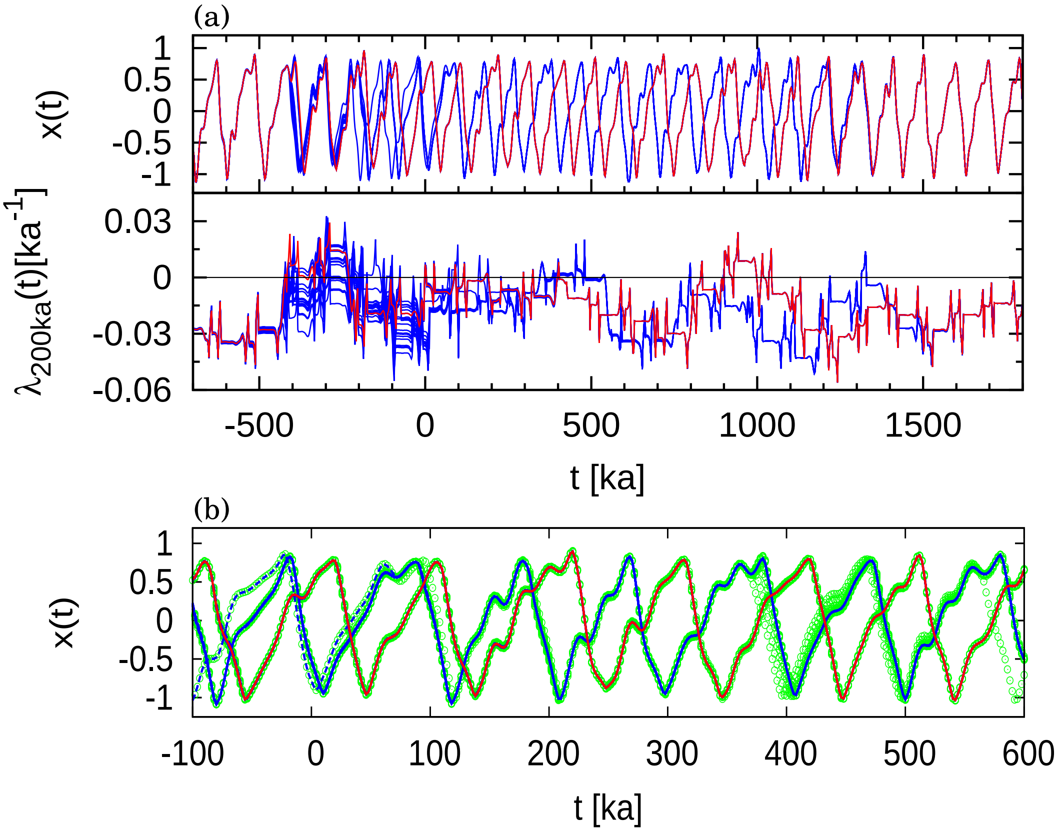

Figure 4.6: Transient orbits with a long lifetime in the van der Pol-like model (4.3) and (4.4): (a) The trajectory corresponding to the attractor of the original noiseless system (red) and some pieces of transient orbits with a long lifetime (blue) (top), along with the finite-time Lyapunov exponent $\lambda_{200\mathrm{ka}}(t)$ (bottom). (b) Twenty trajectories with stochastic forcing with $\varepsilon = 0.002$ (green points). The red and blue lines are the same in the top panel in (a). Figure taken from [100].

Sample trajectories are shown (in green) on Figure 4.6(b), superimposed on the long transients in red and blue. To read the graph more easily, we zoomed over the sample of the time span displayed by 4.6(b). Observe that the stochastic trajectories are distributed over the actual pullback attractor (the trajectory obtained with deterministic model, integrated a long time before), and over the long-transient. The space between the pullback attractor and the long-transient is not populated. Intuitively, the stochastic forcing acts as a photographic developer, which reveals the locally-stable transient trajectories.

Hence, if we run a large number of stochastic simulations, the simulated states, at a time t, will appear organised around a number of clusters, which correspond to the pullback attractors and the long-transient trajectories existing in the deterministic system. If the stochastic forcing is small, then the clusters are neatly separated from each other. As the amplitude of the stochastic forcing increases, trajectories may jump between leave their local attractors and travel to another attractor or another long-transient. We now compare ttwo versions of a same deterministic model, SM90, and HA02. Remember that in SM90, the long-term Lyapuonov exponent (with astronomical forcing) is negative, indicating that it satisfies the criteria of generalised synchronization. HA02 is, again, the same model, but the parameters were adjusted to maximise the agreement with observations. In this case, the long-term Lyapunov exponent is positive: it is chaotic. Both models have finite-time Lyapunov exponents varying between negative and positive values. We now consider 10000 stochastic simulations, with a small amount of noise and ask how many points do not belong to a cluster (see method details and parameter values in [100]). This number varies over time, therefore the authors have provided a frequency histogram. As we see it (Figure 4.7), in SM90, most of the time, all stochastic realizations belong to a cluster. There is little leakage from one cluster to the next, suggesting that the system is very predictable because it is tightly controlled by the astronomical forcing. In HA02, the chaotic system, we find most of the time between 5 and 20 mavericks. It is not much (remember we have 10000 trajectories), but yet suggests that the synchronization is less reliable.

The qualitative change between the non-chaotic and the chaotic versions of the model is thus not very dramatic. In both cases, the vast majority of stochastic trajectories are grouped around a small (between 1 and 5) number of clusters, implying that the sequence of ice ages is effectively controlled by the astronomical forcing. However, the chaotic system has more leakage, and it is therefore more unpredictable, even at small noise levels.

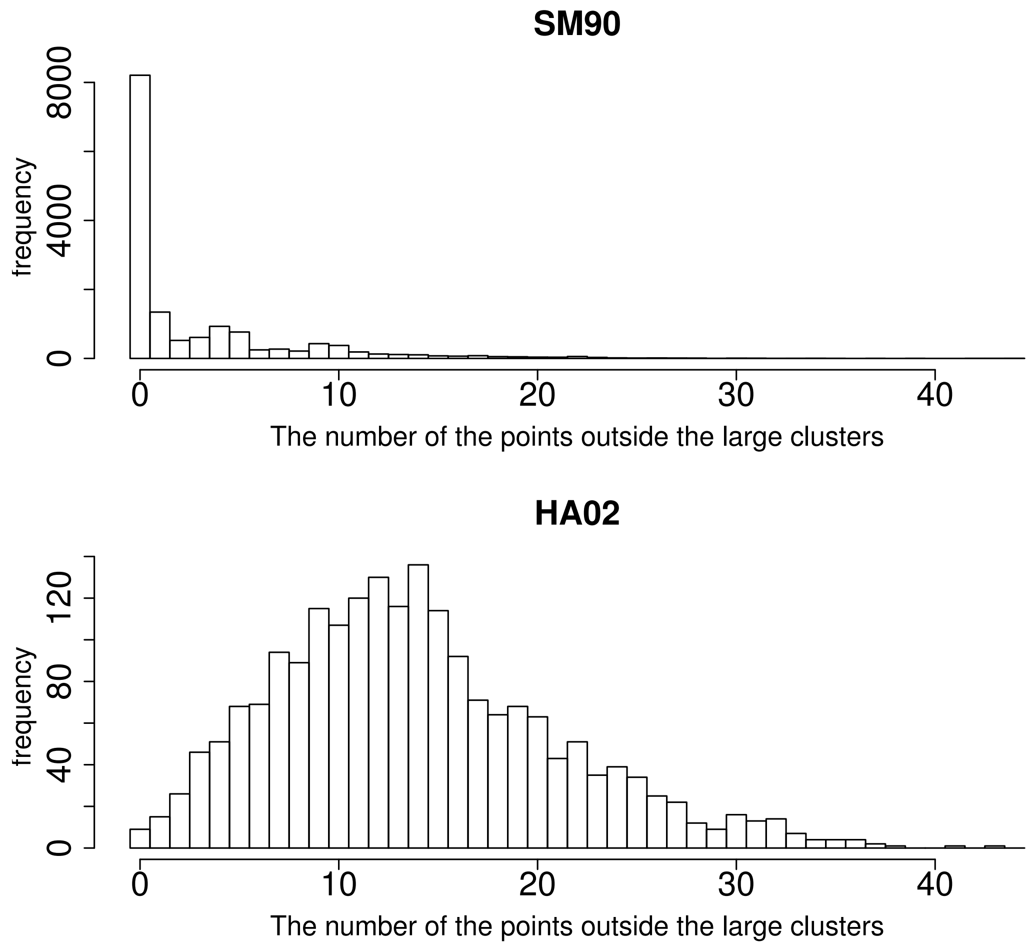

Figure 4.7: Histogram of the number of “mavericks”, defined as states which do not belong to clusters of trajectories similar to those shown on Figure 4.6(b), in two dynamical systems: SM90 and HA02. Figure taken from [100].

Chapter 5

Conclusions

In this review, a number of available deterministic conceptual models of climate dynamics served as a basis to deepen our understanding of the mechanisms which may generate the climate oscillations observed in palaeoclimate records. As a rule, we considered the models with their original, published parameter values, and studied how the regimes of oscillators may appear when some key parameters vary, either in a deterministic or in a random manner, or when a stochastic forcing is added. It was shown that even very small parameter changes, or small amounts of stochastic forcing, may qualitatively deform the dynamical modes. To analyse this phenomenon, it is necessary to understand the types of bifurcations which may take place in these models.

We started with the model (2.5) (see Section), which describes a nonlinear feedback between the ocean temperature and sea ice extent [52]. This simple 2-dimensional model undergoes saddle-node and sub/supercritical Andronov-Hopf bifurcations, and exhibits multistability with the coexistence of a limit cycle and two equilibria. In the conditions of multistability, the presence of noise further diversifies the dynamic scenarios. We showed how noise-induced transitions between attractors can generate mixed-mode fluctuations with alternations of small- and large-amplitude stochastic oscillations, and also cause an order-to-chaos transition. A transition to chaos is expected to drastically reduce the forecast horizon of the system.

Even in the framework of two-dimensional models, one can get a non-trivial description of catastrophic climate changes. Here, a typical example is the temperature-vegetation model [49] (see Section 2.2). The behaviour of this model is caused by the association of an Andronov-Hopf bifurcation, with the simultaneous existence of two attractors associated with opposite states of climate: snowball Earth (stable equilibrium) and vegetated earth (stable equilibrium or limit cycle). In the framework of the deterministic theory, transitions between these climate states are not possible. However, noise of increasing intensity leads to a systematic decrease of the average temperature and, in the end, can cause a catastrophic shift of the climate system from the favourable state of vegetation to the snowball Earth mode.

Accounting for additional climatic variables and processes leads us models of higher dimension. One of the first 3-dimensional models of glacial-interglacial cycles was proposed by Saltzman and Sutera [39] (see Section 3.1). This system governs the dynamics of the continental and marine ice masses and it introduces a variable called the mean ocean temperature. The peculiar behaviour of this model is caused by a special type of bifurcation: a so-called saddle-node bifurcation on an invariant cycle (SNIC), which was not observed in 2-dimensional climate models considered above. We have shown that near the SNIC bifurcation the equilibrium is extremely excitable: even small random noise can cause large-amplitude spike oscillations. As a result, the stochastic system exhibits a complex dynamic mode with the alternation of SASO and LASO. This oscillatory regime is also followed by a transition from order to chaos.

This scenario turns out not to be an exclusive feature of the model (3.1). Indeed, the SNIC bifurcation associated with this scenario is also observed in another 3-dimensional model (3.7) describing the interactions of CO_2 concentration, ice mass, and deep ocean temperature (see Section 3.2).

Note that proximity to SNIC bifurcation is not the only cause of stochastic excitability. In the 3-dimensional climate models considered here, another scenario of the stochastic excitability is possible near the saddle-node bifurcation of limit cycles, in the zone, where the initial unforced deterministic model exhibits the stable equilibrium regime only. Such a scenario was discussed in Section using the example of the Paillard and Parrenin [79] climate model. This model describes the dynamics of the global ice volume, the area of the Antarctic continental ice sheet, and the atmospheric concentration of carbon dioxide. For this model, we show a mechanism of the stochastic excitation of LASO in the zone of stable equilibria when the parameter approaches the saddle-node bifurcation point.

At the scale of glacial-interglacial cycles, it is also essential to take into account the forcing caused by the oscillations in Earth's orbital parameters and obliquity. In the literature this forcing is commonly referred to as Milankovitch, orbital, or astronomical forcing. Concretely, the forcing can be expressed as a series of harmonics. It can produce oscillations in ice volume in models which, without forcing, have only one fixed point (strong interpretation of Milankovitch theory), or it can synchronise oscillations in models which, in absence of forcing, present a limit cycle (weak interpretation). Both cases may be conducive to the emergence of strange non-chaotic attractors, though in practice, they have mainly been observed in synchronization scenarios. The strange non-chaotic attractor presents different specificities: it is associated with aperiodic trajectories (even though the forcing is quasi-periodic), trajectories are generally stable, but the attractor and repellers may be arbitrarily close to each other. Consequently, there are episodic moments when a very small perturbation may produce a long transient orbit. The effect of even a small amount of stochastic forcing is to excite these long transient orbits, which produces a form of unpredictability. For these reasons, such systems are said to have a regime which is intermediate between order and chaos.

Hence, the interaction of stochasticity and nonlinearity generates a great diversity of possible behaviours, which can be decoded and understood by reference to the bifurcation structure. Some of the models that we have studied may appear overly conceptual, and they may no longer appear to be an adequate description of glacial-interglacial cycles. The key point, however, is that they describe mechanisms which, at one point, have been considered to be relevant (e.g., the relationship in sea ice and ocean temperature), and which may still have some relevance at other time scales. For example, the Dansgaard-Oeschger oscillations, which we briefly introduced in Chapter 1, involve the ice sheets, the sea ice, and ocean circulation. Hence, we are confident that the description of various possible modes of climate dynamics and mechanisms of their occurrence obtained here will become a beachhead for understanding higher-dimensional models, which take into account new physical factors and more adequately reflect both available and newly obtained paleoclimate records.

On this basis, we may formulate what we consider to be our main conclusion. The nonlinear dynamics is capable of describing a great variety of evolutionary climate scenarios even in the framework of existing dynamical models. However, it is more realistic to consider that stochastic effects will inevitably affect several model parameters simultaneously. These stochastic forcings are caused by various physical processes, which have different intensities. We found that such effects may easily generate quite complex stochastically induced phenomena, such as random walks of the phase trajectories, abrupt transitions between attractors, formation of mixed-mode oscillations, appearance of phantom attractors and chaotization. Of course, simulating such complex dynamics could potentially require costly simulations on supercomputers. It is, in practice, impossible to investigate dynamic models taking into account various noises in all coefficients of the equations. For this reason we focus here on possible stochastic responses of the system to the presence of noise in one of the coefficients (in a specific process). Yet, the results that we obtained demonstrate the appearance of evolutionary climate scenarios that have no analogues in the framework of the deterministic theory. We therefore argue that the conceptual understanding of climate oscillations needs be expanded to account for these stochastic scenarios. From this point of view, the results obtained should not be taken as accurate prediction of the temporal behaviour of the main variables of the models under consideration. They show possibilities associated with the existence of stochastic forcings.

Acknowledgements This work was supported by the Russian Science Foundation (Grant No. 16-11-10095).

Appendix A. Stochastic sensitivity technique

As a general dynamical model, consider the system of nonlinear Ito's stochastic differential equations

$$\dot{x} \;=\; f(x) + \varepsilon\sigma(x)\xi(t), \tag{5.1}$$

where x is an n-dimensional vector of the system state, $f(x)$ is an n-vector function, $\sigma(x)$ is an $n \times m$-matrix function, $\xi(t)$ is an m-dimensional white Gaussian noise with parameters $\mathrm{E}\xi(t) = 0$, $\mathrm{E}\xi(t)\xi^\top(\tau) = \delta(t-\tau)I$, I is an identity $m \times m$-matrix, and ε is a scalar parameter of the noise intensity.

Let the corresponding deterministic system (5.1) with $\varepsilon = 0$ have an exponentially stable attractor A. This means that for the small neighbourhood D of the attractor A, there exist positive constants K and l such that for any solution $x(t)$ of the deterministic system with the initial condition $x(0) = x_0 \in D$ the following inequality holds

$$||\vartriangle(x(t))|| \leq Ke^{-lt}||\vartriangle(x_0)||$$

for $t > 0$. Here, $\vartriangle(x) = x - \gamma(x)$ is a vector of a deviation of the point x from the attractor A, $\gamma(x)$ is a point of the attractor A that is nearest to x.

Under stochastic disturbances, random solutions $x^\varepsilon(t)$ of system (5.1) form some flow. Dynamics of this flow is defined by the probability density function $\rho(t, x, \varepsilon)$. This function is governed by the following Kolmogorov–Fokker–Planck equation [130, 131]

$$\frac{\partial\rho}{\partial t} \;=\; L\rho, \quad L\rho \;=\; \frac{\varepsilon^2}{2}\sum_{i,j=1}^{n}\frac{\partial^2}{\partial x_i \partial x_j}(a_{ij}\rho) - \sum_{i=1}^{n}\frac{\partial}{\partial x_i}(f_i\rho), \quad a_{ij} = [\sigma\sigma^\top]_{ij}.$$

In many cases, a character of the transient process is unessential and the main interest of the study is focused on the stable stationary regime. In these circumstances, in the stochastic analysis one should use the stationary density function $\rho(x, \varepsilon)$. This function is a solution of the stationary Kolmogorov–Fokker–Planck equation

$$L\rho = 0.$$

The direct solution of this equation is very difficult from the technical point of view even for the two-dimensional case. In these circumstances, asymptotics and approximations are actively used. In this range, an asymptotics based on the quasipotential

$$v(x) = -\lim_{\varepsilon\to 0} \varepsilon^2 \ln \rho(x,\varepsilon)$$

is well known [132].

The quasipotential $v(x)$ is related to some variational problem of the minimization of the action potential and governed by the Hamilton–Jacobi equation

$$\left(f(x), \frac{\partial v}{\partial x}\right) + \frac{1}{2}\left(\frac{\partial v}{\partial x}, \sigma(x)\sigma^\top(x)\frac{\partial v}{\partial x}\right) = 0$$

with conditions $v|_A = 0\,,\;\; v|_{D\setminus A} > 0$.

An analytical solution of this equation is still difficult problem in general case. However, main features of the behavior of the quasipotential $v(x)$ near the attractor A can be described by the following quadratic approximation [133]

$$v(x) \approx \frac{1}{2}(\Delta(x), \Phi(\gamma(x))\Delta(x)),\;\; \Phi(x) = \frac{\partial^2 v}{\partial x^2}(x).$$

Let us discuss constructive methods of such approximations when equilibria and cycles are attractors of the initial deterministic system.

Stochastic sensitivity of equilibria

Let the attractor of the deterministic system be an exponentially stable equilibrium $\bar{x}$. In this case, the quadratic approximation $v(x) \approx \frac{1}{2}(x - \bar{x}, \Phi(\bar{x})(x-\bar{x}))$ of the quasipotential gives an asymptotics of the probability density function $\rho(x,\varepsilon)$ in a neighbourhood of the equilibrium $\bar{x}$ in the following Gaussian form

$$\rho(x,\varepsilon) \approx N \exp\left(-\frac{(x-\bar{x}, W^{-1}(x-\bar{x}))}{2\varepsilon^2}\right),\;\; W = \Phi^{-1}(\bar{x}).$$

Here, parameters of the Gaussian distribution are defined by the mean value $\bar{x}$, the covariance matrix $C = \varepsilon^2 W$, and the normalization constant, N. The matrix W is a solution of the equation

$$FW + WF^\top + S = 0, \tag{5.2}$$

where $F = \dfrac{\partial f}{\partial x}(\bar{x})$ is the Jacobi matrix of the deterministic system at the equilibrium point $\bar{x}$ and $S = \sigma(\bar{x})\sigma^\top(\bar{x})$.

Because of the exponential stability of the equilibrium $\bar{x}$, the eigenvalues of the Jacobi matrix F have negative real parts, and the matrix equation (5.2) has a unique solution W. The matrix W is called the stochastic sensitivity matrix of the equilibrium $\bar{x}$ in system (5.1) [134]. The stochastic sensitivity matrix W allows us to approximate the mean-square variation of the stationary distributed solution $x^\varepsilon(t)$ of system (5.1) as follows

$$\mathrm{E}(x^\varepsilon(t) - \bar{x})(x^\varepsilon(t) - \bar{x})^\top \approx \varepsilon^2 W.$$

Stochastic sensitivity of limit cycles

Consider now the case when the attractor of the deterministic system is an exponentially stable limit cycle defined by a T-periodic solution $\bar{x}(t)$, $\bar{x}(t+T) = \bar{x}(t)$. Denote by Π_t a hyperplane which is orthogonal to the cycle at the point $\bar{x}(t)$. For the Poincare section Π_t in the neighbourhood of the point $\bar{x}(t)$, the quadratic approximation

$$v(x)|_{\Pi_t} \approx \frac{1}{2}\left(x - \bar{x}(t), \Phi(\bar{x}(t))(x - \bar{x}(t))\right)$$

of the quasipotential gives the asymptotics $\rho_t(x, \varepsilon)$ of the probability density $\rho(x, \varepsilon)|_{\Pi_t}$ in the following Gaussian form

$$\rho_t(x, \varepsilon) = N \exp\left(-\frac{(x - \bar{x}(t), W^+(t)(x - \bar{x}(t)))}{2\varepsilon^2}\right), \quad W(t) = \Phi^+(\bar{x}(t)).$$

Parameters of the Gaussian distribution are defined by the mean value $\bar{x}(t)$ and covariance matrix $C(t) = \varepsilon^2 W(t)$. Here, the sign "+" means the pseudoinversion [135].

For the exponentially stable limit cycle, the matrix function $W(t)$ is a unique solution of the boundary problem [136]

$$\begin{aligned} \dot{W} &= F(t)W + WF^\top(t) + P(t)S(t)P(t) \\ W(0) &= W(T) \\ W(t)r(t) &\equiv 0. \end{aligned} \tag{5.3}$$

Here,

$$F(t) = \frac{\partial f}{\partial x}(\bar{x}(t)), \;\; S(t) = \sigma(\bar{x}(t))\sigma^\top(\bar{x}(t)), \;\; r(t) = f(\bar{x}(t)), \;\; P(t) = P_{r(t))},$$

and $P_r = I - rr^\top / r^\top r$ is a projection matrix onto the hyperplane that is orthogonal to the vector r.

The T-periodic matrix $W(t)$ defines the stochastic sensitivity of the limit cycle $\bar{x}(t),\ t \in [0, T]$ in the stochastic system (5.1).

In two-dimensional case, the stochastic sensitivity matrix $W(t)$ can be written in the form

$$W(t) = m(t)p(t)p^\top(t),$$

where $p(t)$ is a normalized vector that is orthogonal to $f(\bar{x}(t))$.

The scalar function $m(t) > 0$ is a T-periodic stochastic sensitivity function of the limit cycle. The function $m(t)$ is a unique solution of the following boundary problem [134]

$$\dot{m} = a(t)m + b(t), \;\; m(0) = m(T) \tag{5.4}$$

with the T-periodic coefficients

$$a(t) = p^\top(t)(F^\top(t) + F(t))p(t)\ ,\ b(t) = p^\top(t)S(t)p(t).$$

Here, an explicit formula for the solution $m(t)$ of the problem (5.4) can be derived:

$$m(t) = g(t)(c + h(t)),$$

where

$$g(t) = \exp\left(\int_0^t a(s)ds\right), \quad h(t) = \int_0^t \frac{b(s)}{g(s)}ds, \qquad c = \frac{g(T)h(T)}{1 - g(T)}.$$

The maximum value $M = \max m(t),\ t \in\ [0, T]$ can be used in the stochastic analysis of the forced limit cycle as a whole. We call M the *stochastic sensitivity factor* of the cycle.

Appendix B. Mahalanobis metrics and method of confidence domains

The stochastic sensitivity matrix of the attractor is an asymptotics which allows us to describe quantitatively a dispersion of random states around the attractor in the stochastically forced system. To visualize this spatial probabilistic distribution of random states around the attractor, the confidence domains can be used.

First, consider a case when the stable equilibrium $\bar{x}$ is an attractor of the unforced $n-$dimensional deterministic model. Let W be a stochastic sensitivity matrix of this equilibrium. Around the equilibrium $\bar{x}$, one can construct a confidence ellipsoid:

$$\big(x-\bar{x}, W^{-1}(x-\bar{x})\big) = \varepsilon^2 K(P), \tag{5.5}$$

where P is a fiducial probability. The function $K(P)$ is an inverse function to $P(K)$:

$$P(K) = \frac{\Phi_n(K)}{\Phi_n(\infty)}, \qquad \Phi_n(K) = \int\limits_0^{\sqrt{K}} e^{-\frac{t^2}{2}}\, t^{n-1} dt.$$

The equation (5.5) of the confidence ellipsoid can be rewritten as

$$d_M^2(x,\bar{x}) = \varepsilon^2 K(P),$$

where

$$d_M(x,\bar{x}) = \sqrt{(x-\bar{x}, W^{-1}(x-\bar{x}))}.$$

The function $d_M(x,\bar{x})$ can be considered as the Mahalanobis distance [137]. Surfaces on which $d_M(x,\bar{x})$ is constant are confidence ellipsoids that are centered about the mean $\bar{x}$. So, the stochastic sensitivity matrix W defines a new statistic metrics related to the randomly forced system (5.1).

In one-dimensional case ($n=1$),

$$P(K) = \sqrt{\frac{2}{\pi}} \int\limits_0^{\sqrt{K}} e^{-\frac{t^2}{2}}\, dt = \mathrm{erf}\left(\sqrt{\frac{K}{2}}\right), \quad \mathrm{erf}(x) = \frac{2}{\sqrt{\pi}} \int\limits_0^{x} e^{-t^2} dt,$$

and the corresponding confidence interval $(\bar{x} - r, \bar{x} + r)$ is defined by $r = \varepsilon\sqrt{2\mu}\,\mathrm{erf}^{-1}(P)$, where the stochastic sensitivity μ can be found from the explicit formula:

$$\mu = -\frac{\sigma^2(\bar{x})}{2f'(\bar{x})}.$$

For the 3σ-rule, it holds that $r = 3\varepsilon\sqrt{\mu}$.

In two-dimensional case ($n = 2$),

$$P(K) = 1 - \mathrm{e}^{-\frac{K}{2}}, \qquad K(P) = -2\ln(1 - P).$$

The equation of the confidence ellipse with $\bar{x}$ as an origin can be written as

$$\frac{\beta_1^2}{\lambda_1} + \frac{\beta_2^2}{\lambda_2} = \varepsilon^2 K(P), \qquad \beta_1 = (x - \bar{x}, v_1), \;\; \beta_2 = (x - \bar{x}, v_2). \tag{5.6}$$

Here, λ_1, λ_2 are the eigenvalues, v_1, v_2 are the normalized eigenvectors of the stochastic sensitivity matrix W, and β_1, β_2 are coordinates of this ellipse in the basis of the eigenvectors v_1, v_2. These eigenvectors define directions of the confidence ellipse axis, and λ_1, λ_2 define the values of corresponding semi-axis.

In three-dimensional case ($n = 3$),

$$P(K) = \sqrt{\frac{2}{\pi}}\left[\int\limits_0^{\sqrt{K}} e^{-\frac{t^2}{2}}\,dt - \sqrt{K}e^{-\frac{K}{2}}\right] = \mathrm{erf}\left(\sqrt{\frac{K}{2}}\right) - \sqrt{\frac{2K}{\pi}}\mathrm{e}^{-\frac{K}{2}}.$$

The confidence ellipsoid can be written in the following form

$$\frac{\beta_1^2}{\lambda_1} + \frac{\beta_2^2}{\lambda_2} + \frac{\beta_3^2}{\lambda_3} = \varepsilon^2 K(P), \tag{5.7}$$

where $\beta_1 = (x - \bar{x}, v_1)$, $\beta_2 = (x - \bar{x}, v_2)$, $\beta_3 = (x - \bar{x}, v_3)$ are coordinates of this ellipse in the basis of the eigenvectors v_1, v_2, v_3, and $\lambda_1, \lambda_2, \lambda_3$ are the eigenvalues of the stochastic sensitivity matrix W.

Consider now a case when the attractor of the deterministic system is an exponentially stable limit cycle defined by a T-periodic solution $\bar{x}(t)$. Let $W(t)$ be the stochastic sensitivity matrix of this cycle in the randomly forced system (5.1). In this case, the Mahalanobis distance is defined by the function

$$d_M(x, \bar{x}(t)) = \sqrt{(x - \bar{x}(t), W^{+}(t)(x - \bar{x}(t)))}.$$

In two-dimensional case, this Mahalanobis distance has a simple representation

$$d_M(x, \bar{x}(t)) = \frac{\|x - \bar{x}(t)\|}{\sqrt{m(t)}},$$

where $m(t)$ is the solution of the boundary problem (5.4) and $\|\cdot\|$ is a standard Euclid distance.

Using the stochastic sensitivity function $m(t)$, one can construct a confidence band around the deterministic cycle in the following way. Let Π_t be a line that is orthogonal to the cycle at the point $\bar{x}(t)$. The boundaries $x_{1,2}(t)$ of the confidence band on this line can be found in an explicit parametric form:

$$x_{1,2}(t) = \bar{x}(t) \pm \varepsilon\sqrt{2m(t)}\,\mathrm{erf}^{-1}(P)p(t). \tag{5.8}$$

It is worth noting that confidence domains are sufficiently simple and evident models for the spatial description of the distribution of random states near the deterministic attractors. The method of confidence domains based on the stochastic sensitivity functions technique was successfully applied to the study of noise-induced effects in dynamical models from the various domains of science [138–142].

Bibliography

[1] T.M. Cronin. *Principles of Paleoclimatology*. The Critical Moments and Perspectives in Earth History and Paleobiology. Columbia University Press, 1999.

[2] J. C. Zachos, G. R. Dickens, and R. E. Zeebe. An early cenozoic perspective on greenhouse warming and carbon-cycle dynamics. *Nature*, 451(7176):279283, 2008.

[3] K. D. Burke, J. W. Williams, M. A. Chandler, A. M. Haywood, D. J. Lunt, and B. L. Otto-Bliesner. Pliocene and eocene provide best analogs for near-future climates. *Proceedings of the National Academy of Sciences*, page 201809600, 2018.

[4] M. Gutjahr, A. Ridgwell, P. F. Sexton, E. Anagnostou, P. N. Pearson, H. Plike, R. D. Norris, E. Thomas, and G. L. Foster. Very large release of mostly volcanic carbon during the palaeoceneeocene thermal maximum. *Nature*, 548(7669):573577, 2017.

[5] S. Kirtland Turner, P. M. Hull, L. R. Kump, and A. Ridgwell. A probabilistic assessment of the rapidity of petm onset. *Nature Communications*, 8(1), 2017.

[6] W. F. Ruddiman, M. Raymo, and A. McIntyre. Matuyama 41,000-year cycles: North atlantic ocean and northern hemisphere ice sheets. *Earth and Planetary Science Letters*, 80:117–129, 1986.

[7] L. E. Lisiecki and M. E. Raymo. Plio-pleistocene climate evolution: trends and transitions in glacial cycles dynamics. *Quaternary Science Reviews*, 26:56–69, 2007.

[8] H. Elderfield, P. Ferretti, M. Greaves, S. Crowhurst, I. N. McCave, D. Hodell, and A. M. Piotrowski. Evolution of ocean temperature and ice volume through the mid-pleistocene climate transition. *Science*, 337(6095):704–709, 2012.

[9] W. S. Broecker and J. van Donk. Insolation changes, ice volumes and the o^{18} record in deep-sea cores. *Reviews of Geophysics*, 8(1):169–198, 1970.

[10] L. E. Lisiecki and M. E. Raymo. A pliocene-pleistocene stack of 57 globally distributed benthic δ^{18}o records. *Paleoceanography*, 20:PA1003, 2005.

[11] J. R. Petit, J. Jouzel, D. Raynaud, N. I. Barkov, J. Barnola, I. Basile, M. Bender, J. Chappellaz, M. Davis, G. Delaygue, M. Delmotte, V. M. Kotlyakov, M. Legrand, V. Y. Lipenkov, C. Lorius, L. Ppin, C. Ritz, E. Saltzman, and M. Stievanard. Climate and atmospheric history of the past 420,000 years from the vostok ice core, antarctica. *Nature*, 399(6735):429436, 1999.

[12] D. Lthi, M. Le Floch, B. Bereiter, T. Blunier, J. M. Barnola, U. Siegenthaler, D. Raynaud, J. Jouzel, H. Fischer, K. Kawamura, and T. F. Stocker. High-resolution carbon dioxide concentration record 650,000-800,000 years before present. *Nature*, 453(7193):379–382, 2008.

[13] C. Emiliani. Pleistocene temperatures. *The Journal of Geology*, 63:538, 1955.

[14] G. C. Bond, W. Showers, M. Elliot, M. Evans, R. Lotti, I. Hajdas, G. Bonani, and S. Johnson. The North Atlantic's 1-2 kyr climate rhythm: Relation to Heinrich events, Dansgaard/Oeschger cycles and the little ice age. In *Mechanisms of Global Climate Change at Millennial Time Scales*, pages 35–58. American Geophysical Union, 1999.

[15] C. Lang, M. Leuenberger, J. Schwander, and S. Johnsen. 16°c rapid temperature variation in central Greenland 70,000 years ago. *Science*, 286(5441):934–937, 1999.

[16] J. P. Steffensen, K. K. Andersen, M. Bigler, H. B. Clausen, D. Dahl-Jensen, H. Fischer, K. Goto-Azuma, M. Hansson, S. u. s. J. Johnsen, J. Jouzel, V. Masson-Delmotte, T. Popp, S. O. Rasmussen, R. Rthlisberger, U. Ruth, B. Stauffer, M. L. Siggaard-Andersen, A. Sveinbjrnsdttir, A. Svensson, and J. W. C. White. High-resolution Greenland ice core data show abrupt climate change happens in few years. *Science*, 321(5889):680–684, 2008.

[17] J. Jouzel, V. Masson-Delmotte, O. Cattani, G. Dreyfus, S. Falourd, G. Hoffman, B. Minster, J. Nouet, J. M. Barnola, J. Chappellaz, H. Fisher, J. C. Gallet, S. Johnsen, M. Leuenberger, L. Loulergue,

D. Luethi, H. Oerter, F. Parrenin, G. Raisbeek, D. Raynaud, J. Schwander, R. Spahni, R. Souchez, E. Selmo, A. Shilt, J. P. Steffensen, B. Stenni, B. Stauffer, T. F. Stocker, J. L. Tison, M. Werner, and E. W. Wolff. Orbital and millennial Antarctic climate variability over the last 800 000 years. *Science*, 317(5839):793–796, 2007.

[18] S. Barker, G. Knorr, L. R. Edwards, F. Parrenin, A. E. Putnam, L. C. Skinner, E. Wolff, and M. Ziegler. 800,000 years of abrupt climate variability. *Science*, 334(6054):347–351, 2011.

[19] J. F. McManus, G. C. Bond, W. S. Broecker, S. Johnsen, L. Labeyrie, and S. Higgins. High-resolution climate records from the north atlantic during the last interglacial. *Nature*, 371(6495):326329, 1994.

[20] M. F. Sanchez Goni, E. Bard, A. Landais, L. Rossignol, and F. d/'Errico. Air-sea temperature decoupling in western Europe during the last interglacial-glacial transition. *Nature Geosciences*, 6(10):837–841, 2013.

[21] D. Oliveira, S. Desprat, T. Rodrigues, F. Naughton, D. Hodell, R. Trigo, M. Rufino, C. Lopes, F. Abrantes, and M. F. S. Goni. The complexity of millennial-scale variability in southwestern europe during mis 11. *Quaternary Research*, 86(3):373387, 2016.

[22] J. Weertman. Milankovitch solar radiation variations and ice age ice sheet sizes. *Nature*, 261, 1976.

[23] M. Milankovitch. *Canon of insolation and the ice-age problem*. Narodna biblioteka Srbije, 1998. English translation of the original 1941 publication.

[24] J. Weertman. Stability of ice-age ice sheets. *Journal of Geophysical Research*, 66(11):3783–3792, 1961.

[25] A. Abe-Ouchi, F. Saito, K. Kawamura, M. E. Raymo, J. I. Okuno, K. Takahashi, and H. Blatter. Insolation-driven 100,000-year glacial cycles and hysteresis of ice-sheet volume. *Nature*, 500(7461):190–193, 2013.

[26] H. A. Dijkstra and M. Ghil. Low-frequency variability of the large-scale ocean circulation: A dynamical systems approach. *Reviews of Geophysics*, 43(3), 2005.

[27] N. Boers, M. Ghil, and D. Rousseau. Ocean circulation, ice shelf, and sea ice interactions explain dansgaardoeschger cycles. *Proceedings of the National Academy of Sciences*, 115(47):E11005E11014, 2018.

[28] P. Schulte, L. Alegret, I. Arenillas, J. A. Arz, P. J. Barton, P. R. Bown, T. J. Bralower, G. L. Christeson, P. Claeys, C. S. Cockell, and et al. The chicxulub asteroid impact and mass extinction at the cretaceous-paleogene boundary. *Science*, 327(5970):12141218, 2010.

[29] C. C. Raible, S. Brnnimann, R. Auchmann, P. Brohan, T. L. Frlicher, H. Graf, P. Jones, J. Luterbacher, S. Muthers, R. Neukom, and et al. Tambora 1815 as a test case for high impact volcanic eruptions: Earth system effects. *Wiley Interdisciplinary Reviews: Climate Change*, 7(4):569589, 2016.

[30] R. J. Haarsma, M. J. Roberts, P. L. Vidale, C. A. Senior, A. Bellucci, Q. Bao, P. Chang, S. Corti, N. S. Fučkar, V. Guemas, J. von Hardenberg, W. Hazeleger, C. Kodama, T. Koenigk, L. R. Leung, J. Lu, J. Luo, J. Mao, M. S. Mizielinski, R. Mizuta, P. Nobre, M. Satoh, E. Scoccimarro, T. Semmler, J. Small, and J. von Storch. High resolution model intercomparison project (highresmip v1.0) for cmip6. *Geoscientific Model Development*, 9(11):4185–4208, 2016.

[31] F. Pattyn. The paradigm shift in Antarctic ice sheet modelling. *Nature Communications*, 9(1), 2018.

[32] P. Martinez, P. Bertrand, I. Bouloubassi, G. Bareille, G. Shimmield, B. Vautravers, F. Grousset, S. Guichard, Y. Ternois, and M. Sicre. An integrated view of inorganic and organic biogeochemical indicators of palaeoproductivity changes in a coastal upwelling area. *Organic Geochemistry*, 24(4):411420, 1996.

[33] I. M. Held. The gap between simulation and understanding in climate modelling. *Bull. Am. Meteorol. Soc.*, 86(11):1609–1614, 2005.

[34] M. I. Budyko. The effect of solar radiation variations on the climate of the Earth. *Tellus*, 21(5):611–619, 1969.

[35] W. D. Sellers. A global climatic model based on the energy balance of the Earth-atmosphere system. *Journal of Applied Meteorology*, 8(3):392–400, 1969.

[36] M. Ghil. Climate stability for a sellers-type model. *J. Atmos. Sci.*, 33:3–20, 1976.

[37] G. R. North, L. Howard, D. Pollard, and B. Wielicki. Variational formulation of Budyko-Sellers climate models. *Journal of the Atmospheric Sciences*, 36(2):255–259, 1979.

[38] M. Ghil. A century of nonlinearity in the geosciences. *Earth and Space Science*, 6(7):10071042, 2019.

[39] B. Saltzman, A. Sutera. A model of the internal feedback system involved in late quaternary climatic variations. *J. Atmospheric Sci.*, 41:736–745, 1984.

[40] R. Benzi, G. Parisi, A. Sutera, and A. Vulpiani. Stochastic resonance in climatic change. *Tellus*, 34(1):10–16, 1982.

[41] C. Nicolis. Stochastic aspects of climatic transitions — response to a periodic forcing. *Tellus*, 34(1):1–9, 1982.

[42] J. Imbrie and J. Z. Imbrie. Modelling the climatic response to orbital variations. *Science*, 207:943–953, 1980.

[43] E. Käll, C. Crafoord, and M. Ghil. Free oscillations in a climate model with ice-sheet dynamics. *Journal of Climate*, 36:2292–2303, 1979.

[44] M. Crucifix. Oscillators and relaxation phenomena in pleistoceene climate theory. *Phil. Trans. R. Soc. A*, 370:1140–1165, 2012.

[45] L. Arnold. *Random Dynamical Systems*. Springer-Verlag, 1998.

[46] K. Hasselmann. Stochastic climate models part i. theory. *Tellus*, 28(6):473–485, 1976.

[47] C. Penland. Noise out of chaos and why it won't go away. *Bulletin of the American Meteorological Society*, 84(7):921–925, 2003.

[48] J. Wouters and V. Lucarini. Multi-level dynamical systems: Connecting the Ruelle response theory and the Mori-Zwanzig approach. *Journal of Statistical Physics*, 151(5):850860, 2013.

[49] J. Rombouts, M. Ghil. Oscillations in a simple climate-vegetation model. *Nonlinear Process. Geophys.*, 22:275–288, 2015.

[50] D. Paillard. Quaternary glaciations: from observations to theories. *Quat. Sci. Rev.*, 107:11–24, 2015.

[51] R. Grimshaw. *Nonlinear Ordinary Differential Equations*. CRC Press, 1993.

[52] B. Saltzman. A survey of statistical-dynamical models of the terrestrial climate. *Adv. Geophys.*, 20:183–307, 1978.

[53] A. Evenson B. Saltzman, A. Sutera. Structural stochastic stability of a simple auto-oscillatory climatic feedback system. *J. Atm. Sci.*, 38:494–503, 1981.

[54] C. Nicolis. Self-oscillations and predictability in climate dynamics. *Tellus*, 36A:1–10, 1984.

[55] C. Nicolis. Long-term climatic variability and chaotic dynamics. *Tellus*, 39A:1–9, 1987.

[56] C. Nicolis. Long-term climatic transitions and stochastic resonance. *J. Stat. Phys.*, 70:3–14, 1993.

[57] D.V. Alexandrov, I.A. Bashkirtseva, L.B. Ryashko. Stochastically driven transitions between climate attractors. *Tellus*, 66:23454, 2014.

[58] `https://earthobservatory.nasa.gov/Features/SeaIce`.

[59] B. Bereiter, S. Shackleton, D. Baggenstos, K. Kawamura, J. Severinghaus. Mean global ocean temperatures during the last glacial transition. *Nature*, 553:39–44, 2018.

[60] P.E. Kloeden, E. Platen. *Numerical Solution of Stochastic Differential Equations*. Springer, 1992.

[61] G. Benettin, L. Galgani, A. Giorgilli, J.M. Strelcyn. Lyapunov characteristic exponents for smooth dynamical systems and for hamiltonian systems; a method for computing all of them. part 1: theory. *Meccanica*, 15:9–20, 2014.

[62] J. G. Charney. Dynamics of deserts and droughts in the sahel. *Q. J. R. Meteorol. Soc.*, 101:193–202, 1975.

[63] J. Otterman, M. D. Chou, and A. Arking. Effects of nontropical forest cover on climate. *Journal of Climate Appl. Meteorol.*, 23:762–767, 1984.

[64] W.D. Sellers. A global climatic model based on the energy balance of the earth-atmosphere system. *J. Appl. Meteorol.*, 8:392–400, 1969.

[65] M.I. Budyko. The effect of solar radiation variations on the climate of the earth. *Tellus*, 21:611–619, 1969.

[66] W.T. Hyde, T.J. Crowley, S.K. Baum, W.R. Peltier. Neoproterozoic 'snowball earth' simulations with a coupled climate/ice-sheet model. *Nature*, 405:425–429, 2000.

[67] D. Herwartz, A. Pack, D. Krylov, Y. Xiao, K. Muehlenbachs, S. Sengupta, T. Di Rocco. Revealing the climate of snowball earth from Δ^{17}o systematics of hydrothermal rocks. *Proc. Nat. Acad. Sci.*, 112:5337–5341, 2015.

[68] I. Banik. Snowball earth. *Astrobiol. Outreach*, 4:153, 2016.

[69] P.F. Hoffman, D.S. Abbot, Y. Ashkenazy et al. Snowball earth climate dynamics and cryogenian geology-geobiology. *Sci. Adv.*, 3:e1600983, 2017.

[70] P.F. Hoffman, A.J. Kaufman, G.P. Halverson, D.P. Schrag. A neoproterozoic snowball earth. *Science*, 281:1342–1346, 1998.

[71] B. Mills, A. J. Watson, C. Goldblatt, R. Boyle, and T. M. Lenton. Timing of neoproterozoic glaciations linked to transport-limited global weathering. *Nature Geoscience*, 4(12):861864, 2011.

[72] E. N. Lorenz. Deterministic non-periodic flow. *Journal of the Atmospheric Sciences*, 20:130–141, 1963.

[73] B. Saltzman. *Dynamical Paleoclimatology: Generalised Theory of Global Climate Change*. Academic Press, 2002.

[74] A.S. Pikovsky, J. Kurths. Coherence resonance in a noise-driven excitable system. *Phys. Rev. Lett.*, 78:775–778, 1997.

[75] B. Saltzman. Carbon dioxide and the δ^{18}o record of late-quaternary climatic change: a global model. *Clim. Dyn.*, 1:77–85, 1987.

[76] B. Saltzman and K. A. Maasch. Carbon cycle instability as a cause of the late pleistocene ice age oscillations: modeling the asymmetric response. *Global Biogeochem. Cycles*, 2(2):117–185, 1988.

[77] M. Y. Verbitsky, M. Crucifix, and D. M. Volobuev. A theory of pleistocene glacial rhythmicity. *Earth System Dynamics*, 9(3):10251043, 2018.

[78] E. Izhikevich. Neural excitability, spiking and bursting. *Int. J. Bifur. Chaos*, 10:1171–1266, 2000.

[79] D. Paillard, F. Parrenin. The antarctic ice sheet and the triggering of deglaciations. *Earth Planet. Sci. Lett.*, 227:263–271, 2004.

[80] J. F. W. Herschel. Xvii.–on the astronomical causes which may influence geological phaenomena. *Transactions of the Geological Society of London*, s2-3(2):293300, 1832.

[81] A. Berger. Histoire de paloclimats. Préface Duplessy / Ramstein, 2012.

[82] D. Paillard. Climate science: Predictable ice ages on a chaotic planet. *Nature*, 542:419420, 2017.

[83] P. Bretagnon. Termes longues priodes dans le systme solaire. *Astron. Astroph.*, 30:141–154, 1974.

[84] J. L. Lagrange. Thorie des variations sculaires des lments des plantes 1. In *Nouveaux mémoires de l'Académie Royale des Sciences et Belles-Lettres*, pages 199–276, 1781.

[85] A. L. Berger. Long-term variations of daily insolation and quaternary climatic changes. *Journal of the Atmospheric Sciences*, 35:2362–2367, 1978.

[86] J. Laskar, A. Fienga, M. Gastineau, and H. Manche. La2010: a new orbital solution for the long-term motion of the earth. *Astronomy and Astrophysics*, 532:A89, 2011.

[87] J. Oerlemans. On zonal asymmetry and climate sensitivity. *Tellus*, 32(6):489–499, 1980.

[88] D. Pollard. A simple ice sheet model yields realistic 100 kyr glacial cycles. *Nature*, 296(5855):334–338, 1982.

[89] J. Imbrie, E. A. Boyle, S. C. Clemens, A. Duffy, W. R. Howard, G. Kukla, J. E. Kutzbach, D. G. Martinson, A. McIntyre, A. C. Mix, B. Molfino, J. J. Morley, L. C. Peterson, N. G. Pisias, W. L. Prell, M. E. Raymo, N. J. Shackleton, and J. R. Toggweiler. On the structure and origin of major glaciation cycles 1. linear responses to milankovitch forcing. *Paleoceanography*, 7(6):701–738, 1992.

[90] H. Gallée, J. P. van Ypersele, T. Fichefet, I. Marsiat, C. Tricot, and A. Berger. Simulation of the last glacial cycle by a coupled, sectorially averaged climate-ice sheet model. part ii : Response to insolation and co_2 variation. *Journal of Geophysical Research*, 97:15713–15740, 1992.

[91] D. Paillard. The timing of pleistocene glaciations from a simple multiple-state climate model. *Nature*, 391:378–381, 1998.

[92] B. Saltzman and K. A. Maasch. A first-order global model of late cenozoic climate. *Transactions of the Royal Society of Edinburgh Earth Sciences*, 81:315–325, 1990.

[93] M. Milankovitch. *Kanon der Erdbestrahlung und Seine Anwendung auf das Eiszeitenproblem (Canon of insolation and the ice-age problem).* Könlishe Serbische Akademie, 1941.

[94] P. Huybers and E. Tziperman. Integrated summer insolation forcing and 40,000-year glacial cycles: The perspective from an ice-sheet/energy-balance model. *Paleoceanography*, 23:PA1208, 2008.

[95] J. Carson, M. Crucifix, S. P. Preston, and R. D. Wilkinson. Quantifying age and model uncertainties in palaeoclimate data and dynamical climate models with a joint inferential analysis. *Proceedings of the Royal Society A: Mathematical, Physical and Engineering Sciences*, 475(2224):20180854, 2019.

[96] A. Berger and M. F. Loutre. Insolation values for the climate of the last 10 million years. *Quaternary Science Reviews*, 10(4):297 – 317, 1991.

[97] A. Berger and M. F. Loutre. Origine des frquences des lments astronomiques intervenant dans l'insolation. *Bull. Classe des Sciences*, 1-3:45–106, 1990.

[98] D. J. Thompson. Spectrum estimation and harmonic analysis. *Proceedings of the IEEE*, 70:1055–1096, 1982.

[99] R. Vautard, P. Yiou, and M. Ghil. Singular-spectrum analysis: A toolkit for short, noisy chaotic signals. *Physica D: Nonlinear Phenomena*, 58(1–4):95–126, 1992.

[100] T. Mitsui and K. Aihara. Dynamics between order and chaos in conceptual models of glacial cycles. *Climate Dynamics*, 42(11-12):3087–3099, 2014.

[101] J. D. Hays, J. Imbrie, and N. J. Shackleton. Variations in the earth's orbit : Pacemaker of ice ages. *Science*, 194:1121–1132, 1976.

[102] K. Kawamura, F. Parrenin, L. Lisiecki, R. Uemura, F. Vimeux, J. P. Severinghaus, M. A. Hutterli, T. Nakazawa, S. Aoki, J. Jouzel, M. E. Raymo, K. Matsumoto, H. Nakata, H. Motoyama, S. Fujita, K. Goto-Azuma, Y. Fujii, and O. Watanabe. Northern hemisphere forcing of climatic cycles in antarctica over the past 360,000 years. *Nature*, 448:912–914, 2007.

[103] P. Huybers and C. H. Langmuir. Delayed co_2 emissions from mid-ocean ridge volcanism as a possible cause of late-pleistocene glacial cycles. *Earth and Planetary Science Letters*, 457:238249, 2017.

[104] D. MacAyeal. A catastrophe model of the paleoclimate. *Journal of Glaciology*, 24(90):245–257, 1979.

[105] P. D. Ditlevsen. Bifurcation structure and noise-assisted transitions in the pleistocene glacial cycles. *Paleoceanography*, 24:PA3204, 2009.

[106] I. Daruka and P. D. Ditlevsen. A conceptual model for glacial cycles and the middle pleistocene transition. *Climate Dynamics*, 46:2940, 2016.

[107] P. C. Tzedakis, M. Crucifix, T. Mitsui, and E. W. Wolff. A simple rule to determine which insolation cycles lead to interglacials. *Nature*, 542:427432, 2017.

[108] N. Gandy, L. J. Gregoire, J. C. Ely, C. D. Clark, D. M. Hodgson, V. Lee, T. Bradwell, and R. F. Ivanovic. Marine ice sheet instability and ice shelf buttressing of the minch ice stream, northwest scotland. *The Cryosphere*, 12(11):36353651, 2018.

[109] G. E. Birchfield, J. Weertman, and A. T. Lunde. A paleoclimate model of northern hemisphere ice sheets. *Quaternary Research*, 15(2):126–142, 1981.

[110] M. Y. Verbitsky and D. V. Chalikov. *Modelling of the GlaciersOceanAtmosphere System*. Leningrad, 1986.

[111] D. Pollard. A coupled climate-ice sheet model applied to the quaternary ice ages. *Journal of Geophysical Research*, 88(C12):7705–7718, 1983.

[112] R. Calov, A. Ganopolski, C. Kubatzki, and M. Claussen. Mechanisms and time scales of glacial inception simulated with an earth system model of intermediate complexityarth system model of intermediate complexity. *Climate of the Past*, 5(2):245–258, 2009.

[113] A. Ganopolski and V. Brovkin. Simulation of climate, ice sheets and co_2: evolution during the last four glacial cycles with an earth system model of intermediate complexity. *Climate of the Past*, 13(12):16951716, 2017.

[114] D. Archer, A. Winguth, D. Lea, and N. Mahowald. What caused the glacial/interglacial atmospheric pco_2 cycles? *Reviews of Geophysics*, 38(2):159–189, 2000.

[115] K. Kohfeld and A. Ridgwell. Glacial-interglacial variability in atmospheric co^2. In C. Le Qur and E. Saltzman, editors, *Surface Ocean—Lower Atmosphere Processes*, volume 187, pages 251–286, 2009.

[116] Past Interglacials Working Group of PAGES. "interglacials of the last 800,000 years". *Reviews of Geophysics*, 2015.

[117] A. Landais, G. Dreyfus, E. Capron, J. Jouzel, V. Masson-Delmotte, D. M. Roche, F. Prie, N. Caillon, J. Chappellaz, M. Leuenberger, A. Lourantou, F. Parrenin, D. Raynaud, and G. Teste. Two-phase change in co2, antarctic temperature and global climate during termination ii. *Nature Geosciences*, 6(12):1062–1065, 2013.

[118] A. W. Omta, B. W. Kooi, G. A. K. van Voorn, R. E. M. Rickaby, and M. J. Follows. Inherent characteristics of sawtooth cycles can explain different glacial periodicities. *Climate Dynamics*, 2015.

[119] A. Pikovski, M. Rosenblum, and J. Kurths. *Synchronization: a universal concept in nonlinear sciences*, volume 12. 2001.

[120] M. Crucifix. Why could ice ages be unpredictable? *Climate of the Past*, 9(5):2253–2267, 2013.

[121] A. B. Belogortsev. Analytical approach to the torus bifurcations in the quasiperiodically forced van der pol oscillator. *Physics Letters A*, 161(4):352–356, 1992.

[122] T. Kapitaniak and J. Wojewoda. Strange non-chaotic attractors of a quasi-periodically forced van der pol's oscillator. *Journal of Sound and Vibration*, 138(1):162–169, 1990.

[123] A. S. Pikovsky and U. Feudel. Characterizing strange nonchaotic attractors. *Chaos: An Interdisciplinary Journal of Nonlinear Science*, 5(1):253260, 1995.

[124] J. A. Langa, J. C. Robinson, and A. Suárez. Stability, instability, and bifurcation phenomena in non-autonomous differential equations. *Nonlinearity*, 15(3):887, 2002.

[125] J. C. Hargreaves and J. D. Annan. Assimilation of paleo-data in a simple earth system model. *Climate Dynamics*, 19:371–381, 2002.

[126] T. Mitsui and M. Crucifix. Effects of additive noise on the stability of glacial cycles. In F. Ancona, P. Cannarsa, C. Jones, and A. Portaluri, editors, *Mathematical Paradigms of Climate Science*, Spring INdAM Series, pages 93–113. Springer Verlag, 2016.

[127] T. Kapitaniak, E. Ponce, and J. Wojewoda. Route to chaos via strange non-chaotic attractors. *Journal of Physics A: Mathematical and General*, 23(8):L383, 1990.

[128] T. Kapitaniak. Strange non-chaotic transients. *Journal of Sound and Vibration*, 158(1):189–194, 1992.

[129] M. Rasmussen. *Attractivity and bifurcation for nonautonomous dynamical systems*. Lecture Notes in Mathematics. 2000.

[130] H. Risken. *The Fokker-Planck Equation. Methods of Solution and Applications*. Springer-Verlag, Berlin, 1984.

[131] C. Gardiner. *Stochastic Methods. A Handbook for the Natural and Social Sciences*. Springer, Berlin, 2009.

[132] M. I. Freidlin, A. D. Wentzell. *Random Perturbations of Dynamical Systems*. Springer, New York, 2012.

[133] G. N. Milshtein, L. B. Ryashko. A first approximation of the quasipotential in problems of the stability of systems with random non-degenerate perturbations. *Journal of Applied Mathematics and Mechanics*, 59:47–56, 1995.

[134] I. Bashkirtseva, L. Ryashko. Sensitivity analysis of stochastic attractors and noise-induced transitions for population model with Allee effect. *Chaos*, 21:047514, 2011.

[135] R. A. Horn, C. R. Johnson. *Matrix Analysis*. Cambridge University Press, Cambridge, 2012.

[136] I. Bashkirtseva, L. Ryashko. Stochastic sensitivity of 3D-cycles. *Mathematics and Computers in Simulation*, 66:55–67, 2004.

[137] P. C. Mahalanobis. On the generalized distance in statistics. *Proceedings of the National Institute of Science of India*, 2:49–55, 1936.

[138] L. B. Ryashko, E. S. Slepukhina. Noise-induced torus bursting in the stochastic Hindmarsh-Rose neuron model. *Physical Review E*, 96:032212, 2017.

[139] I. Bashkirtseva, L. Ryashko. Analysis of noise-induced chaos-order transitions in Rulkov model near crisis bifurcations. *International Journal of Bifurcation and Chaos*, 27:1730014, 2017.

[140] I. Bashkirtseva, L. Ryashko, T. Ryazanova. Method of confidence domains in the analysis of noise-induced extinction for tritrophic population system. *European Physical Journal B*, 90:161, 2017.

[141] I. Bashkirtseva, L. Ryashko. Generation of mixed-mode stochastic oscillations in a hair bundle model. *Physical Review E*, 98:042414, 2018.

[142] I. Bashkirtseva, L. Ryashko. Noise-induced shifts in the population model with a weak Allee effect. *Physica A*, 491:28–36, 2018.